REPORT DOCUMENTATION PAGE

Form Approved
OMB No. 0704-0188

1. AGENCY USE ONLY (Leave blank)	2. REPORT DATE	3. REPORT TYPE AND DATES COVERED
	15 November 1993	Interim

4. TITLE AND SUBTITLE
Investigation of a Cylindrical Nonacoustic-wavenumber Calibration Array

5. FUNDING NUMBERS
WU - DN220-161
PE - 61153N
TA - RR011

6. AUTHOR(S)
L. Dwight Luker

7. PERFORMING ORGANIZATION NAME(S) AND ADDRESS(ES)
NAVAL RESEARCH LABORATORY
UNDERWATER SOUND REFERENCE DETACHMENT
PO BOX 568337
ORLANDO, FL 32856-8337

8. PERFORMING ORGANIZATION REPORT NUMBER
NRL MEMORANDUM REPORT 7385

9. SPONSORING/MONITORING AGENCY NAME(S) AND ADDRESS(ES)
OFFICE OF NAVAL RESEARCH
800 N. QUINCY STREET
ARLINGTON, VA 22217-5000

10. SPONSORING/MONITORING AGENCY REPORT NUMBER

11. SUPPLEMENTARY NOTES
Report is based on author's doctoral thesis dissertation submitted to the Georgia Institute of Technology, Atlanta, GA

12a. DISTRIBUTION/AVAILABILITY STATEMENT
Approved for public release; distribution unlimited.

12b. DISTRIBUTION CODE

13. ABSTRACT *(Maximum 200 words)*

This thesis describes an investigation of a Cylindrical Wavenumber Calibrator (CWC). The CWC is a water-filled device designed to generate nonacoustic-wavenumber pressure fields propagating axially in the water within the calibrator. It can therefore be used to simulate the effects of flow noise on a device placed in the water. The investigation begins with the mathematical analysis of the pressure field inside an infinitely-long, liquid-filled, cylindrical chamber with an axially-symmetric, normal-velocity distribution on the wall of the chamber. The analysis then continues with the study of the propagation speed in the fluid inside an infinite-length elastic tube surrounded by another fluid. A finite-length CWC is then investigated with several computer models of the CWC using the CHIEF acoustic-radiation program and the ATILA finite element program. These models are integrated into a computer program that uses the electroacoustic transfer matrix for the system to compute electrical band drives designed to produce the desired nonacoustic-wavenumber fields within the CWC. A prototype CWC with 40 independently-driven bands was constructed from a piezoelectric-PVDF tube. Measured results show that relatively uniform nonacoustic-wavenumber pressure fields can be created with the CWC.

14. SUBJECT TERMS			15. NUMBER OF PAGES
Acoustic	Nonacoustic	Sonar	127
Wavenumber	Calibrator		16. PRICE CODE
Evanescant	Flow noise		

17. SECURITY CLASSIFICATION OF REPORT	18. SECURITY CLASSIFICATION OF THIS PAGE	19. SECURITY CLASSIFICATION OF ABSTRACT	20. LIMITATION OF ABSTRACT
UNCALSSIFIED	UNCLASSIFIED	UNCLASSIFIED	UL

Naval Research Laboratory

Washington, DC 20375-5320

NRL/MR/5983/93-7385

INVESTIGATION OF A CYLINDRICAL NONACOUSTIC-WAVENUMBER CALIBRATION ARRAY

by

L. Dwight Luker

Naval Research Laboratory
Underwater Sound Reference Detachment
Orlando, FL 32856-8337

15 November 1993

CONTENTS

FIGURES

TABLES

SYMBOLS

Roman Letters

a	inner radius
A	arbitrary constant
A_i	area of surface i
A^{i}_{inner}	area of the inner surface of the ith band
A^{i}_{outer}	area of the outer surface of the ith band
b	outer radius
B	arbitrary constant
c	speed of sound
c_d	dilatational wave speed in region II
c_e	phase speed of evanescent wave
c_i	speed of sound in region I
c_s	speed of sound in region III
c_t	shear wave speed in region II
C	arbitrary constant
C_m	mechanical compliance of ring
$\boldsymbol{d}$	vector of applied drives
d_{31}	piezoelectric strain coefficient
D	arbitrary constant
$\boldsymbol{D}$	vector of computed drives
e	strain
ε_3	radial electric field
E_i	voltage applied across electrodes
f	frequency
F	arbitrary constant
F_i	total normal force exerted on surface i
$\boldsymbol{F}$	vector of the nodal values of forces
$\boldsymbol{F}^D$	vector of the nodal values of external forces that drive the structure
$\boldsymbol{F}^R$	vector of the nodal values of forces associated with fluid loading
$\bar{\boldsymbol{F}}$	vector of normal surface forces
G	arbitrary constant
G^{ij}	a Green's function
i	$\sqrt{-1}$
h	height of piezoelectric ring
$H_n^{(2)}$	Hankel function of the second kind of order n
I	region inside infinite-length elastic tube
II	infinite-length elastic-tube region
III	region outside infinite-length elastic tube
$\boldsymbol{I}$	unit matrix
I_n	modified Bessel function of order n
J_n	Bessel function of order n

J_n'	derivative of Bessel function of order n
$\boldsymbol{k}$	wavevector
k	magnitude of wavevector
k_1	wavevector component in flow direction
k_2	wavevector component normal to wall
k_3	wavevector component in plane of wall perpendicular to flow direction
k_a	acoustic wavenumber = ω/c
k_d	dilatational wavenumber in region II = ω/c_d
k_{dr}	r component of k_d
k_e	evanescent wavenumber = ω/c_e
k_h	hydrodynamic wavenumber = ω/u
k_i	wavenumber in region I = ω/c_i
k_{ir}	r component of k_i
k_r	wavevector component in r direction
k_s	wavenumber in region III = ω/c_s
k_{sr}	r component of k_s
k_t	shear wavenumber in region II = ω/c_t
k_{tr}	r component of k_t
k_z	wavevector component in z direction
$[K_{uu}]$	stiffness matrix
$[K_{u\phi}]$	piezoelectric matrix
$[K_{\phi\phi}]$	dielectric matrix
m	number of field points
M	mass of ring
$\boldsymbol{M}$	transfer matrix
$\boldsymbol{M}'$	reduced transfer matrix
$[M]$	mass matrix
n	number of driven bands
$\boldsymbol{n}_i$	normal unit vector for surface S_i
p	acoustic pressure
p_i	acoustic pressure in region I
p_{inner}^{i}	pressure on the inner surface of the ith band
p_{outer}^{i}	pressure on the outer surface of the ith band
$\boldsymbol{p}$	vector of measured (or modeled) pressures at field points
$\boldsymbol{P}$	vector of desired pressures
$\boldsymbol{q}$	vector of the nodal values of the electrical charges
r	radial coordinate in cylindrical coordinate system
$r(x,\sigma)$	distance between surface point σ and field point x
s_{11}^{E}	elastic compliance coefficient with constant electric field
S	radiating surface
S_1	circumferential strain
t	time
t_w	wall thickness
T_1	circumferential stress
u	convection velocity
u_{ir}	radial component of displacement in region I
u_{iz}	axial component of displacement in region I
u_r	radial component of displacement in region II
u_z	axial component of displacement in region II

$\underline{U}$ vector of the nodal values of the displacement field
v normal surface velocity
v_0 amplitude of radial surface velocity
v_i normal surface velocity of the ith surface
v_r radial velocity
$v(\sigma)$ normal velocity on surface S
$\underline{V}$ vector of surface velocities
w half of the width of the window
W azimuthal component of vector potential Ψ
x coordinates of field point
Y Young's modulus
z axial coordinate in cylindrical coordinate system
z_i interior-wall impedance
$Z_{m_i}^{i}$ mechanical impedance for ith band
Z^{ij} radiation impedance
$[Z]$ radiation-impedance matrix
$[Z_{tot}]$ total impedance matrix

Greek Letters
α real quantity added to the diagonals of a matrix
$\delta(x)$ Dirac delta function
Δ dilatation
∇^2 Laplacian
Φ scalar potential function
$\underline{\Phi}$ vector of the nodal values of the electric potential
Ψ vector potential function
θ angular coordinate in cylindrical coordinate system
μ wavenumber multiplier, Lamé's constant
λ wavelength, Lamé's constant
ρ density
ρ_i density of fluid in region I
ρ_s density of fluid in region III
ρ_t density of infinite-length elastic tube in region II
σ coordinates of surface point
τ stress
ω angular frequency ($2\pi f$)
ξ integration variable

INVESTIGATION OF A CYLINDRICAL NONACOUSTIC-WAVENUMBER CALIBRATION ARRAY

INTRODUCTION

This thesis describes an investigation of a prototype Cylindrical Wavenumber Calibrator (CWC). The CWC is a cylindrical, tubular device designed to generate nonacoustic-wavenumber pressure fields in water within the CWC. It can therefore be used to simulate the effects of flow noise on a device placed in the water. The research consists of both theoretical and experimental investigations of the CWC.

Wavenumber Calibration

There has been considerable interest in recent years in the acoustic effects of the turbulent boundary layer (TBL) produced by the motion of a vehicle in water. There is concern about interference by the pressure field in the TBL with the proper operation of transducers used in sonar arrays. Sonar arrays are systems of transducers, often distributed over areas of a vessel or in lines towed behind a vessel, designed to detect acoustic-pressure fluctuations in the water. There is also concern about the excitation of structures of the vehicle, which results in undesirable acoustic fields both internally and externally.

The "flow noise" produced by the TBL is generally characterized by pressure fluctuations that are transported in the flow direction at a speed somewhat less than the free-stream velocity. Since these fluctuations are transported at speeds less than the sound speed in water, they have nonacoustic wavenumbers (i.e., wavenumbers higher than acoustic wavenumbers at the same frequency in water) and are, therefore, evanescent.

Several methods have been employed to reduce the undesirable effects of the flow noise. One method used is to slow the motion of the vehicle through the water, thereby reducing the amplitude of the flow noise. This method is effective but can cause serious tactical problems.

Another technique for reducing the undesirable effects of the flow noise is to spatially separate the acoustic sensors from the TBL. This is sometimes accomplished by using a sonar dome or a layer of acoustically transparent material. Since the convective field is evanescent, a relatively small separation distance can have a significant effect. This technique has limitations at low frequencies, however, where the beneficial effect is reduced.

A third technique for reducing the flow noise problem is spatial averaging. This is accomplished by using sonar sensors that are longer than the flow-noise wavelength.

A major problem encountered in studying the effects of flow noise on acoustic arrays and underwater structures is the fact that the structure of the TBL tends to be poorly defined and somewhat random in nature. Because of this, it is difficult to reproduce the same flow noise from one

measurement to the next. To gain better understanding of the effects of flow noise, it would be useful to be able to plot or calibrate the response of an array or structure as a function of the wavenumber of the excitation for frequencies of interest [1]. This could be achieved if a device existed that could generate a pressure field consisting of essentially a single nonacoustic-wavenumber component. The structure being analyzed could then be placed in the pressure field and its behavior monitored for different wavenumbers.

This thesis concerns an investigation of a cylindrical fluid-filled array designed to generate the desired nonacoustic-wavenumber pressure fields within the array. The work consisted of both theoretical and experimental investigations of the array.

Literature Review

Effects of Flow Noise

Over the years numerous attempts have been made to better understand flow noise and its effects on acoustic measurements in general [2,3]. There has been specific interest in the effects of flow noise on sonar sensors and underwater structures.

A characteristic wavevector-frequency spectrum of TBL wall pressure [4] is shown in Fig. 1. In this figure, k_1 is the wavenumber in the flow direction with k_1 and k_3 lying in the plane of the wall. In general, a qualitative description of the spectral density of the flow noise versus the streamwise wavenumber at a single frequency shows a convective domain or "convective ridge" located at the hydrodynamic wavenumber $k_h = \omega/u$, where ω is the radian frequency, and u is the convection velocity, which is a large fraction of the free-stream velocity. The spectral density decreases with decreasing wavenumber below the convective ridge. The region below the convective ridge and above the acoustic wavenumber $k_a = \omega/c$, where c is the sound speed in the fluid, is sometimes called the low-wavenumber region of the flow noise.

Corcos [5] discussed the ability of a transducer to resolve the spatial details of a turbulent pressure field with two opposite applications in mind. One involved the use of a transducer with a sensing area small enough to give a good account of the fine spatial structure of the turbulent field for studying the field. The other involved the use of transducers with sensing areas large enough to be insensitive to the flow noise within a given frequency band (i.e., larger than the flow-noise wavelength) and yet remain sensitive to incoming sound waves at the same frequency. The latter case is the one generally desired for sonar sensors. Corcos proposed a theoretical model that could be used to determine the response of a transducer to a turbulent pressure field using a size-correction factor and gave asymptotic formulas for large transducers that yield estimates of the degree to which a flush-mounted sonar receiver is able to discriminate against flow noise. Gilchrist and Strawderman [6] presented experimental results that showed good agreement with Corcos' predictions for the size correction value.

Heaps [7] extended Corcos' analysis to treat the case where the transducer is separated from the turbulent layer by a medium free of turbulent sources and through which pressure fluctuations are transmitted acoustically. A theory was developed to compute the attenuation of spectral density as a function of transducer size and distance from the turbulent flow. The theory predicts that (for small Mach numbers) the attenuation is effected more by a change in the separation distance than by a similar change in the radius of a circular transducer.

There has also been considerable interest in recent years in the effects of flow noise on

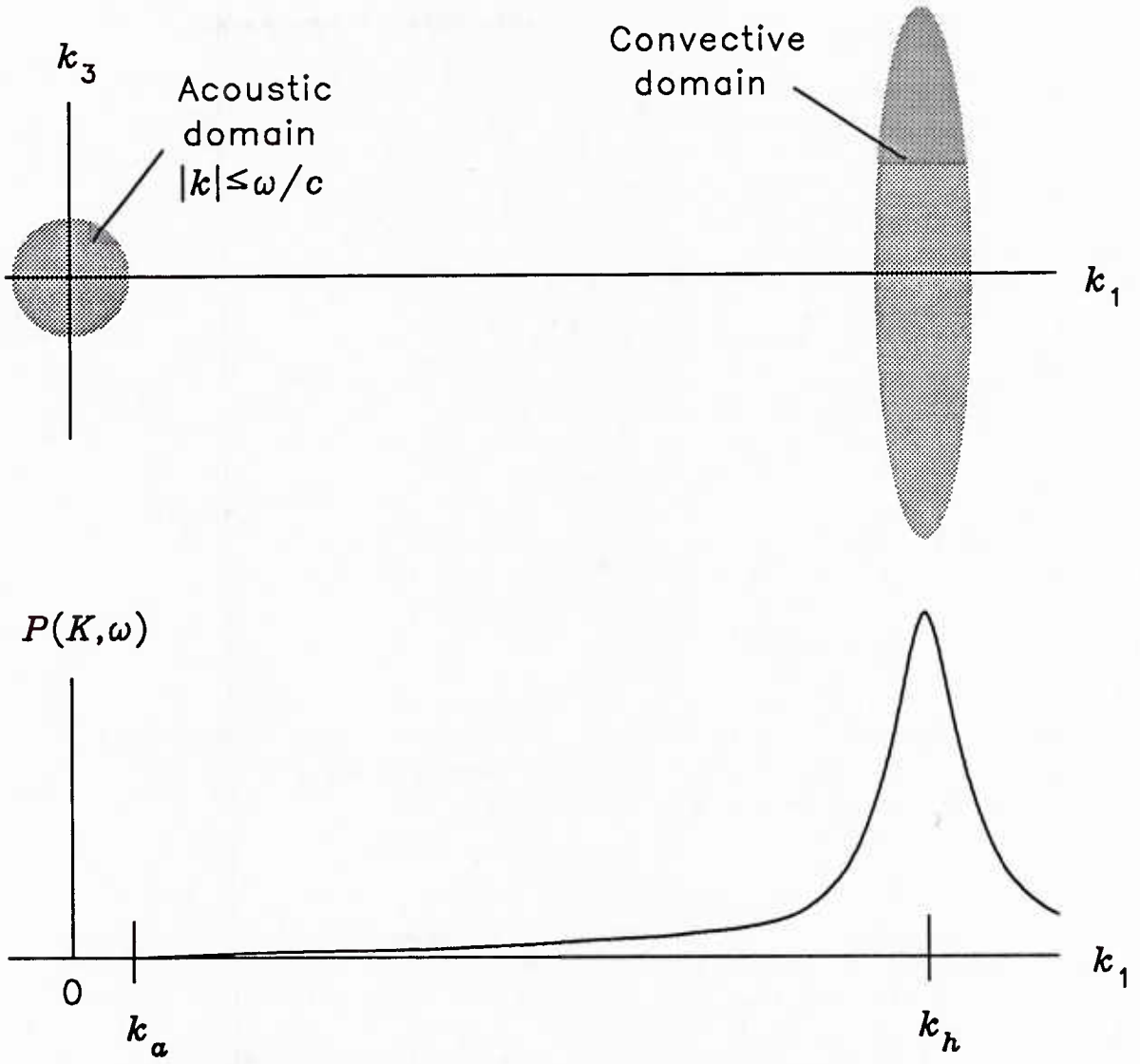

Fig. 1 — Characteristic wavevector-frequency spectrum of TBL wall pressure.

structures. If structures on a vehicle moving through the water are excited by the flow noise, they can then radiate into the vehicle as well as into the surrounding medium. The evanescent energy in the flow noise can, therefore, be converted into acoustic energy that can propagate over large distances. Chandiramani [8] presented a method for estimating the vibrational response of fluid-loaded structures when excited by low-speed TBL flow. An approximate method was also suggested for estimating vibrational characteristics of spatially nonhomogeneous structures excited by surface interactions.

Chandiramani [9] later modified an exact theory [10] of transmission of sound across an isotropic flat plate, involving longitudinal and shear waves, to be applicable to convective wavenumbers and presented closed-form results.

Wavenumber Filters

One problem encountered in measuring the wavenumber content of the low-wavenumber region of the flow noise is the fact that the typically low levels of the wavenumber-frequency spectral density are easily contaminated by the background acoustic noise. Maidanik and Jorgensen [11] proposed a solution to this problem in the form of a wave-vector filter. The filter would consist of an array of equally-spaced transducers aligned parallel to the flow direction. It was shown that with proper choices of sensor size, spacing, and polarity, a filter could be constructed to pass a single narrow band of wavenumbers. A particular example given shows 14 dB of attenuation outside the passband.

Blake and Chase [12,13] constructed a four-element microphone array and tested it as a wave-vector filter in a wind tunnel. Unfortunately, they were unable to conclusively establish whether the dominant array noise in the passband was spurious acoustic noise or flow noise. Therefore, the measurements placed only an upper limit on the flow-noise contribution.

It should be noted that, although reference is made in this thesis to both wavenumber filters (designed primarily as receiving devices) and wavenumber calibrators (designed primarily as transmitting devices), if a device is reciprocal, it can be used for either purpose.

Previous Wavenumber-Calibration Devices

Several techniques have been considered previously for wavenumber calibration with planar geometries. Powers and Sherman [14] examined three techniques for hydrophones; beam patterns taken in air (rather than water), the use of an evanescent-wave generator, and measurement of the spatial impulse response. Devices were constructed and measurements made to investigate the first two techniques.

Since the sound speed is approximately 4.4 times slower in air than in water, measuring the beam pattern of a hydrophone in air instead of in water simulates wavenumbers that are approximately 4.4 times higher than in water. Powers and Sherman constructed a 12.7×12.7-cm hydrophone consisting of 15 piezoelectric ceramic cylinders potted in urethane. Beam patterns taken at 20 kHz in water and 5 kHz in air were compared. The beam patterns were found to be significantly different even though these two cases had similar wavenumbers. A probable reason given for the differences is the different scattering from the hydrophone in the two cases. The acoustic impedance of the urethane potting material is a good match to water but a poor match to air. This would cause much more scattering from the potting in the air case than in the water case. This difference in scattering is a significant problem when trying to simulate water measurements in air.

Powers and Sherman also constructed and tested an evanescent-wave generator in air. The planar array was 10-cm long and 7-cm wide and contained 22 strip elements. Each element consisted of an air backed hemi-cylindrical membrane of piezoelectric polymer. The elements were wired so that the drive at each element could be inverted (i.e., shifted by 180°). The array was driven in air at 3 and 6 kHz. By changing the frequency and phasing of the elements, wavenumbers that were 7.9, 8.8, and 16.4 times the acoustic wavenumber in air were generated. Plots of the pressure in front of the array were obtained using a small probe microphone. A spatial Fourier transform was then performed on the pressure data to determine the wavenumber content. The results showed that high wavenumbers could be generated independent of the drive frequency using a phased transducer array. It was also demonstrated that the amplitude of these waves decreased exponentially with increasing normal distance from the array as would be expected for evanescent waves. It was further shown that undesired acoustic wavenumbers were also generated that contaminated the measured field to a level

that would make the array unusable for wavenumber calibration. It is concluded that a usable calibration array must be large, include many elements, and must work underwater for the calibration to be meaningful for hydrophones.

Schau *et al.* [15,16] constructed and tested a planar array using a piezoelectric composite material (Piezo Rubber) [17] for the active material. The array measured approximately 12.7×12.7 cm and was mounted on a 0.635-cm thick LEXAN backing plate to keep it planar. The array was electroded to provide 20 independently driven active strips. This array was operated in a water tank at 1 kHz and the pressure in front of the array was measured with a small (0.7 cm) hydrophone. Evanescent fields were generated in front of the array but these fields were heavily contaminated with the acoustic wavenumber. The pressure field was also apparently contaminated by the excitation of an antisymmetric Lamb wave [18] in the array and backing plate structure with a phase velocity close to that of the desired evanescent wave.

A planar array was constructed and tested by Trivett *et al.* [19] using piezoelectric polyvinylidene fluoride (PVDF) [20,21] for the active material. The PVDF was bonded to a 2.54-cm-thick LEXAN backing plate. This thick LEXAN backing plate was used to shift the phase speed of the antisymmetric Lamb wave above the region of the evanescent waves while keeping the array essentially acoustically transparent at the frequencies of intended operation. Utilizing the acoustic transparency of the array, drives were calculated using a model of the array consisting of a simple point-source integrated over a driven band. It was also noted that the window width (the length in the simulated flow direction of the region in which the evanescent waves are to be created) must satisfy certain criteria or the algorithm used to calculate the drives would produce drives that had a significant dipole outside of the window. This dipole drive would produce acoustic radiation that would contaminate the desired evanescent field. Since the wavenumber spectrum of the pressure field being generated is a convolution of the evanescent wavenumber k_e with the wavenumber spectrum of the window (i.e., a rectangular aperture), the wavenumber spectrum being generated is proportional to

$$\frac{\sin[(k-k_e)w]}{(k-k_e)w}, \tag{1}$$

where w is half of the width of the window. If the evanescent wavenumber and the window width are not chosen such that Eq. (1) equals zero for the acoustic wavenumber k_a then drives are generated that produce a dipole outside the window region.

This planar array was operated at frequencies between 500 and 2000 Hz and evanescent phase speeds between 30 and 150 m/s. The results showed good agreement with predicted pressure fields as long as the criteria that there be at least ten driven stripes per evanescent wavelength was satisfied.

Outline of the Thesis

This thesis reports on an investigation of a cylindrical wavenumber calibration array (CWC) designed to produce evanescent pressure fields within the array. The research consists of both theoretical and experimental investigations of the array.

The theoretical investigation of various aspects of the CWC is described. First the pressure field in an infinite-length region surrounded by a cylindrical surface with a specified axially-symmetric normal velocity is investigated. The predicted radial dependence of the pressure is plotted for several evanescent wavenumbers. The results indicate the need for a CWC with a low phase speed within the calibrator. The investigation of infinite-length arrays continues with the calculation of the phase

speeds for propagation inside an idealized array consisting of an interior fluid region surrounded by a cylindrical elastic tube and an outer fluid region. A PVDF CWC is investigated and found to have predicted phase speeds less than one-fifth the speed of sound of water. A finite-length CWC with discrete band drives is then investigated. A method is described for using the electroacoustic transfer matrix of the system to compute electrical drives that will produce the desired nonacoustic-wavenumber pressure fields within the CWC. The transfer matrix at the desired frequency can be determined by measurement or by using a computer model of the CWC. Three computer models of the CWC are presented that can be used to determine the transfer matrix. The acoustic-radiation program Combined Helmholtz Integral Equation Formulation (CHIEF) [22] and the finite-element program ATILA [23] are used for this investigation. These models are combined in a computer program that determines the CWC's electrical drives and can also be used to map the predicted pressure fields within the array. These predictions show a good evanescent pressure field throughout most of the interior of the CWC.

I will also explain the experimental setup used for the investigation of the CWC. First a prototype array consisting of a PVDF tube with 40 independently driven bands is described. Then an electronic drive system is described that allows the 40 bands to be driven with independently controlled amplitudes and phases. A measurement setup is then presented that allows precise positioning of a hydrophone within the water-filled CWC with either air or castor oil on the outside of the array. An electronic measurement system is then described that automatically maps the amplitude and phase of the acoustic pressure within the CWC at specified locations.

The results of the experimental investigation are reported and measured results are compared with the theoretical predictions. Conclusions and recommendations for future work are then presented.

THEORETICAL INVESTIGATION

The theoretical investigation of the CWC includes analytical studies of infinite-length cylindrical geometries and numerical analysis of a finite length CWC. The analysis begins by studying a nonacoustic or evanescent wave inside an infinite-length cylindrical region bounded by a surface with a specified normal velocity having only a z dependence. The analysis continues with the study of the propagation speed in the fluid within an infinite-length elastic tube surrounded by another fluid. A finite-length CWC is then investigated using the CHIEF acoustic-radiation program and the ATILA finite element program. These models of a finite-length CWC are integrated into a computer program that determines the electrical band drives for the CWC and predicted pressures within the CWC.

Analysis of Infinite-Length Geometries

Cylindrical Region with a Specified Normal Wall Velocity

One area of concern regarding a CWC is the radial uniformity of the evanescent pressure field within the calibrator. To estimate the field uniformity within an actual calibrator a mathematical analysis was performed on an idealized device consisting of an infinitely long, fluid-filled, cylindrical region bounded by a surface at $r = a$. Considering the harmonic, steady-state situation [i.e., $\exp(-i\omega t)$ time dependence], the pressure p is a solution to the Helmholtz equation [24]

$$\nabla^2 p + k^2 p = 0 , \tag{2}$$

where k is the magnitude of the wavevector $\boldsymbol{k}$ and is equal to ω/c, ω is the angular frequency equal to $2\pi f$, f is the frequency, and c is the sound speed in the fluid. In cylindrical coordinates (r,θ,z), the

Laplacian ∇^2 is given by [25]

$$\nabla^2 = \frac{1}{r}\frac{\partial}{\partial r}\left(r\frac{\partial}{\partial r}\right) + \frac{1}{r^2}\frac{\partial^2}{\partial \theta^2} + \frac{\partial^2}{\partial z^2} . \tag{3}$$

For axially symmetric fields, the cylindrical Helmholtz equation then becomes

$$\frac{1}{r}\frac{\partial}{\partial r}\left(r\frac{\partial p}{\partial r}\right) + \frac{\partial^2 p}{\partial z^2} + k^2 p = 0 . \tag{4}$$

Imposing the condition that the pressure be finite at $r = 0$, the solution to Eq. (4) can be written as

$$p(r,z) = A J_0(k_r r)\, \exp(ik_z z) , \tag{5}$$

where A is a constant to be determined by the boundary condition at $r = a$, J_0 is a Bessel function, and k_r and k_z are the wavevector components in the r and z directions with

$$k_r^2 + k_z^2 = k^2 . \tag{6}$$

In order to conveniently incorporate a specified-velocity boundary condition at $r = a$, the pressure can be written in the form of a Fourier integral as [26]

$$p(r,z) = \int_{-\infty}^{\infty} A(k_z)\, J_0\left(\sqrt{k^2 - k_z^2}\, r\right) \exp(ik_z z)\, dk_z . \tag{7}$$

Defining the radial velocity as $v_r(r,z)$ and utilizing the linear approximation of Euler's equation [27]

$$\rho \frac{\partial v}{\partial t} = -\frac{\partial p}{\partial r} , \tag{8}$$

where ρ is the density of the fluid, the boundary condition at $r = a$ becomes

$$i\omega\rho v_r(a,z) = \frac{\partial}{\partial r} p(r,z)\Big|_{r=a} . \tag{9}$$

Letting ξ replace the integration variable k_z, one has

$$\frac{\partial}{\partial r} p(r,z) = \int_{-\infty}^{\infty} A(\xi)\, \sqrt{k^2 - \xi^2}\; J_0'\left(\sqrt{k^2 - \xi^2}\, r\right) \exp(i\xi z)\, d\xi \tag{10}$$

or

$$\frac{\partial}{\partial r}\, p(r,z) = \int_{-\infty}^{\infty} -A(\xi)\, \sqrt{k^2 - \xi^2}\; J_1\left(\sqrt{k^2 - \xi^2}\; r\right) \exp(i\xi z)\; d\xi \ . \tag{11}$$

The boundary condition then becomes

$$i\omega\rho v_r(a,z) = \int_{-\infty}^{\infty} -A(\xi)\, \sqrt{k^2 - \xi^2}\; J_1\left(\sqrt{k^2 - \xi^2}\; a\right) \exp(i\xi z)\; d\xi \ . \tag{12}$$

Multiplying both sides by $\exp(-i\eta z)$ and integrating over z from $-\infty$ to ∞, gives

$$\begin{aligned} i\omega\rho \int_{-\infty}^{\infty} v_r(a,z)\, \exp(-i\eta z)\; dz \\ = \int_{-\infty}^{\infty} \int_{-\infty}^{\infty} -A(\xi)\, \sqrt{k^2 - \xi^2}\; J_1\left(\sqrt{k^2 - \xi^2}\; a\right) \exp[i(\xi - \eta)z]\; d\xi dz \ . \end{aligned} \tag{13}$$

Utilizing the identity [28]

$$\int_{-\infty}^{\infty} \exp(i\alpha z)\; dz = 2\pi\delta(\alpha) \ , \tag{14}$$

where $\delta(\alpha)$ is the Dirac delta function [29], and the fact that

$$\int_{-\infty}^{\infty} f(\xi)\; \delta(\xi - \eta)\; d\xi = f(\eta) \ , \tag{15}$$

Eq. (13) becomes

$$i\omega\rho \int_{-\infty}^{\infty} v_r(a,z)\, \exp(-i\eta z)\; dz = -2\pi\; A(\eta)\, \sqrt{k^2 - \eta^2}\; J_1\left(\sqrt{k^2 - \eta^2}\; a\right) . \tag{16}$$

Solving for $A(\eta)$ gives

$$A(\eta) = \frac{-i\omega\rho \int_{-\infty}^{\infty} v_r(a,z)\, \exp(-i\eta z)\; dz}{2\pi\, \sqrt{k^2 - \eta^2}\; J_1\left(\sqrt{k^2 - \eta^2}\; a\right)} \ . \tag{17}$$

The normal velocity on the surface is specified as

$$v_r(a,z) = v_0 \exp(ik_e z) \ , \tag{18}$$

where k_e is the desired evanescent wavenumber. The evanescent wavenumber is related to the acoustic wavenumber k by

$$k_e = \mu k \qquad (\mu > 1) \ , \tag{19}$$

where μ is the wavenumber multiplier. With this velocity, one has

$$\int_{-\infty}^{\infty} v_r(a,z) \exp(-ik_z z)\, dz = v_0 \int_{-\infty}^{\infty} \exp\left[i(k_e - k_z)z\right] dz \ . \tag{20}$$

Again utilizing the identity given in Eq. (14), this becomes

$$\int_{-\infty}^{\infty} v_r(a,z) \exp(-ik_z z)\, dz = 2\pi v_0\, \delta(k_e - k_z) \ . \tag{21}$$

Inserting this result into Eq. (17) yields

$$A(k_z) = \frac{-i\omega\rho v_o\, \delta(k_e - k_z)}{\sqrt{k^2 - k_z^2}\ J_1\left(\sqrt{k^2 - k_z^2}\ a\right)} \ . \tag{22}$$

The pressure is then, from Eqs. (7) and (22),

$$p(r,z) = \int_{-\infty}^{\infty} \frac{-i\omega\rho v_o\, J_0\left(\sqrt{k^2 - k_z^2}\ r\right)}{\sqrt{k^2 - k_z^2}\ J_1\left(\sqrt{k^2 - k_z^2}\ a\right)} \exp(ik_z z)\, \delta(k_e - k_z)\, dk_z \ . \tag{23}$$

Once again utilizing the characteristic of the Dirac delta function given in Eq. (15), and Eq. (19) one obtains

$$p(r,z) = \frac{-i\rho c v_o\, J_0\left(k\sqrt{1-\mu^2}\ r\right)}{\sqrt{1-\mu^2}\ J_1\left(k\sqrt{1-\mu^2}\ a\right)} \exp(ik_e z) \ . \tag{24}$$

For evanescent waves μ is greater than one making the arguments of the Bessel functions imaginary. This necessitates the use of the modified Bessel functions I_0 and I_1 [30]. The pressure inside the cylindrical region is then

$$p(r,z) = \frac{-\rho c v_o \, I_0\left(k\sqrt{\mu^2-1}\, r\right)}{\sqrt{\mu^2-1}\; I_1\left(k\sqrt{\mu^2-1}\, a\right)} \exp(ik_e z) \; . \tag{25}$$

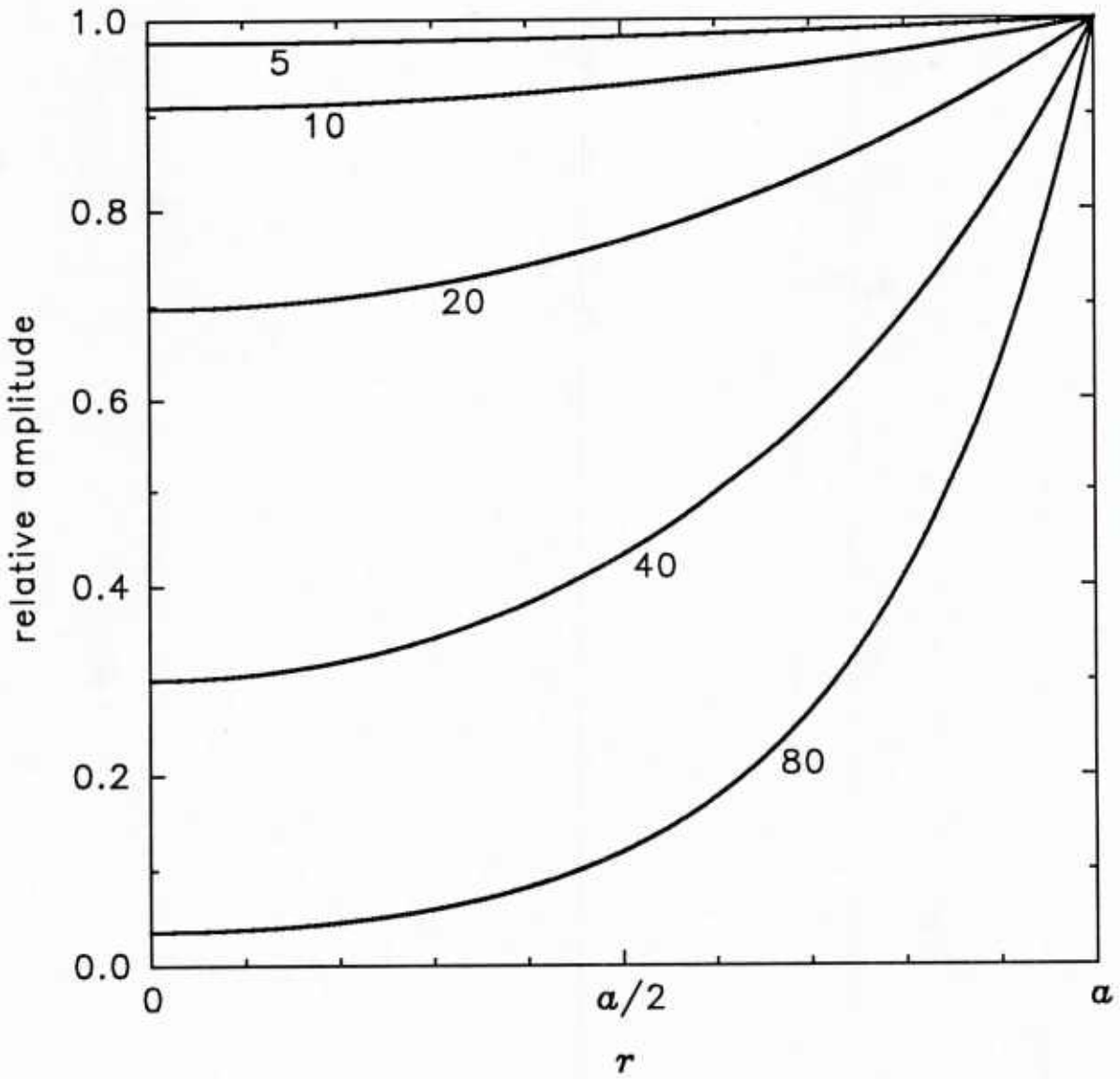

Fig. 2 — Radial pressure dependence for various wavenumber multipliers.

The pressure shows the desired z dependence and a radial dependence that has a maximum at $r = a$ decaying to a minimum at $r = 0$. The results of this analysis are shown in Fig. 2. The plot shows the radial pressure dependence for various wavenumber multipliers for a water-filled region at a frequency of 1 kHz with a wall radius a of 1.5 cm. The results show that the pressure drops only slightly for small wavenumber multipliers but decays rapidly for large multipliers.

For a calibration device, it is desirable for the pressure field to be as uniform as possible. One reason for this is the desire to have the highest pressure possible in the central portion of the calibrator, where the device being calibrated is placed, relative to the inner surface of the calibrator. A rapidly decaying field also restricts the size of the device being calibrated and makes the positioning of the device very critical.

One way to improve the uniformity of the pressure field is to reduce the natural propagation speed within the calibrator. This allows the creation of pressure fields with specified evanescent wavenumbers using smaller wavenumber multipliers. The smaller multipliers then result in more uniform pressure fields.

At a specified frequency the propagation speed within the calibrator depends on two things: (1) the fluid within the calibrator and (2) the compliance of the calibrator wall. Because the devices that will be calibrated are normally operated in water, the calibrator will be filled with water when in use. Even if another fluid was used, most convenient fluids have sound speeds that do not vary greatly from that of water. The only other way to significantly lower the propagation speed is to design a calibrator with a fairly flexible wall.

Propagation Speed

To determine the predicted propagation speed within the PVDF CWC prototype, the propagation speed in the fluid within an infinite-length elastic tube surrounded by another fluid was studied. The details of this analysis are given in Appendix A. To verify the predicted propagation speeds experimentally, an effort was undertaken to measure the propagation speeds within the CWC. The relatively short length of the CWC and low frequencies involved meant that it was not feasible to determine the propagation speeds with time-of-flight measurements. The first four resonant frequencies for the water column within the CWC were measured with the CWC air backed and castor-oil backed. Using these frequencies and the effective length [31] of the CWC the propagation speed within the CWC could then be calculated for each case.

The results of this analysis for the PVDF CWC prototype with either air or castor oil for the outer fluid are shown in Fig. 3. The figure shows the propagation speed in the water within the CWC as a function of frequency throughout the operational frequency range of the drive electronics. This frequency range is below the cutoff frequency for all modes in the water except the zeroeth mode. The cutoff frequency for the next mode was calculated [32] to be approximately 35 kHz. The measured propagation speeds at the first four resonances show good agreement with the theoretical speeds. The reduction in the propagation speed with the oil on the outside of the CWC is caused by the mass loading of the oil. At very low frequencies this effect is of little importance because inertial forces are small compared to elastic forces [33].

It can be seen that the propagation speed within the PVDF CWC prototype is about one-fifth the sound speed in open water (1485 m/s). This would indicate that pressure fields for a given evanescent wavenumber could be created within the PVDF CWC with much less radial pressure dependance than within a more rigid calibrator where the propagation speed would be closer to the speed of sound in water.

Determination of Band Drives

Operation of the CWC requires the determination of appropriate sets of band drives that will produce acceptable high-wavenumber fields within the CWC. The technique that was used was to first determine the electroacoustic transfer matrix for the system and then use the inverse transfer matrix to

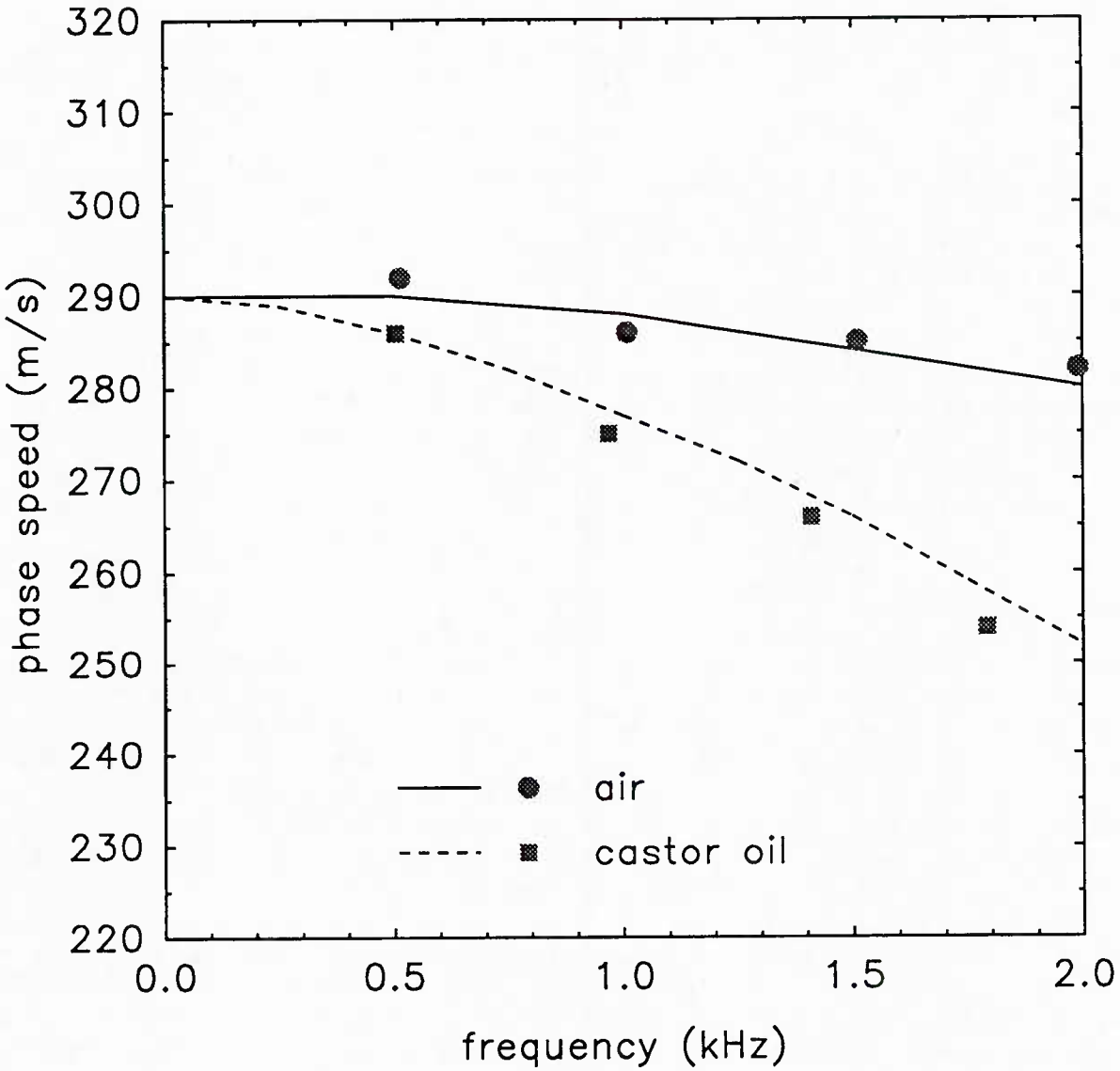

Fig. 3 — Theoretical and measured propagation speeds in the water column within the PVDF CWC with air or castor oil outside the CWC.

calculate a set of drives that will produce a desired field [34].

Assume that there are n driven bands each being driven by a sinusoidal signal d_i, $i = 1, 2, \ldots, n$. Also assume that the pressure can be determined at m field points within the CWC where $m \geq n$. The pressure at the field point may be determined by actual measurement or it may be determined using a computer model of the device. The pressure at the jth field point (where $j = 1, 2, \ldots, m$) has a complex value p_j. If the system is linear and superposition holds, one can define the electroacoustic transfer matrix by

$$p = Md \ , \tag{26}$$

where the transfer matrix M is an $m \times n$ complex matrix. The first task is to determine the elements of M. This can be accomplished by driving each band alone and measuring the resultant pressures at each field point. First one applies drive d_1 to the first band, while setting all the other band drives to zero, and determine the resulting pressure at each of the field points. One can then obtain the first column of M from

$$\left.\begin{aligned} M_{11} &= p_1/d_1 \\ M_{21} &= p_2/d_1 \\ &\vdots \\ M_{m1} &= p_m/d_1 \end{aligned}\right\} \quad d_j = 0 \text{ for } j \neq 1 \ . \tag{27}$$

This process is repeated by driving the remaining bands, one at a time, to fill each column of M.

One must then determine the set of drive levels that best approximates the desired sound field at the field points. This can be accomplished by noting that

$$P = MD \ , \tag{28}$$

where P is a vector of dimension m consisting of the desired pressures at the field points, and D is a vector of dimension n consisting of drives that will produce the desired pressures P. If $m = n$ the drive levels D_i can be computed directly from

$$D = M^{-1} P \ . \tag{29}$$

If $m > n$ one can determine the drives that produce a pressure field that best fits the desired pressure field P in a least-squares sense [35] (i.e., where the squares of the errors are minimized) from [36]

$$D = \left(M^{T*} M\right)^{-1} M^{T*} P \ , \tag{30}$$

where the superscript T indicates transposition and the asterisk indicates complex conjugation. This can be expressed in the simpler form

$$D = \left(M'\right)^{-1} P' \ , \tag{31}$$

where $M' = M^{T*} M$ is the reduced transfer matrix and $P' = M^{T*} P$ is the reduced vector of pressures. It should be noted that if $m > n$, M is not square but M' is always square and hence invertible.

Although the drives computed by this method will mathematically produce the pressure field closest to the desired field (in a least-squares sense), they may not be the most suitable set of drives in practice [37]. The computed drive levels can vary dramatically from one band to the next. In this situation small changes in the drive levels can cause large changes in the uniformity of the resultant pressure field. This places severe demands on the dynamic range and precision of the electronic system used to produce the drives. An example of this condition is presented later.

One solution to this problem was first developed for antenna pattern synthesis [38]. Equation (31) can be expressed as

$$\sum_{j=1}^{n} \left(M'_{ij} D_j \right) = P_i , \qquad i = 1,2,\ldots,n . \tag{32}$$

If a small positive real constant α is added to the diagonal elements of $\boldsymbol{M}'$ one obtains the approximate equation

$$\sum_{j=1}^{n} \left(\alpha \delta_{ij} + M'_{ij} \right) D_j \approx P_i , \qquad i = 1,2,\ldots,n , \tag{33}$$

where δ_{ij} is the Kronecker delta. Although the drive levels tend to decrease as α increases, the larger drive levels decrease more rapidly than the smaller drive levels, thereby creating more uniform drives. Even though these drive levels are no longer the ideal least-squares solution, small values of α often produce drives that are more suitable in practice for creating the desired pressure field. A wide range of values of α will produce a significant improvement in the uniformity of the drive levels with only slight degradation of the uniformity of the pressure field. In practice an α that is one-thousandth the average amplitude of the $\boldsymbol{M}'$ elements usually gives good results.

Utilizing this technique, the solution for $\boldsymbol{D}$ then becomes

$$\boldsymbol{D} = \left(\alpha \boldsymbol{I} + \boldsymbol{M}' \right)^{-1} \boldsymbol{P}' , \tag{34}$$

where $\boldsymbol{I}$ is a unit matrix. It should be noted that once $\boldsymbol{M}'$ is determined for a particular frequency, a set of drives for any desired field can be acquired by resolving Eq. (34) with the appropriate values for $\boldsymbol{P}$ and therefore $\boldsymbol{P}'$.

Computer Program to Model the CWC and Determine Band Drives

As noted above, the drives for the bands can be calculated from a transfer matrix for the system that is determined by either measuring the pressures within the CWC as each band is driven or by using a computer model of the CWC and calculating the predicted pressures using the model. An overall view of the prototype PVDF CWC is shown in Fig. 4. The piezoelectric element of the CWC consisted of a PVDF tube with an inner radius of 1.55 cm, a wall thickness of 0.75 mm and an overall length of 25.2 cm. The PVDF was electroded on the inside and outside of the tube in such a way that it could be electrically driven as 40 bands, each having a width of 6 mm, with an additional grounded band at each end of the tube. A FORTRAN program called CWCMDL was written to model the CWC and calculate the drives using three different methods of determining the transfer matrix. The first method utilizes a CHIEF model of the CWC specifying an interior-wall impedance. The second method models the bands of the CWC as thin-walled piezoelectric rings and includes the effects of fluid loading by using a radiation-impedance matrix computed with CHIEF. The third method utilizes the ATILA finite-element code coupled with CHIEF to include the effects of the fluid.

CWC Models Using Only CHIEF

CHIEF [39,40] is a computer program written in FORTRAN that computes the acoustic radiation from arbitrarily-shaped radiating bodies. The program consists of a collection of subroutines that are called by a user-written control program. CHIEF utilizes the fact that the pressure and velocity can be

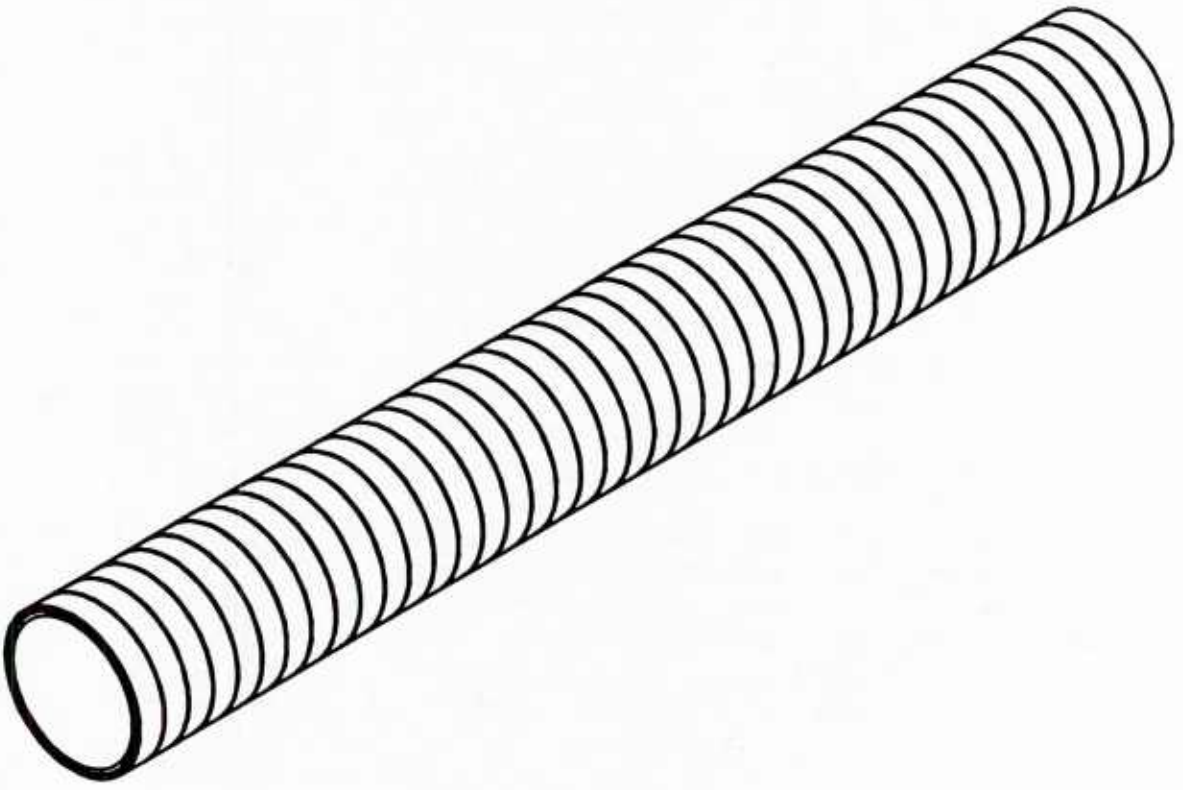

Fig. 4 — Prototype PVDF CWC.

related through the classical Helmholtz integral equation [41,42]

$$\iint_S \left(p(\sigma) \frac{\partial}{\partial n_\sigma} \frac{\exp[-ikr(x,\sigma)]}{r(x,\sigma)} + i\omega\rho v(\sigma) \frac{\exp[-ikr(x,\sigma)]}{r(x,\sigma)} \right) dS(\sigma) \tag{35}$$

$$= \begin{cases} 0 \ , \ x \text{ interior to } S \\ 2\pi p(x), \ x \text{ on } S \\ 4\pi p(x), \ x \text{ exterior to } S \end{cases} ,$$

where S is the radiating surface, $\partial/\partial n_\sigma$ is the outward-normal derivative, $r(x,\sigma)$ is the distance between the surface point σ and the field point x, ω is the radial frequency, and ρ is the fluid density.

The operation of CHIEF can be divided into two basic parts:

- With the normal surface velocity specified, calculate the surface pressure using the Helmholtz integral equation at the surface.
- Calculate the pressure at any point in the surrounding medium using the Helmholtz integral for the surrounding medium.

To solve the Helmholtz integral equation, the surface is divided into N subdivisions over which the pressure and normal velocity are considered to be constant. The Helmholtz integral equation at the surface is then reduced to a system of N complex linear equations in N unknowns. CHIEF can handle

arbitrarily shaped bodies, but a subroutine is provided which simplifies the process for many common geometries [43]. Symmetry can be utilized to reduce the number of required subdivisions. CHIEF requires the numerical solution of $2N^2$ surface integrals. The system is then solved for the surface pressures at each of the N subregions.

There are certain frequencies called "characteristic frequencies" for which the solution of the Eq. (35) is not unique [44]. These frequencies are those for which there exists a nontrivial function satisfying the Helmholtz equation throughout the volume enclosed by the radiating surface and vanishing at the radiating surface.

Schenck proposed a solution to this problem which is utilized by CHIEF [39]. Since the solution to the integral equation is not unique at certain frequencies, unique solutions can be obtained by placing additional constraints on the pressure. CHIEF requires that Eq. (35) be satisfied for points interior to S that are specified by the user. CHIEF then uses a Householder-reduction least-squares technique [45] to compute the surface pressures.

There remains the problem of determining how many interior points are required and where to position them. CHIEF includes a point-source check [46] to help determine the validity of its results. This check allows the user to define one or more point source locations. Normal surface velocities for each of the N surface subdivisions are assigned that coincide with the normal velocity that would be generated at the location of the subdivisions by the point sources if the vibrating body were absent. The surface pressures are also computed by CHIEF from Eq. (35). These surface pressures are then compared with the pressures that would be generated at the location of the surface subdivisions by the point sources in the absence of the vibrating body. The point-source check can help determine whether sufficient interior points are specified and if the surface subdivision scheme is adequate and correct. However, the point-source check can lead to erroneous conclusions if the velocity distribution due to the point sources varies too much from the velocity distribution that normally exists on the surface. These potential problems indicate that the results from CHIEF require careful analysis.

The prototype CWC's largest internal dimension (i.e., its length) is 25.2 cm. The lowest characteristic frequency for the CWC's internal modes is approximately 3 kHz, which is above its operating frequency. This eliminates the problem of frequencies associated with internal modes for the radiating body and no interior points are needed.

The task of writing a control program that calls the CHIEF subroutines has been greatly simplified with the CHIEF Preprocessor called CID (CHIEF Interactive Driver) [47]. This program allows the user to interactively answer questions about the desired CHIEF analysis and then generates a control program for CHIEF.

A recent enhancement to CHIEF is the capability of calculating the radiation from vibrating bodies for which part of the surface has an arbitrary acoustic impedance rather than a specified normal velocity [48,49]. This feature is used for one model of the CWC. All the CHIEF models of the CWC use 18-fold rotational symmetry about the axis of the CWC.

CWC Model with All Surface Velocities Specified

One CHIEF model of the CWC that CWCMDL utilizes involves the use of CHIEF in the traditional manner (i.e., specifying the normal velocity of every surface element of the radiating body). For this model the CWC is divided into 86 surfaces as shown in Table 1. This table shows a cross section of the wall of the CWC (not to scale). The inside of the CWC is on the left and the outside is on the

Table 1 — Surface numbering and axial positions of the borders of the CHIEF surfaces for the model with all the normal velocities specified.

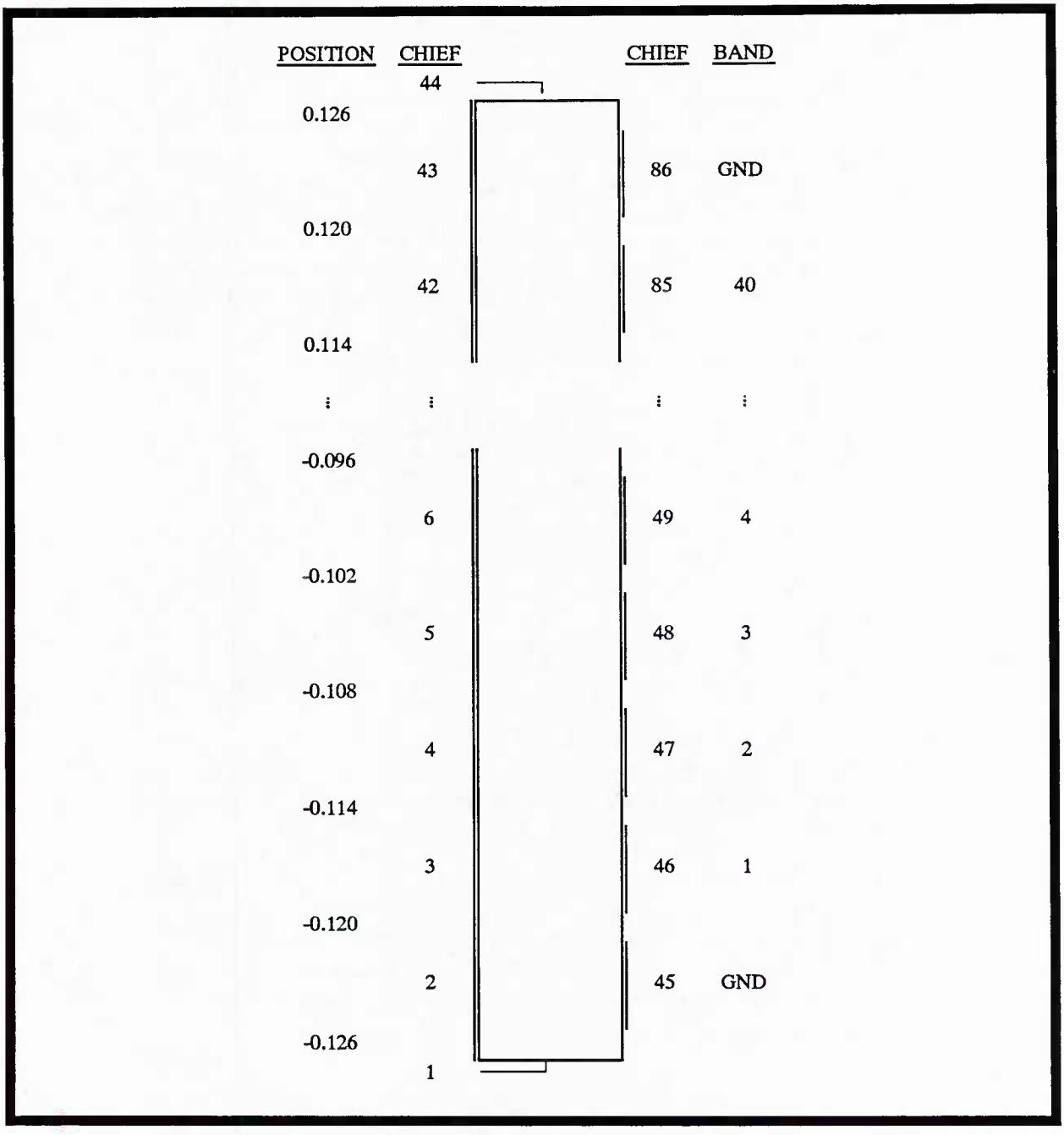

right. The inner radius is 1.55 cm and the outer radius is 1.625 cm. Positions shown are the locations of the divisions between surface elements in meters along the axis of the CWC (the *z* axis) with the origin at the center of the CWC. Surface element widths of 6 mm were chosen to coincide with the 6-mm electrode-band spacing. The electroding is approximated by double lines. The band numbering and CHIEF surface-area numbering are also shown. Since all the normal surface velocities are specified with this model, the description of the surfaces remains the same no matter what surface velocities are specified. This means that the surfaces and the matrices for CHIEF only have to be set up and calculated once for each program run. The field pressures for different sets of velocities can then be calculated without rerunning all of CHIEF. This model is used to determine the field

pressures whenever all the normal surface velocities are known (i.e., after the normal surface velocities have been determined using another model of the CWC).

CWC Model with Interior-Wall Impedance Specified (CHIEF-I)

Another CHIEF model is used to calculate the field pressures when a single band is driven where a surface impedance is specified for the remainder of the interior wall. This model seemed plausible because, while making the pressure measurements within the CWC to determine the resonant frequencies and therefore the propagation speeds with air or water outside the CWC, it was noted that there seemed to be very little coupling between the pressures fields inside and outside of the CWC. It was felt that a simple model that matched the conditions within the CWC reasonably well would give useful results even if the model did not match the conditions well on the outside of the CWC. Since this model ignores the effect of acoustic loading on a driven band it is only used to model the CWC when a single band is driven and therefore cannot be used to model the predicted performance of the CWC when all the bands are driven with a set of computed drives.

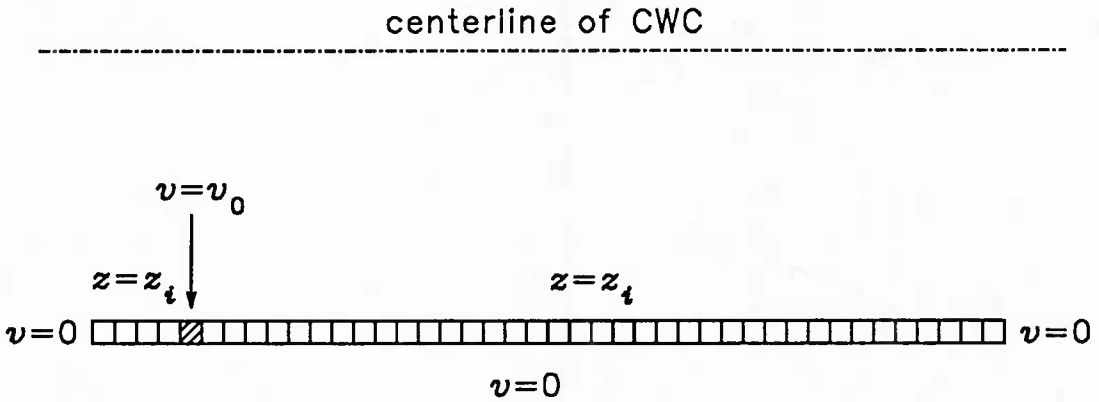

Fig. 5 — Diagram of the CHIEF model of the CWC with a wall impedance specified on the interior of the CWC except for the interior of the driven band.

A diagram of this model is shown in Fig. 5 for band number 4 being driven. (Note: The first band is a ground band, therefore, driven band 4 is the fifth band in from the left.) In this model:

1. The normal velocities on the outside and the end surfaces of the CWC are set to zero.
2. The normal velocity of the inner surface of the driven band v_0 is specified.
3. The surface impedance of the remainder of the interior wall of the CWC z_i is specified.

The interior-wall impedance z_i is calculated from [50]

$$z_i = \frac{Y t_w}{i\omega a^2}, \tag{36}$$

where Y is the Young's modulus, t_w is the wall thickness, and a is the inner radius of the PVDF tube.

CHIEF requires that, if arbitrary impedances are specified instead of normal surface velocities for any of the surfaces, they must be the last surface regions described. Since impedances are specified for the interior wall regions below and above the driven band, they must be the last surfaces loaded. The locations of these surfaces and the inner surface of the driven band change whenever a different band is driven, so these surfaces are reloaded and the matrices recalculated as each different band is driven. This means that CHIEF has to perform more computations to determine the transfer matrix by driving each band with this model than in the model where all the surface velocities are specified.

The CHIEF model of the CWC with specified interior-wall impedances will be referred to as the CHIEF-I model.

RING-CHIEF Model

One limitation of the interior-wall-impedance model of the CWC is the fact that the effects of the acoustic loading on the velocity of the driven band are ignored. Another model of the CWC called RING-CHIEF was created that models the CWC bands as thin-walled piezoelectric rings and includes the effects of the acoustic loading.

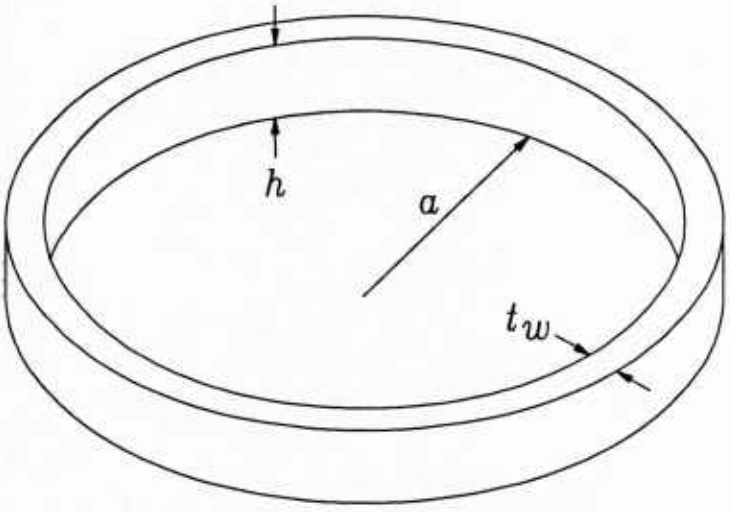

Fig. 6 — Thin-walled piezoelectric ring used for the RING-CHIEF model.

The radiation impedance of a fluid-loaded vibrating surface is the ratio of the force exerted by the surface on the fluid to the normal velocity of the surface [51]. The total force on the vibrating surface also includes the effects of the internal mechanical impedance and the mutual radiation impedances from other surfaces. One can model the bands of the CWC as thin-walled piezoelectric rings with each ring having an inner radius a, a wall thickness t_w, and a height h (see Fig. 6). A coordinate system is used in which 1 is in the circumferential direction and 3 is in the radial direction. Each ring is electroded on the inner and outer surfaces and poled radially. If one assumes that there are N bands, and therefore $2N$ total inner and outer surfaces, the radial force exerted on band i is [52]

$$F_i = Z_m^i v_i + p_{inner}^i A_{inner}^i - p_{outer}^i A_{outer}^i , \tag{37}$$

where

Z_m^i = mechanical impedance of the ith band

v_i = radial velocity of the ith band

p_{inner}^i = pressure on the inner surface of the ith band

p_{outer}^i = pressure on the outer surface of the ith band

A_{inner}^i = area of the inner surface of the ith band

A_{outer}^i = area of the outer surface of the ith band

The pressures on the inner and outer surfaces of the band can be expressed as

$$p^{i}_{inner} = \sum_{j=1}^{2N} G^{i,j} v_j \tag{38}$$

and

$$p^{i}_{outer} = \sum_{j=1}^{2N} G^{i+N,j} v_j \ , \tag{39}$$

where $G^{i,j}$ is a Green's function [53] and v_j is the normal velocity of surface j. If the inner and outer surface areas are written as

$$A^{i}_{inner} = A_i \tag{40}$$

and

$$A^{i}_{outer} = A_{i+N} \ , \tag{41}$$

Eq. (37) can be expressed as

$$F_i = Z^{i}_{m} v_i + \sum_{j=1}^{2N} (G^{i,j} A_i - G^{i+N,j} A_{i+N}) v_j \ . \tag{42}$$

The summation can be divided into separate parts for the inner and outer normal surface velocities giving

$$\begin{aligned} F_i = Z^{i}_{m} v_i &+ \sum_{j=1}^{N} (G^{i,j} A_i - G^{i+N,j} A_{i+N}) v_j \\ &+ \sum_{j=N+1}^{2N} (G^{i,j} A_i - G^{i+N,j} A_{i+N}) v_j \end{aligned} \tag{43}$$

or

$$\begin{aligned} F_i = Z^{i}_{m} v_i &+ \sum_{j=1}^{N} (G^{i,j} A_i - G^{i+N,j} A_{i+N}) v_j \\ &+ \sum_{j=1}^{N} (G^{i,j+N} A_i - G^{i+N,j+N} A_{i+N}) v_{j+N} \ . \end{aligned} \tag{44}$$

Since the bands are assumed to be thin-walled rings, the outer wall normal surface velocities are equal to the negative of the inner wall normal surface velocities

$$v_{j+N} = -v_j \tag{45}$$

giving

$$F_i = Z_m^i v_i + \sum_{j=1}^{N} (G^{i,j} A_i - G^{i+N,j} A_{i+N} - G^{i,j+N} A_i + G^{i+N,j+N} A_{i+N}) v_j \tag{46}$$

or

$$F_i = Z_m^i v_i + \sum_{j=1}^{N} (Z^{i,j} - Z^{i+N,j} - Z^{i,j+N} + Z^{i+N,j+N}) v_j \quad , \tag{47}$$

where the radiation impedance $Z^{ij} = G^{ij} A_i$.

The radiation impedance Z^{ij} is defined as the normal force exerted on surface i when surface j moves with unity normal velocity and all other surfaces have normal velocities of zero. This coincides with the radiation-impedance matrix $[Z]$ that can be computed with CHIEF [54]. Equation (47) can be written as

$$F_i = \sum_{j=1}^{N} Z_{tot}^{ij} v_j \ , \tag{48}$$

where

$$Z_{tot}^{ij} = \begin{cases} Z^{i,j} - Z^{i+N,j} - Z^{i,j+N} + Z^{i+N,j+N} & , \quad j \neq i \\ Z^{i,i} - Z^{i+N,i} - Z^{i,i+N} + Z^{i+N,i+N} + Z_m^i & , \quad j = i \end{cases} . \tag{49}$$

Equation (48) can then be expressed in matrix notation as

$$\bar{F} = [Z_{tot}] \, \bar{V} \ , \tag{50}$$

where

$\bar{F}$ = vector of the normal surface forces
$[Z_{tot}]$ = total impedance matrix
V = vector of the normal surface velocities

This system can be solved for the resultant velocities for a set of specified forces.

The strain in a thin-walled ring can be expressed as [55]

$$S_1 = s_{11}^E T_1 + d_{31} \varepsilon_3 \quad , \tag{51}$$

where

s_{11}^E = elastic compliance coefficient with constant electric field
T_1 = circumferential stress
d_{31} = piezoelectric strain coefficient
ε_3 = electric field

Considering the blocked case (i.e., $S_1 = 0$) and noting that s_{11}^E is the reciprocal of Young's modulus [56] Y, Eq. (51) becomes

$$T_1 = -d_{31}\,\varepsilon_3 Y\,. \tag{52}$$

This stress exerts a radial force on the ring of [55]

$$F_i = -2\pi h t_w T_1\,. \tag{53}$$

Substituting Eq. (52) into this gives

$$F_i = 2\pi h t_w d_{31}\,\varepsilon_3 Y\,. \tag{54}$$

If a voltage E_i is applied across the electrodes, the fact that $\varepsilon_3 = E_i/t_w$ gives a force of

$$F_i = 2\pi h d_{31} Y E_i\,. \tag{55}$$

The internal mechanical impedance of the thin ring can be expressed as [57]

$$Z_m = i\left(\omega M - \frac{1}{\omega C_m}\right), \tag{56}$$

where $M = 2\pi\rho a h t_w$ is the mass of the ring and $C_m = a/(2\pi h t_w Y)$ is the mechanical compliance of the ring.

The normal surface velocities of all the surfaces when a single band is driven can be computed from Eq. (50) by setting $F_i = 0$ for all bands except the driven band. The force on the driven band is given by Eq. (55). The system in Eq. (50) is then solved for the velocities. A FORTRAN program was written to compute the necessary quantities and solve the resultant system for the surface velocities. The model is implemented by driving the first band alone with $E_1 = 1$ and solving for the resultant normal surface velocities, which are then stored in a file. This process is repeated for each of the driven bands through band 20 with each set of resultant surface velocities appended to the velocity file. Since the CWC is symmetric, the resultant surface velocities for drives to bands 21 through 40 can be obtained from the results for bands 1 through 20. The file containing the resultant surface velocities for unity drive to each of the first twenty bands is then used to calculate all the surface velocities for any set of band drives. This is accomplished by multiplying the complex contribution to each surface velocity for unity drive to each band by the complex drive to that band. The complex velocities are then summed for all driven bands to give the resultant velocities.

ATILA-CHIEF Model

In order to obtain a more complete model of the PVDF CWC, the ATILA finite-element code was used. This model includes structural interaction within the PVDF tube and the effects of the fluid. ATILA was specifically developed to aid in the design of sonar transducers, but can be used for other types of transducers or for passive structures. If one first considers the harmonic analysis of the CWC in vacuum (i.e., without any effects of fluid loading), the matrix equation describing the problem can be written as [58]

$$\begin{bmatrix} [K_{uu}] - \omega^2[M] & [K_{u\phi}] \\ [K_{u\phi}]^{\mathrm{T}} & [K_{\phi\phi}] \end{bmatrix} \begin{bmatrix} \boldsymbol{U} \\ \Phi \end{bmatrix} = \begin{bmatrix} \boldsymbol{F} \\ -q \end{bmatrix}, \tag{57}$$

where

$[K_{uu}]$	=	stiffness matrix
$[K_{u\phi}]$	=	piezoelectric matrix
$[K_{\phi\phi}]$	=	dielectric matrix
$[M]$	=	mass matrix
$\boldsymbol{U}$	=	vector of the nodal values of the displacement field
Φ	=	vector of the nodal values of the electrical potential
$\boldsymbol{F}$	=	vector of the nodal values of the applied forces
$\boldsymbol{q}$	=	vector of the nodal values of the electrical charges

and superscript T indicates matrix transposition. For a structure that is in contact with a fluid medium the force vector $\boldsymbol{F}$ can be written as [59]

$$\boldsymbol{F} = \boldsymbol{F}^R + \boldsymbol{F}^D \ , \tag{58}$$

where $\boldsymbol{F}^R$ is associated with the acoustic loading of the fluid medium and $\boldsymbol{F}^D$ is associated with the other known forces that drive the structure.

The effects of the fluid loading can then be included by using the radiation-impedance matrix that relates forces and velocities on the wetted surfaces by [60]

$$[Z]\,\overline{V} = \overline{F} \ , \tag{59}$$

where

$[\underline{Z}]$	=	radiation-impedance matrix
$\underline{V}$	=	vector of the normal surface velocities
$\overline{F}$	=	vector of the normal surface forces

The nodal forces $\boldsymbol{F}^R$ can be expressed in terms of the normal surface force for surface S_i by [61]

$$F_i^R = -\frac{\overline{F_i}}{A_i} \int_{S_i} [N_{ei}]^{\mathrm{T}} \cdot \boldsymbol{n}_i \, dS_i \tag{60}$$

or

$$F_i^R = -\overline{F_i} \pi_i^e \ , \tag{61}$$

where

$$\pi_i^e = \frac{1}{A_i} \int_{S_i} [N_{ei}]^T \cdot \boldsymbol{n}_i \, dS_i \,, \tag{62}$$

A_i = area of surface S_i
$[N_{ei}]$ = interpolation function
$\boldsymbol{n}_i$ = normal unit vector for surface S_i

The π_i^e can be reordered in a larger vector π_i containing all the degrees of freedom. A coupling matrix $[X]$ can be defined as

$$[X] = [\pi_1, \pi_2, \ldots, \pi_n] \,, \tag{63}$$

where n is the total number of wetted surfaces. The nodal forces are related to the nodal displacements by

$$\boldsymbol{F}^R = -i\omega [X][Z][X]^T \boldsymbol{U} \,. \tag{64}$$

The finite-element model then becomes [62]

$$\begin{bmatrix} [K_{uu}] - \omega^2 [M] + i\omega [X][Z][X]^T & [K_{u\phi}] \\ [K_{u\phi}]^T & [K_{\phi\phi}] \end{bmatrix} \begin{bmatrix} \boldsymbol{U} \\ \Phi \end{bmatrix} = \begin{bmatrix} \boldsymbol{F}^D \\ -q \end{bmatrix} . \tag{65}$$

After solving this set of equations, the normal velocities of the wetted surfaces are computed from

$$\boldsymbol{V} = -i\omega [X]^T \boldsymbol{U} \,. \tag{66}$$

CHIEF can then be used to compute field pressures using the normal surface velocities.

ATILA incorporates an option that will read a radiation-impedance matrix file created by CHIEF and compute the resultant normal velocities of the wetted surfaces. Care must be taken to describe the radiating body in CHIEF and ATILA in such a way that the surfaces in CHIEF correspond to the appropriate elements in ATILA.

The procedure for calculating field pressures using the ATILA-CHIEF model is therefore:

1. Run CHIEF to calculate and store the appropriate radiation-impedance matrix.
2. Run ATILA with appropriate boundary conditions. ATILA uses the radiation-impedance matrix and calculates the resultant normal surface velocities.
3. Run CHIEF (specifying the normal surface velocities determined with ATILA) to calculate the resultant field pressures.

An ATILA-CHIEF model of the CWC was created utilizing the axial symmetry. The flow diagram for the model is shown in Fig. 7. The region inside the dashed lines is labeled GEOMETRY DEPENDENT to signify that it only depends on the physical parameters of the system (e.g., dimensions, material properties, frequency, etc.). Therefore, the ATILA-CHIEF computation only has to be performed once for a particular set of physical parameters. The results can then be used to determine all the surface velocities for any set of band drive voltages. Once the surface velocities are

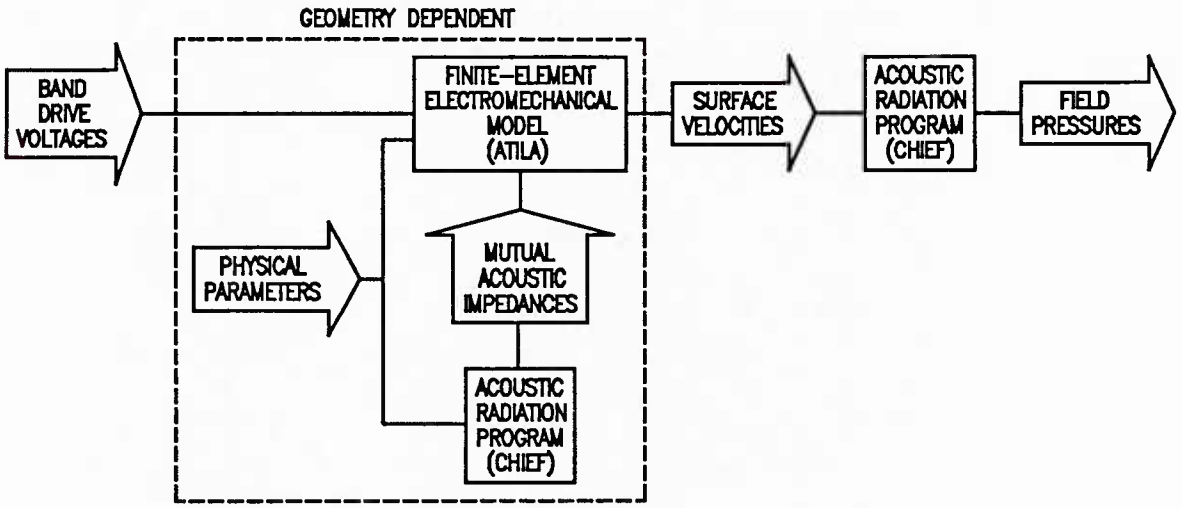

Fig. 7 — Flow diagram of the ATILA-CHIEF CWC model.

known, CHIEF can then be used to determine the field pressures. This method is analogous to the method used with the RING-CHIEF model. The model was implemented by setting up a CHIEF model of the CWC that matches the ATILA model. This CHIEF model creates a radiation-impedance file. ATILA is then run (accessing the radiation-impedance file) with the first driven band having unity drive voltage applied to its outer electrode and zero volts applied to the inner electrode and to all the other outer electrodes. The resultant surface velocities output by ATILA are then stored in a file. This process is repeated (as with the RING-CHIEF model) for each of the driven bands through band 20 with each set of resultant surface velocities appended to the velocity file.

In order to give the finite-element model a finer grid and give a more conservative aspect ratio for the fairly thin-walled tube (i.e., to reduce the ratio of the longest dimension of an element to its shortest dimension), compatible CHIEF and ATILA models of the CWC were created where each 6-mm-wide band is divided into two 3-mm-wide regions. This CHIEF model has 170 surface areas instead of the 86 for the 6-mm model. Although this significantly increases the computation time, this CHIEF run only has to be performed once for each drive frequency with a specified set of physical parameters to compute the radiation-impedance matrix. The positions of the ATILA nodes and CHIEF surfaces for these models are given in Table 2. The ATILA model utilizes axial symmetry and was generated with the aid of the MOSAIQUE Automatic Mesh Generator that is part of the ATILA package. The model consists of 84 eight-node, isoparametric, quadrilateral (QUAD08P) elements [63]. These elements are designed to model any piezoelectric material. The QUAD08P elements run from the bottom to the CWC to the top with the first element having nodes 1, 2, 3, 171, 257, 256, 255, and 170. The CHIEF model is coupled to the ATILA model by the use of 170 three-node isoparametric (LINE03Z) elements [64]. These elements are used to couple the ATILA model with the radiation-impedance matrix output by CHIEF and are superimposed on the radiating surfaces of the mesh of the solid structure (one for each CHIEF surface area). The LINE03Z elements run counterclockwise around the surface with the first element having nodes 255, 256, and 257. The ATILA model has a total of 423 nodes, as shown in Table 2.

The output of the ATILA-CHIEF model is average normal surface velocities for the two end surfaces and the 168 surfaces of the 3-mm wide regions. A FORTRAN program was written to convert these into velocities for the 86 surface areas as used in the RING-CHIEF model where each band surface velocity is the average of the two 3-mm regions spanning the band.

Table 2 — Numbering and axial positions of ATILA nodes and CHIEF surface borders for the ATILA-CHIEF model.

POSITION	CHIEF	NODES			CHIEF	BAND
	85					
0.2520		169	254	423		
0.2505	86	168		422	84	
0.2490		167	253	421		GND
0.2475	87	166		420	83	
0.2460		165	252	419		
0.2445	88	164		418	82	
0.2430		163	251	417		40
0.2415	89	162		416	81	
0.2400		161	250	415		
⋮	⋮	⋮	⋮	⋮	⋮	⋮
0.0300		21	180	275		
0.0285	160	20		274	10	
0.0270		19	179	273		4
0.0255	161	18		272	9	
0.0240		17	178	271		
0.0225	162	16		270	8	
0.0210		15	177	269		3
0.0195	163	14		268	7	
0.0180		13	176	267		
0.0165	164	12		266	6	
0.0150		11	175	265		2
0.0135	165	10		264	5	
0.0120		9	174	263		
0.0105	166	8		262	4	
0.0090		7	173	261		1
0.0075	167	6		260	3	
0.0060		5	172	259		
0.0045	168	4		258	2	
0.0030		3	171	257		GND
0.0015	169	2		256	1	
0.0000		1	170	255		
	170					

CWCMDL Program

The FORTRAN computer program CWCMDL is used to calculate sets of band drives that can be used to generate evanescent pressure fields within the CWC. The program uses the method described earlier to determine the complex band drives from transfer matrices computed with either CHIEF-I, RING-CHIEF, or ATILA-CHIEF. The program can also compute the predicted pressure field within the CWC from a specified set of band drives using either RING-CHIEF or ATILA-CHIEF.

The parameters that are required by CWCMDL for each run are contained in a text file. The

program reads the parameters from the input file and then performs the necessary computations. A more detailed description of CWCMDL is given in Appendix B.

EXPERIMENTAL SETUP

To evaluate the performance of a PVDF CWC a prototype was constructed with 40 driven bands. An experimental setup was designed and constructed that allowed operation of the CWC prototype with water on the inside and with either air or castor oil on the outside. It was desirable to investigate both of these configurations because a full sized CWC might be more easily constructed if it were air backed. However, if pressurized operation were required (i.e., to simulate conditions deep underwater), a full sized CWC might be enclosed in a liquid-filled pressure vessel. Independently controlled electronic drives were supplied for up to 40 bands. An electronic measurement system was constructed and software written to accurately map the acoustic pressure within the CWC.

CWC Array

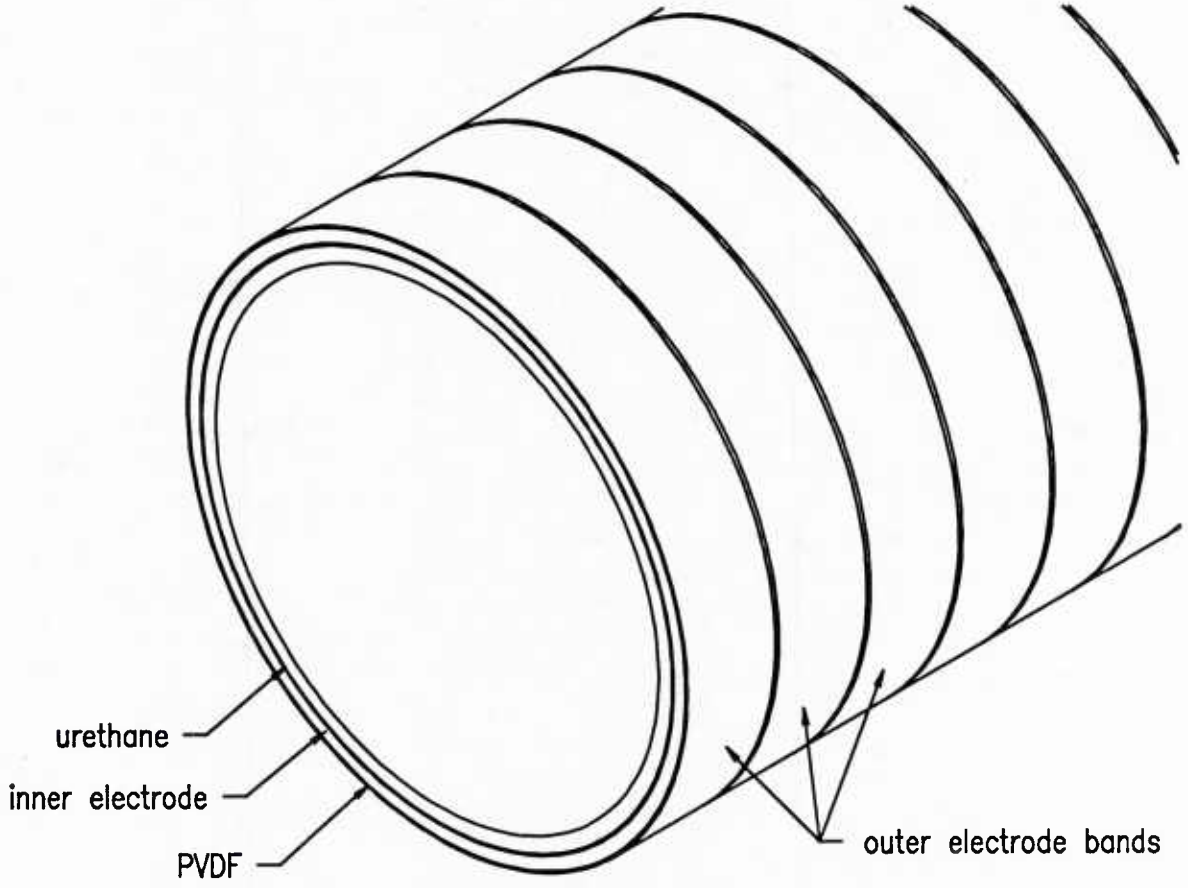

Fig. 8 — Construction details of the PVDF CWC.

A prototype CWC was constructed using a PVDF tube as the active element. The CWC consists of (from the inside to the outside, see Fig. 8); (1) a urethane coating, (2) an inner (ground) electrode, (3) a PVDF tube, and (4) the outer electrodes.

A piezoelectric PVDF tube was acquired from THORN-EMI. PVDF is a fluorocarbon polymer

that is used in a wide range of applications from wiring insulation to chemical storage containers. It can be easily extruded into sheets and tubes. The PVDF has very little piezoelectric activity when it is extruded. The piezoelectric properties are dramatically enhanced by first stretching the PVDF and then applying a large electric field across the sheet (or tube wall) under elevated temperature [65]. The PVDF tube was supplied with thin copper electrodes covering all of the inside and outside surfaces. The tube has an inner radius of 1.55 cm, an outer radius of 1.625 cm, and a length of 25.2 cm. A tube of these dimensions was used because it has the largest radius and length that could be supplied at the time. However, the manufacturer feels that there would be no serious technical problems involved in producing tubes several times this size -- provided that there was sufficient incentive for the investment in additional equipment. Insulator bands were then formed on the outer side of the tube by machining away narrow strips of the outer electrode. It was not necessary to divide the inner electrode into separate bands because it was used as the common ground electrode for all bands. This process created 40 independent outer electrode bands with band spacing of 6 mm and an additional grounded band at each end approximately 6-mm wide. The ground bands are electrically connected to the inner electrode with fine wires and conductive epoxy. This provides for electrical connections to the inner (ground) electrode from the outside of the tube.

Urethane (Eccobond 45) end collars and an approximately 1.5-mm-thick layer of urethane were then cast on the inside of the array for waterproofing. The end collars are provided so that the CWC can be fitted snugly into a Lexan box (described later) and sealed to prevent leaks. A wiring harness is attached to the outer bands of the array with conductive epoxy providing electrical connections from the drive electronics.

Drive Electronics

The electrical band drives for the CWC are supplied by a drive system [66] that provides for 40 channels of simultaneous sinusoidal drive with independently controlled amplitudes and phases at any specified frequency between 100 and 2000 Hz. The system is capable of providing drive levels up to 1000 V peak-to-peak. The hardware is controlled by software on a VAX computer. The drive for each channel is produced by first loading the drive system's internal memory with data representing one or more sine waves at the desired amplitude and phase for each channel. Each channel has a separate digital-to-analog converter (DAC). The sinusoidal output is produced by reading the sine-wave information stored in memory and passing the data through each channel's DAC. The frequency at which the DACs operate is adjusted so that a continuous sinusoidal output is sustained. The DAC output is filtered to remove the DAC frequency component and smooth the desired sinusoidal output; then if applied to a power amplifier that develops the high voltage drive. This process is multiplexed to drive all the channels simultaneously. In the above mentioned process, one sine wave is loaded in memory for each channel unless this would force the system to operate at a higher clock rate than allowed. In this case enough sine waves are loaded in memory to reduce the required clock rate to an acceptable value.

Measurement Setup

A measurement setup and rigging were designed that allow accurate measurement of the acoustic pressure within the CWC with either air or liquid outside the PVDF array. The measurement setup and water tank used for the measurements are shown in Figs. 9 and 10. The measurement setup consists of: (1) a LEXAN box containing the CWC, (2) a hydrophone, (3) a computer-controlled, single-axis positioner and yoke assembly, (4) a water tank, (5) a rigging assembly that mounted the LEXAN box and positioner in proper alignment on the tank.

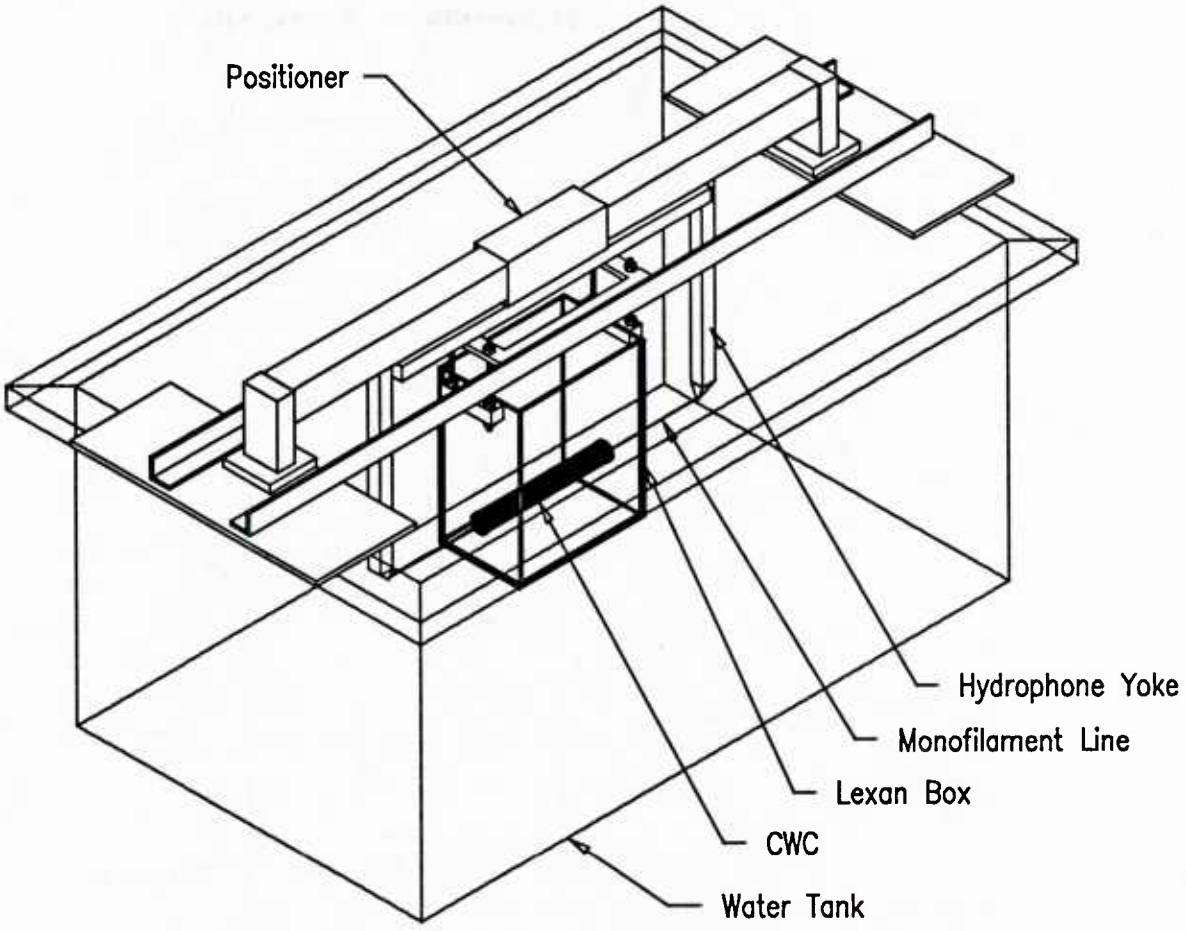

Fig. 9 — Measurement setup and water tank.

CWC Mounting Box

The LEXAN box that was designed and constructed to mount the CWC is shown in Fig. 11. It is constructed from 6.35-mm-thick LEXAN sheets cemented together and is 31.0-cm high by 16.5-cm wide by 25.8-cm long to accommodate the length of the CWC. The box was designed with holes in the two end walls that are snug fits with the urethane collars at the ends of the CWC. When the CWC is inserted into the holes in the box, and the box is partially submerged in water, the inside of the CWC is flooded with water. The box can then either be left empty to provide an air-backed configuration for the CWC or filled with castor oil to provide a liquid-backed configuration. Castor oil is used, instead of water, because it is a good insulator and therefore does not cause shorting across the outer electrodes. The box is equipped with mounting hardware so that the box, and therefore the CWC, can be accurately aligned with the positioner assembly.

Hydrophone

The hydrophone used was a Brüel & Kjær (B&K) Miniature Hydrophone Type 8103. This hydrophone has a cylindrical piezoelectric element with an outer diameter of 7 mm and a length of 8 mm. A somewhat smaller hydrophone that was available (Atlantic Research LC-5) was used in some

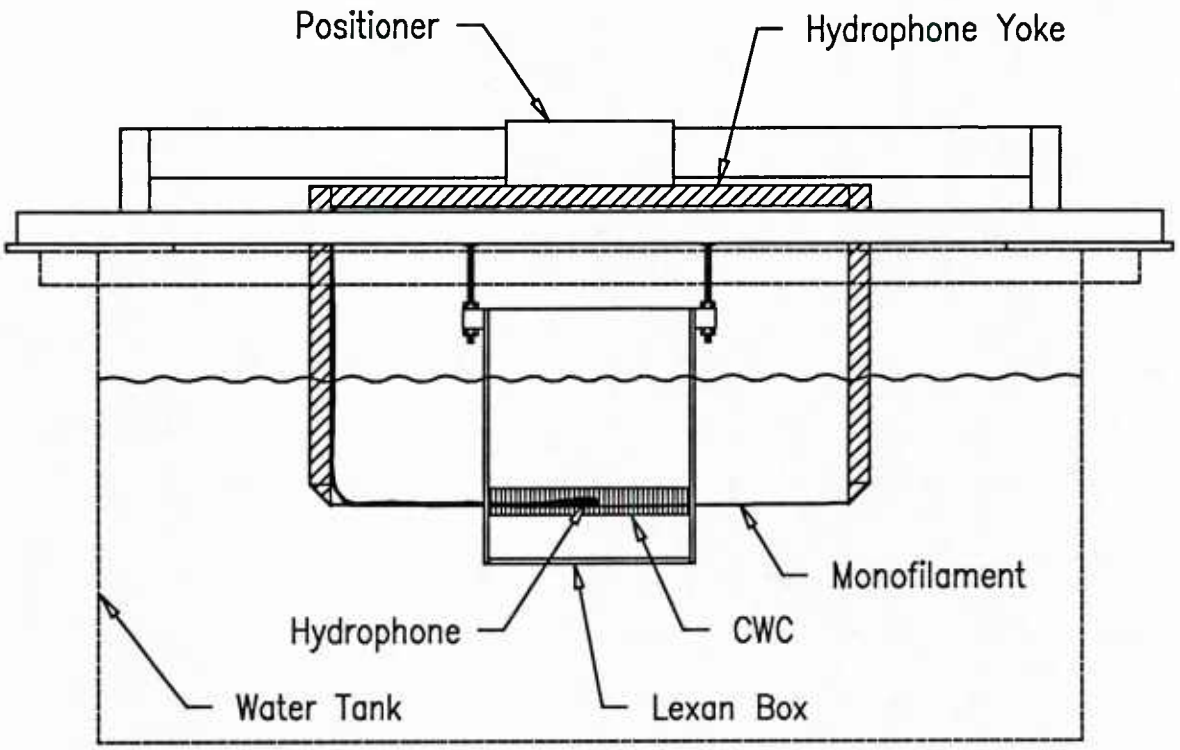

Fig. 10 — Cross-section view of measurement setup and rigging.

early measurements with the CWC but was abandoned in favor of the B&K 8103 because the 8103's higher pressure sensitivity gave more usable signals when the CWC was operated with low drive voltages. The low drive voltages were deemed prudent because the first prototype CWC was destroyed when arcing occurred across the outer electrodes. A B&K 8103 had also been successfully used in measurements with a planar wavenumber calibrator having the same electrode spacing and generating evanescent fields in the same frequency and wavenumber regions that are intended for the prototype CWC [19].

The hydrophone is attached to a monofilament line that is strung tightly through the center of the CWC (see 10). The line is attached to a yoke assemble that in turn is attached to the traveling head on the positioner. This allows positioning of the hydrophone anywhere within the CWC with a minimum amount of rigging within the CWC. The positioner can then automatically position the hydrophone anywhere along a line running through the CWC (usually along the axis of the CWC).

Positioner

The positioner is a Klinger Positioning Stage with a UE72 Stepping Motor. It is controllable either manually with a Klinger CC1.1 Programmable Stepping Motor Controller or remotely by commands sent to the controller via a GPIB-488 interface. The positioner and yoke assembly can position the hydrophone throughout the length of the CWC and up to 1.5 cm beyond the ends with steps as small as 0.0254 mm (0.001 in.).

Water Tank

The water tank is made of fiberglass and is reinforced by a steel and wood frame. The tank

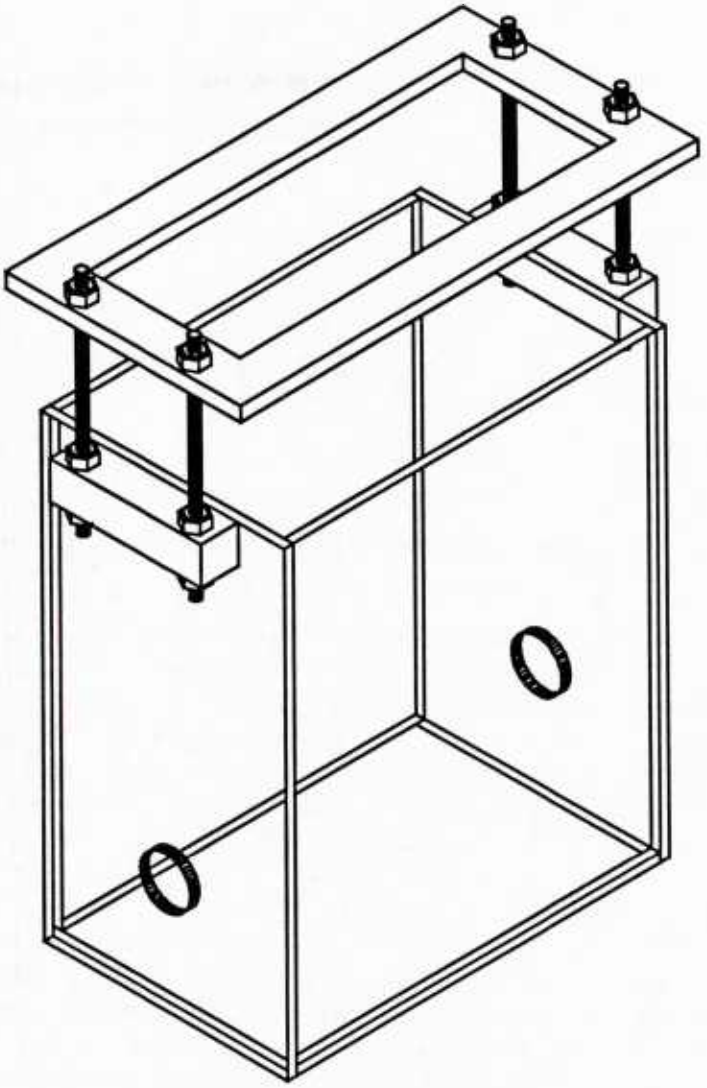

Fig. 11 — LEXAN CWC mounting box and rigging.

measures 120×60×60-cm deep and is supported on air bags to minimize coupling of structural vibrations. During measurements the tank is typically filled to a depth of 45 cm and the CWC is submerged to a depth of at least 15 cm.

Electronic Measurement System

An electronic measurement system was constructed and software written to accurately map the pressure field (both amplitude and phase) within the CWC.

Measurement System Hardware

A block diagram of the measurement system is shown in Fig. 12. The system is controlled by a PC-compatible microcomputer. The PC can control the motion of the positioner, and therefore the hydrophone, by issuing commands over the General Purpose Interface Bus (GPIB) to the positioner

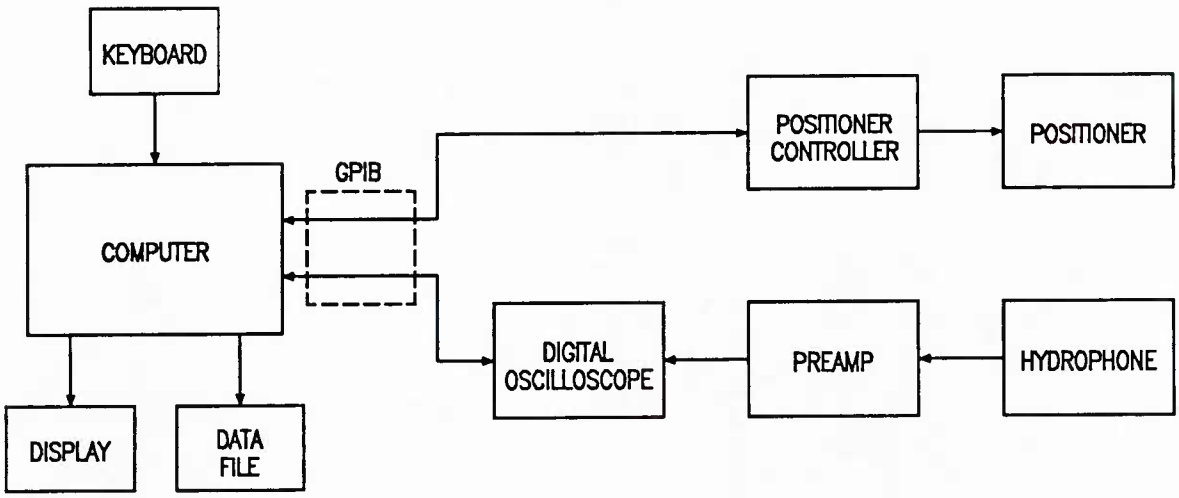

Fig. 12 — Diagram of the measurement system.

controller. The signal from the hydrophone is amplified by an EG&G-PARC Model 113 preamplifier and then captured on a Nicolet Explorer III digital oscilloscope. Additional filtering is sometimes used between the preamplifier and the digital oscilloscope. The other channel of the oscilloscope is used to monitor a reference signal. The data from the oscilloscope is transferred over the GPIB to the PC for processing. The PC displays and records the position of the measurement and the amplitude and relative phase of the signal from the hydrophone. The phase relative to the reference signal is determined by performing a single-frequency discrete-Fourier-transform [67,68] on each of the signals.

Measurement System Software

A QuickBASIC program called CWCMAP was written for the PC to control the positioner and oscilloscope and to determine the amplitude and phase of the signals captured by the oscilloscope. The program first presents the user with a menu (see Fig. 13) allowing the entry of required information such as the first and last positions of the hydrophone and the distance between data points for mapping the pressure field. The user also enters the drive frequency and the name of the data file that is to receive the position and pressure data.

The procedure used to map the pressure field within the CWC is:

- Enter the appropriate parameters (e.g., frequency, band drive amplitudes and phases, etc.) with the drive system software on the VAX.
- Instruct the VAX to start the drive system and apply the appropriate drives to the CWC.
- Enter the appropriate mapping parameters with the measurement system software on the PC
- Instruct the measurement system PC to start the map of the pressure field.

During the measurement process one channel of the digital oscilloscope is connected to the output of the preamplifier while the other channel is connected to one of the drive system outputs to provide a phase reference to determine the relative phase of the pressure signal. The measurement software then maps the pressure field by moving the positioner to the specified measurement positions and at each position:

- Captures the hydrophone and reference signals on the digital oscilloscope.

```
                Cylindrical Wavenumber Calibrator
                  Pressure-Field Mapping Program
                       L.D. Luker  NRL/USRD


      1. Position of origin:       -15.25
      2. First mapping position:   -14
      3. Mapping step size:        .5
      4. Last mapping position:    14
      5. Frequency:                800
      6. Data path:                B:
      7. Data filename:            CWCDAT.PRN
      8. Annotation:               CWCMAP data


      Press the item number to change or a function key:



 F1      F2      F3      F4      F5      F6      F7      F8      F9      F10
HELP    FILES   CAL     MATRIX  MAP             PLOT                    EXIT
```

Fig. 13 — Menu screen for the CWC measurement software.

- Transfers the data to the PC.
- Determines the amplitudes and phases of the signals.
- Records the hydrophone position and amplitude of the hydrophone signal and its phase relative to the reference signal.These data are then written to the specified data file.

EXPERIMENTAL RESULTS

The goal of the research presented in this thesis was to investigate the characteristics of the PVDF CWC prototype. This included the calculation of sets of band drives that could be used to produce evanescent pressure fields within the CWC. Several methods were used to determine the transfer matrix for the system. The performance of the CWC was then evaluated for each of the different methods of determining the transfer matrix. This section describes the measurements that were made and presents the results of those measurements.

Calibration of the Drive System

A technique was devised to improve the accuracy of the electrical drives to the CWC bands by correcting for errors in the drive system. These errors exist because of variations in the performance of the electronic modules from channel to channel. The bands are first driven at uniform amplitude with a 10° phase increment between each succeeding band. The amplitudes and phases of the voltages at the connections on the bands are then measured and recorded using the measurement system. The 10° phase increment between bands (rather than uniform phase) is used to assist in detecting swapped connections in the drive system or CWC wiring harness and misdirection of drives by the drive-system software. A FORTRAN program was written that will read a set of desired drives from a file, correct the drives to cancel out the measured drive system errors, and write the corrected drives to a file that can then be loaded directly into the drive system. Plots of a typical set of drive system errors

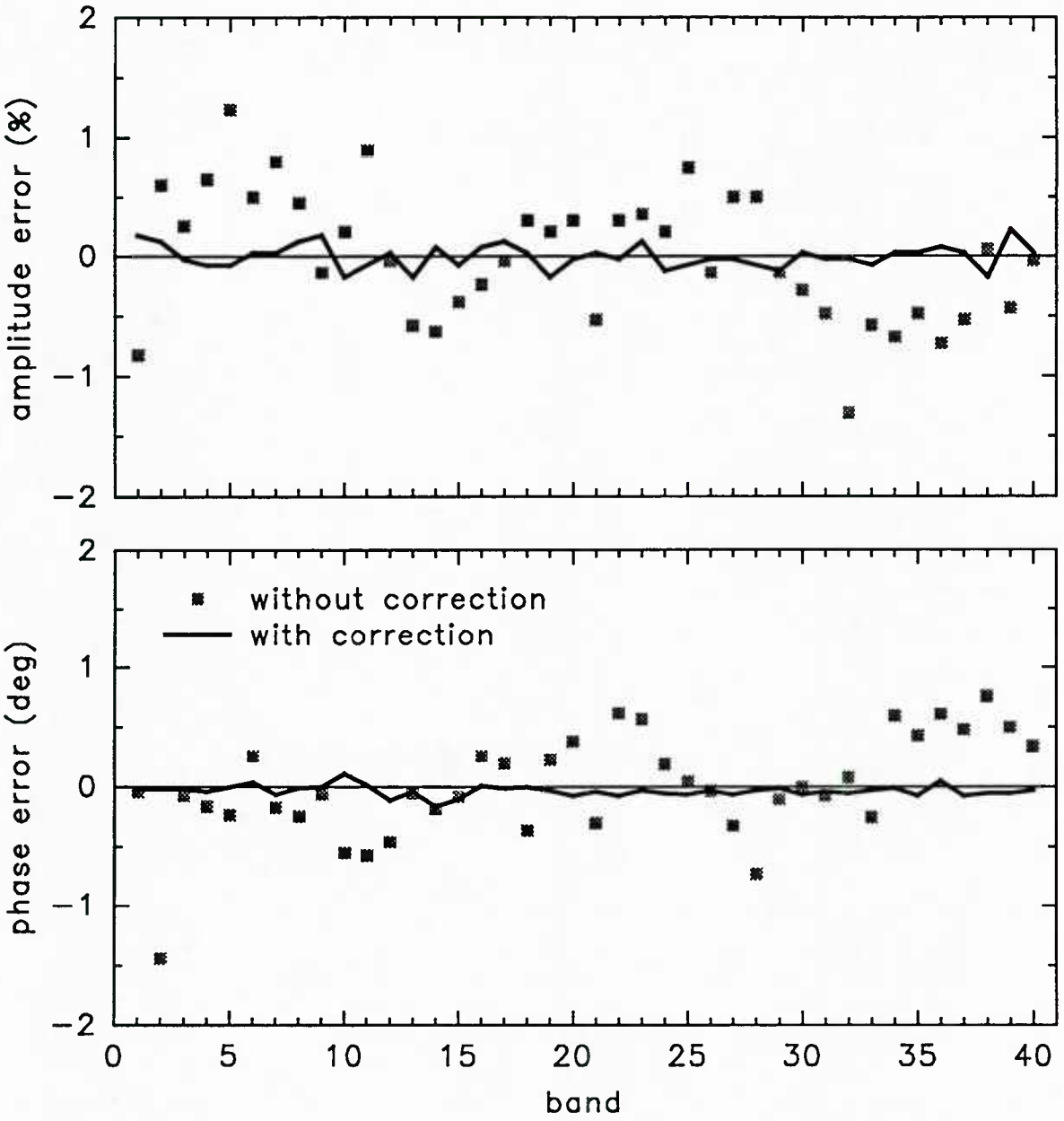

Fig. 14 — Amplitude and phase errors at the band connections for 800 Hz drive with and without the drive system error corrections.

measured directly at the band connections at 800 Hz (without and with the corrections) are shown in Fig. 14. The results show a significant improvement in the accuracy of the band drives. The small errors remaining after the corrections give an indication of the accuracy of the electronic measurement system. This system is able to reproduce measurements with amplitude errors within ±0.4% and phase errors within ±0.3°. Although little variation has been observed in the corrections required at a given frequency (unless some of the electronics are replaced), the calibration process is repeated before each measurement session to insure that all the band drives are functioning properly. The drive-correction program is then run to correct and load each set of desired drives.

Measured-Transfer-Matrix Method

One method used for determining the transfer matrix for the system is to actually measure it. This is probably the most accurate method, if done carefully, since the only errors involved are measurement errors. Unlike the other methods presented, it does not rely on a model of the an idealized CWC (i.e., in the models all the bands are assumed to exactly match the dimensions specified, have perfectly uniform material properties, etc.). The measured transfer matrix includes the effects of any imperfections in the actual array. For example, if, because of manufacturing irregularities, some of the bands have dimensional variations or slightly larger piezolelectric coefficients than others, the effects of this are included in the measured transfer matrix. Since any such imperfections will effect the evanescent field, it is advantageous to have them included in the transfer matrix.

Measurement of the Transfer Matrix

The measurement program CWCMAP was written with an option to measure the transfer matrix by measuring the pressure at specified field points with each band of the CWC driven alone in turn and write the results to data files in the form of a matrix. The output is actually to two files, with one containing the real parts and one containing the imaginary parts of the matrix. The output from the DAC monitor for the drive to band number one is always used as the phase reference. Accordingly, the drive system is always instructed to drive this band at unity amplitude and zero phase shift. The input to the power amplifier for band number one is then disconnected whenever another band is to be driven alone.

Unfortunately, there is no electronic communication between the measurement system (controlled by a PC) and the drive system (controlled by a VAX). This means that the measurement system cannot automatically set up the drive system or enable the drives. The measurement system PC must instruct the user to start the drive system with a specified set of drives. The user then instructs the VAX to operate the drive system with the specified drives. When the drives are achieved, the user indicates to the PC that the drive system is operating so that the measurement can continue.

The procedure followed in performing the transfer-matrix measurements is:

- The required parameters (e.g., frequency, locations of the field points, output filenames, etc.) are input to CWCMAP on the measurement PC and the program is instructed to start the transfer-matrix measurements.
- The PC then positions the hydrophone at the first field point and instructs the user to drive band number one alone.
- The drive system VAX is instructed to drive band number one at a constant amplitude and zero phase at the desired frequency and to set all the other drives to zero.
- The PC is then instructed to continue and measures the pressure at all the field points.
- After completing the measurements with band one driven, the PC writes the data to the files and then instructs the user to drive the next band alone.
- This process is continued until the field-point pressures have been measured and recorded for every band driven alone.

Using this procedure, the transfer matrix for the CWC at 800 Hz (with air outside the CWC) was measured for 70 field points located along the axis of the CWC (i.e., every 4 mm along the z axis from z = -13.8 to z = +13.8 cm). Even though each pressure measurement only took several seconds, setting up the drives to each band and making the 2,800 measurements took several hours. A surface plot of the amplitude of the measured transfer matrix is shown in Fig. 15. In this figure the 70 points

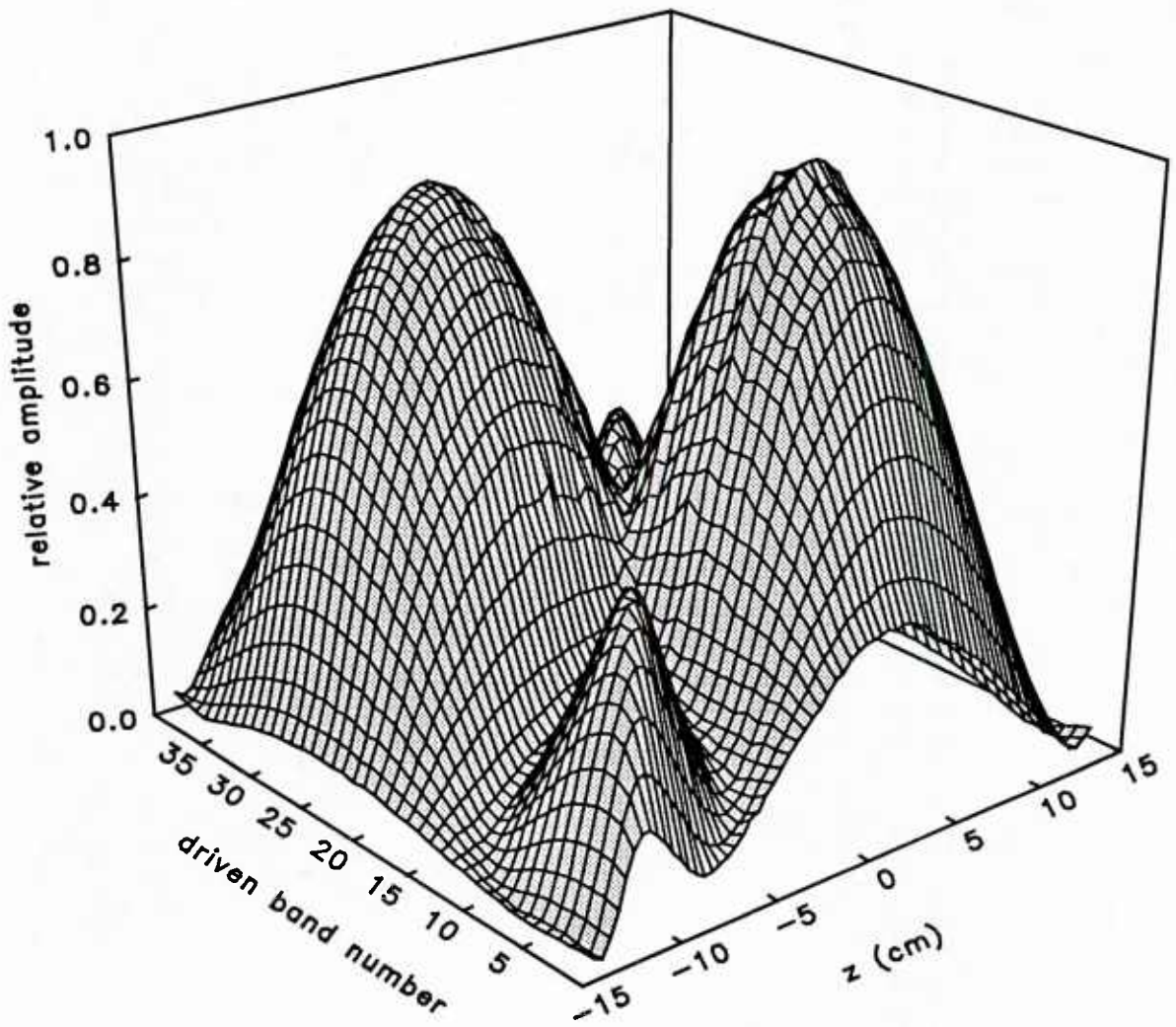

Fig. 15 — Amplitude of the measured transfer matrix at 800 Hz. The 70 points with band 1 driven are along the right-front edge.

for band number one driven are along the right-front edge running left to right from *z* equals -13.8 to +13.8 cm. The values for each successive band driven are represented by another line on the surface.

Figure 16 shows the real part of the pressure field displayed in Fig. 15. These figures show that standing-wave patterns are created in the pressure field within the CWC. The pressure drops to a relatively small value just outside of the CWC no matter which band is driven. (Note: The CWC extends from -12.6 to +12.6 cm.) This frequency (800 Hz) is between the first (half-wavelength) and second (full-wavelength) water column resonances within the CWC. The shape of the standing-wave pattern depends on which band is driven. The pressure pattern is symmetric within the CWC (i.e., the pressure fields from the upper 20 bands are mirror images of the fields from the lower 20 bands). This is reassuring since the CWC has a symmetric design. This also indicates that there is little effect on the pressure field from the B&K 8103 hydrophone housing. The housing extends for approximately 3 cm only on the left side (i.e., negative *z*) of the hydrophone's active element. If the housing was having a significant effect on the pressure field, this effect would tend to show differences when measuring pressures near the left end of the CWC (where most of the housing is

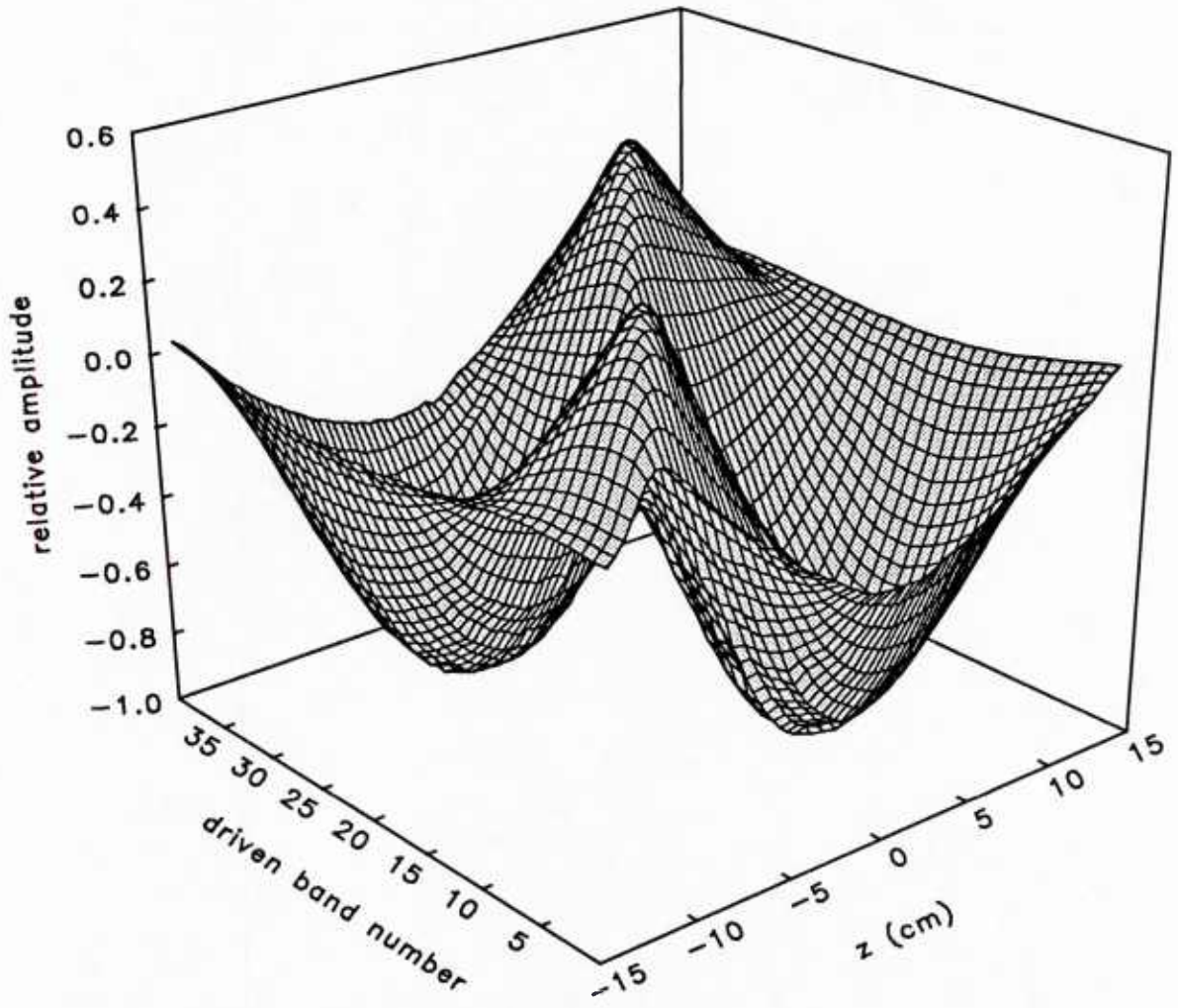

Fig. 16 — Real part of the measured transfer matrix at 800 Hz.

outside the CWC) and pressures near the right end of the CWC (where all of the housing is well within the CWC).

Pressure Fields from Calculated Drives

The measured transfer matrix was used to calculate a set of drives to produce an evanescent field within the CWC. This was accomplished with the aid of Mathcad. Mathcad [69] is a computer program that allows the user to perform complex mathematical computation and plotting. A Mathcad document was created to calculate CWC drives using the method described earlier and to calculate and plot the predicted field within the CWC if these drives were used.

The measured transfer matrix values for the 46 positions running from -9.0 to +9.0 cm were used to calculate a set of band drives that should produce a 60 m/s evanescent field over this region. The predicted field for these drives is shown in Fig. 17. In this figure the thin line indicates the extent of the window (the region in which the evanescent field was being created). Any deviation from the desired level (0 dB) is considered an error.

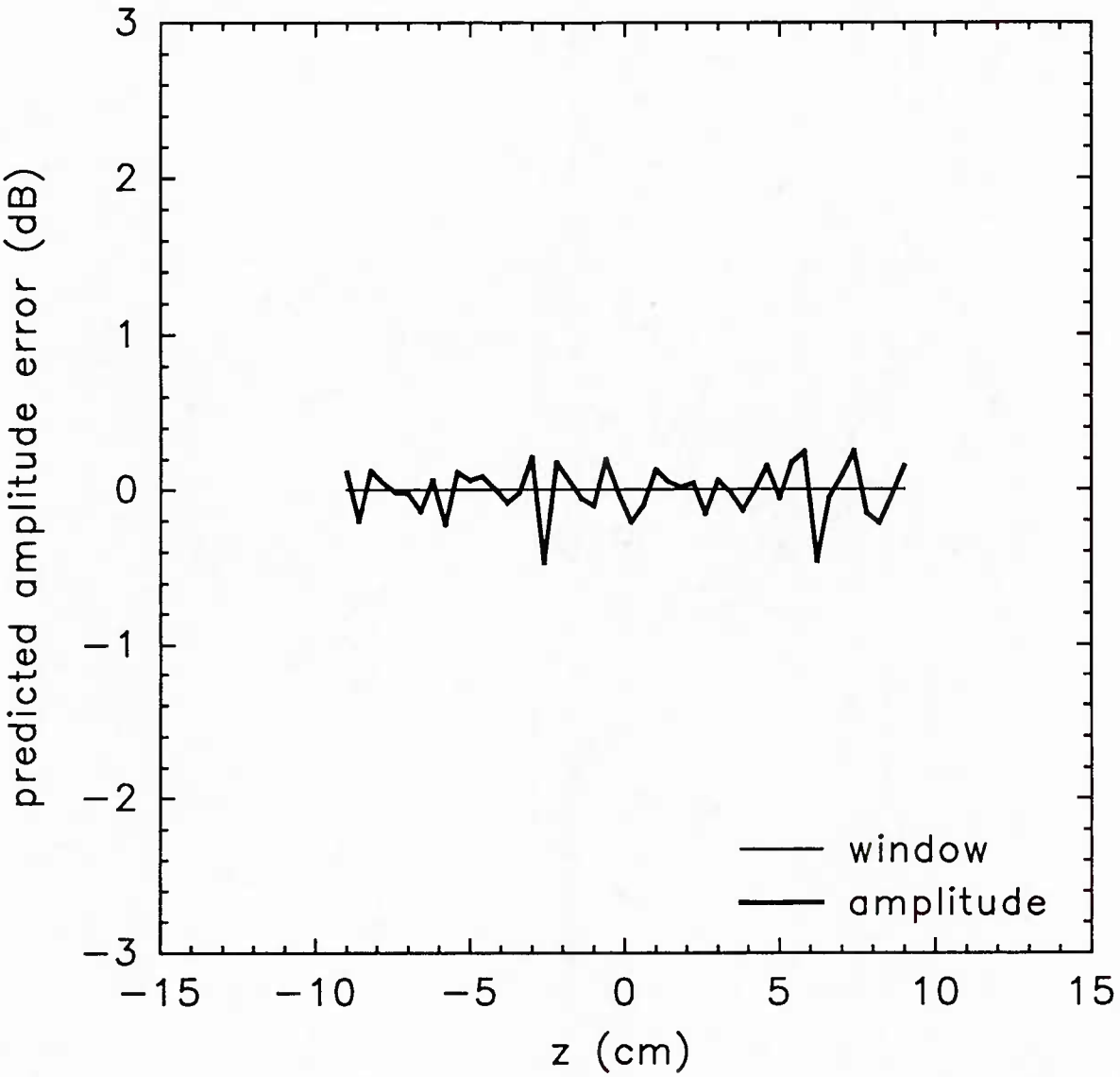

Fig. 17 — Predicted amplitude errors for a 60-m/s evanescent pressure field at 800 Hz. The measured transfer-matrix for 46 positions running from -9.0 to +9.0 cm was used.

The CWC was then driven with the calculated drives and the pressure field mapped. The results are shown in Fig. 18. Since this graph format will be used extensively to present plots of the pressure field within the CWC, it will be described in some detail here. The z axis coincides with the centerline of the CWC with the center of the CWC at $z = 0$. The upper graph plots the amplitude in relative decibels and the lower graph plots the phase in degrees. The predicted amplitude and phase are shown with the thick lines. The thin line at 0 dB again indicates the window extent. This thin line is almost completely obscured by the thick line representing the predicted pressure in this particular plot. The shaded dots indicate the actual pressures measured along the centerline of the CWC (the z axis).

The measured pressure field in Fig. 18 shows the large variations of amplitude (18 dB) and phase that are characteristic of a standing wave field rather than the desired evanescent field. An

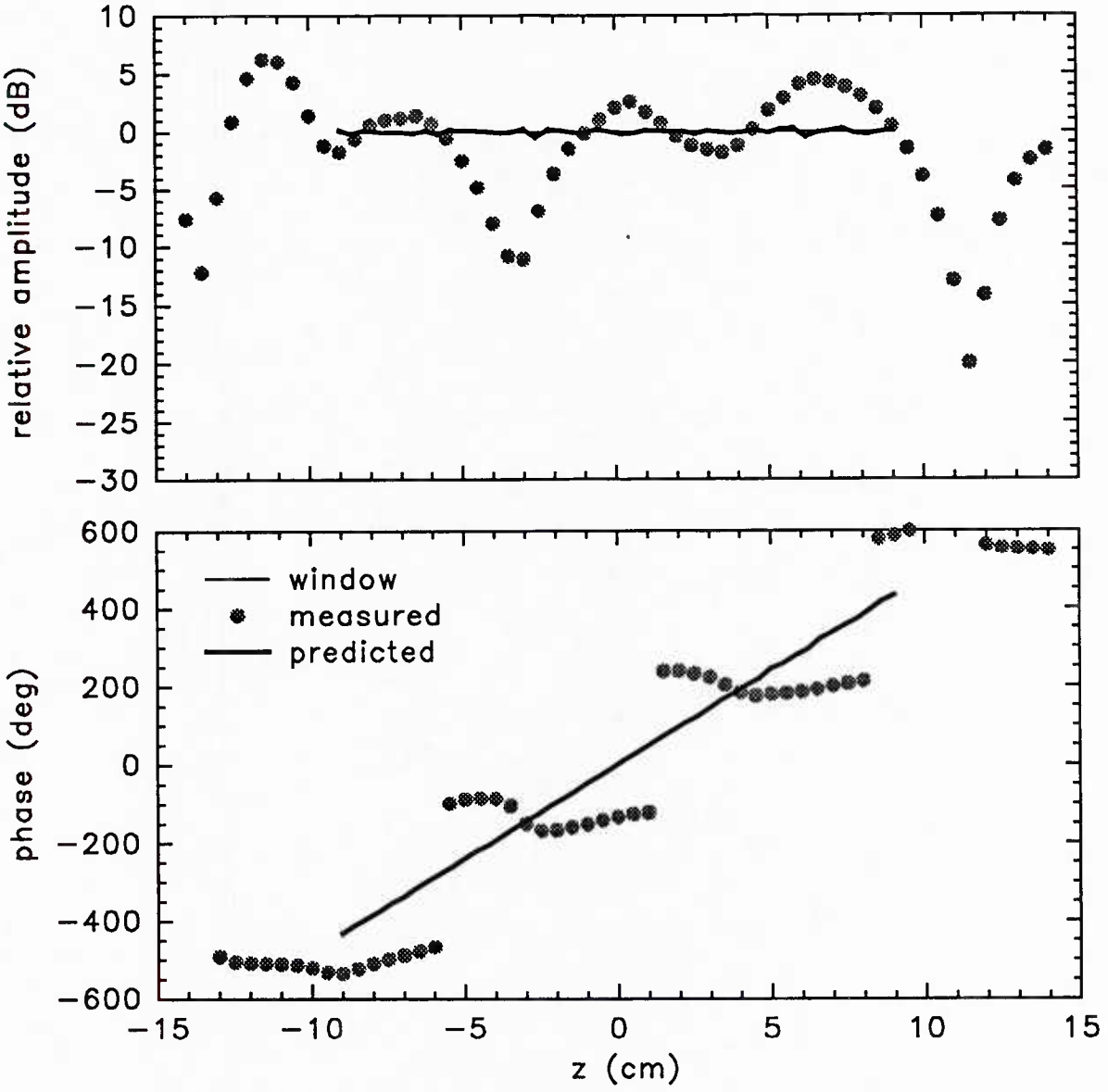

Fig. 18 — Pressures within the CWC for the 60-m/s evanescent field at 800 Hz. The measured transfer-matrix for 46 positions running from -9.0 to +9.0 cm was used.

examination of the drives used (see Fig. 19) shows large differences of amplitude and phase between adjacent bands. Although solutions of this form can produce good predicted results when inserted into a mathematical model because of the high precision available in the computations, they place severe demands on the precision of the electronic drive system. This can be demonstrated if one considers a hypothetical case where it is desired to produce unity pressure at a point in space that is equally effected by the drives to only two bands. This could be done by driving both bands with drives that would produce a pressure of +0.5 at the point if each band were driven alone. The desired pressure could also be achieved by driving the first band such that its drive alone would produce a pressure of +11.0 at the point and driving the second band such that its drive alone would produce a pressure of -10.0 at the point. Mathematically, both of these methods are equally acceptable. However, if the true pressure produced at the point is 1.0% larger in magnitude than expected when the second band is

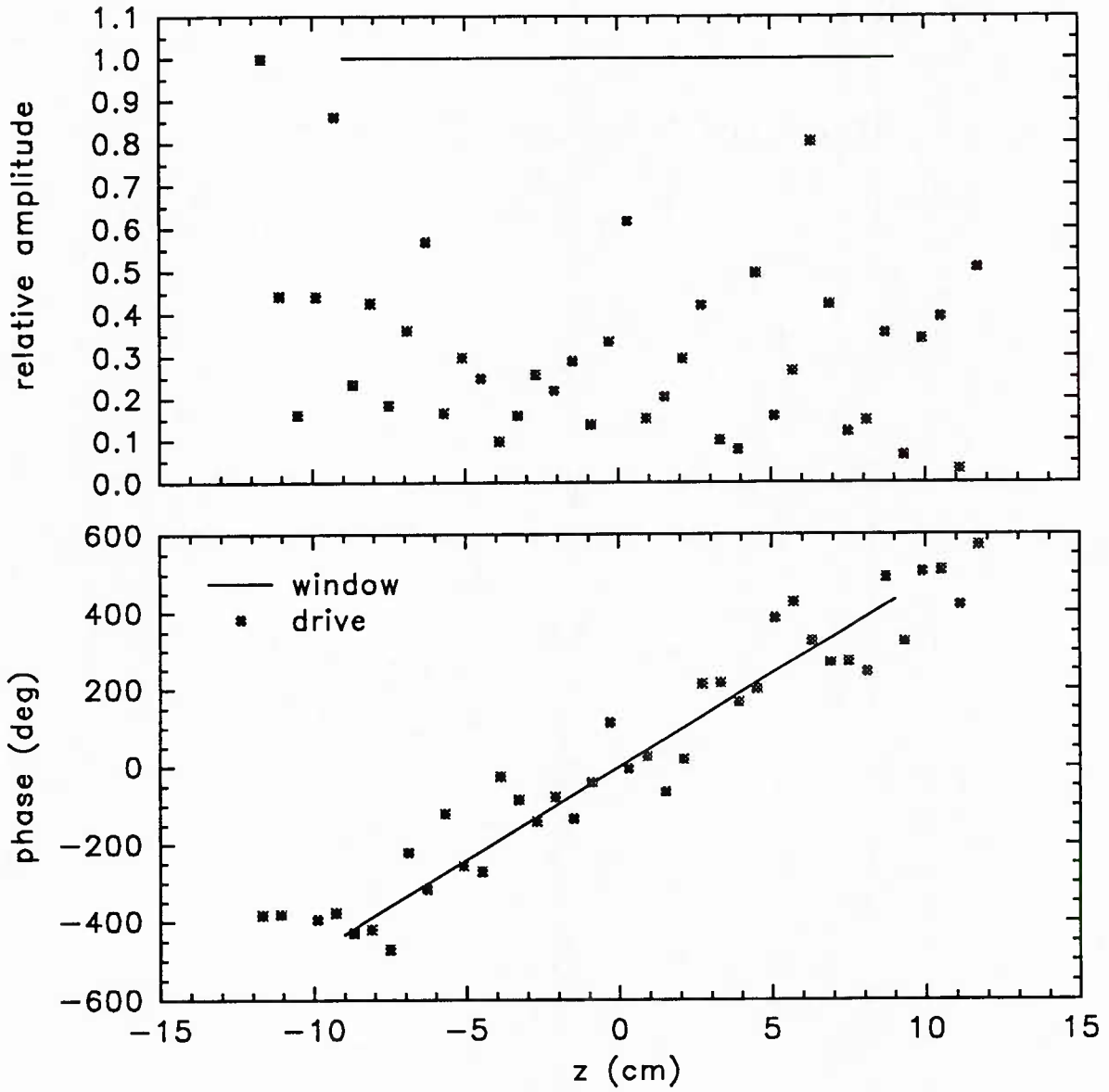

Fig. 19 — Amplitudes and phases of the band drives used to produce the pressure field shown in Fig. 18.

driven alone, the total pressure in the first case (+1.005) will have an error of only +0.5% while the total pressure in the second case (+0.9) will have an error of -10.0%. Even with no errors, the second case requires much larger drives to achieve the same pressure. For these reasons it is desirable to have drives that are as uniform as possible in amplitude and phase.

Pressure Fields from Drives Calculated with Non-Zero α

To compute more suitable drives, the technique described earlier was utilized by adding one-thousandth of the average absolute amplitude of the elements of M' to the diagonal elements. Although this shifts the solution from the ideal least-squares solution, it can significantly improve the uniformity of the drives. These drives (see Fig. 20) show more uniform amplitudes and essentially

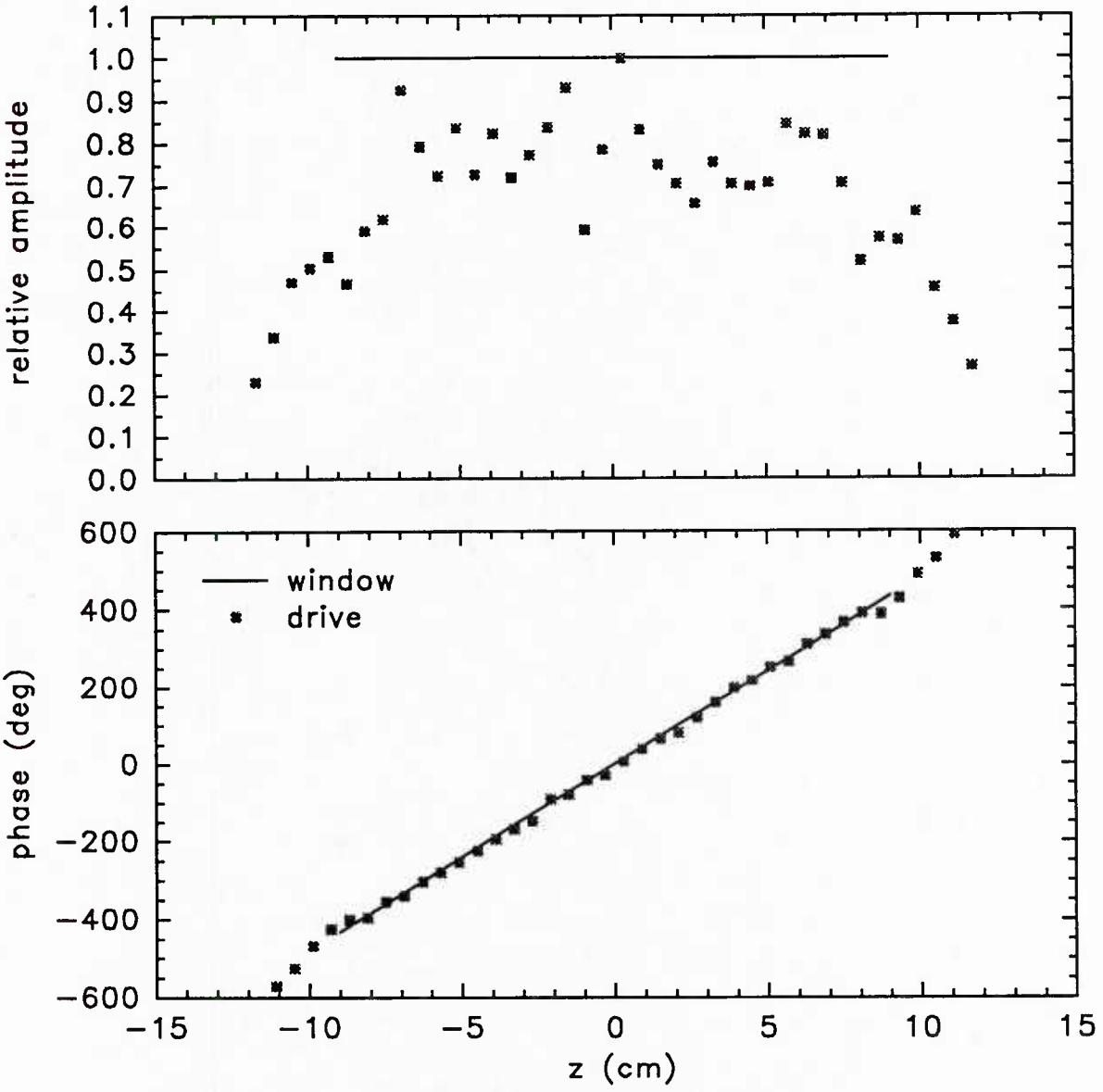

Fig. 20 — Drives calculated by setting α equal to one-thousandth the average absolute amplitude of the M' elements.

uniform phase steps between interior bands. The predicted field for these drives is shown in Fig. 21. This shows the degradation of the predicted pressure field incurred with this α. Although it is debatable just how uniform the evanescent field within an operational CWC should be, a field that is uniform to within ±1.5 dB would certainly give useful information.

The CWC was then operated with these drives and the resultant pressure field mapped. The results (see Fig. 22) show fairly good agreement with the desired and predicted evanescent field (±1.7 dB, ±12°) throughout the window region.

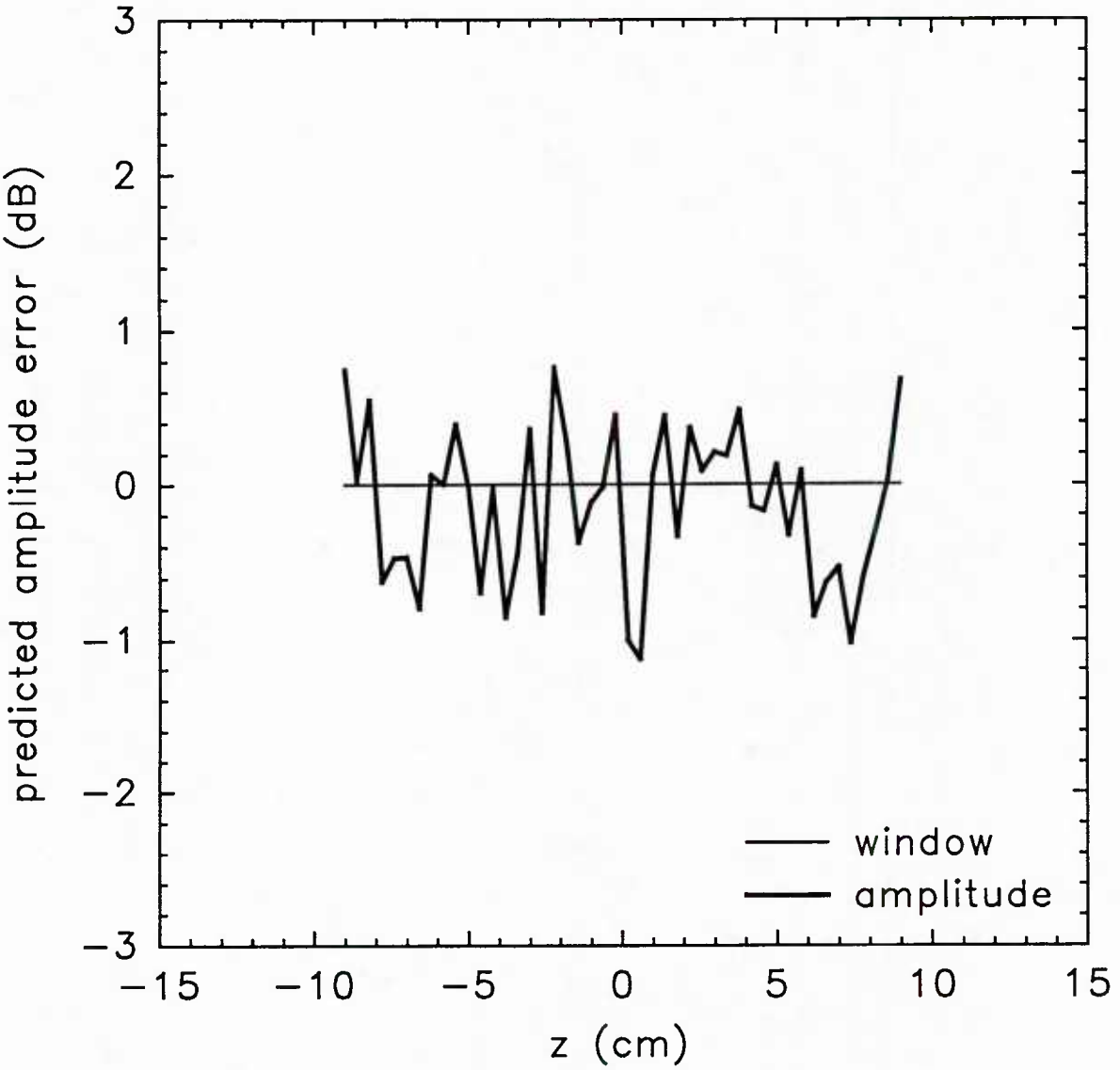

Fig. 21 — Predicted amplitude errors for the drives shown in Fig. 20.

CHIEF Model with Rigid Walls

To first examine the CWC with CHIEF, it was modeled as though it was a rigid tube totally emersed in water with only band 1 driven. This was done using the CHIEF model with all the normal surface velocities specified. The CWC was modeled with all the surface velocities set to zero except for the surfaces of band 1. The inner and outer surfaces of band 1 were given normal velocities of -1.0 and 1.0, respectively (in CHIEF, normal surface velocities are always defined with the normal pointing outward from the radiating surface). The pressure within the CWC was then computed for 31 points spaced 1.0-cm apart along the axis of the tube for a 2772 Hz drive. This frequency was chosen because it is the first resonant frequency for an open-ended rigid tube with these dimensions emersed in water. The results (see Fig. 23) showed a sharp pressure peak opposite the driven band and no signs of the water column resonance that should be there. The position of band 1 is indicated by the short line just above the *z* axis.

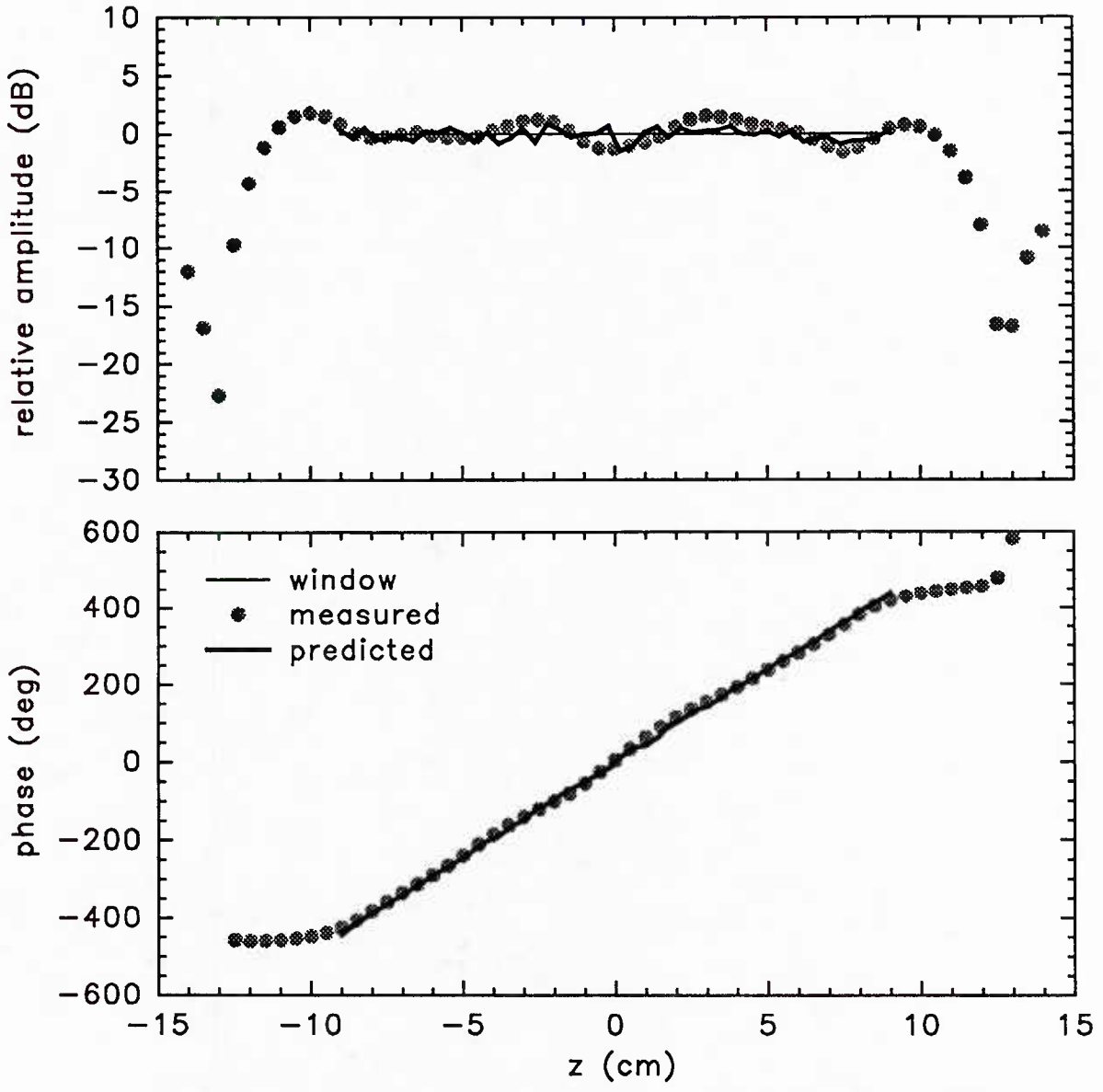

Fig. 22 — Predicted and measured pressures within the CWC using the drives shown in Fig. 20.

To determine if the integration routines used by CHIEF were giving erroneous results because of the relatively thin wall of the CWC compared to the wavelength of sound at this frequency (see Appendix C), the dimensions of the CWC in the CHIEF model were changed. The inner radius and length of the CWC were kept the same but the outer radius was changed to 2.15 cm. This increased the wall thickness from 0.075 to 6.00 mm. All the other parameters for the CHIEF model remained unchanged. The CHIEF model was then run with the new dimensions and the pressures within the CWC were computed. The results (see Fig. 24) show the eigenfunction one would expect near the first resonance in the water column. This confirmed that the problem with the CHIEF model using the correct dimensions was caused by the relatively thin wall. Unfortunately, this limitation with CHIEF is not mentioned in the CHIEF Users Manual [22].

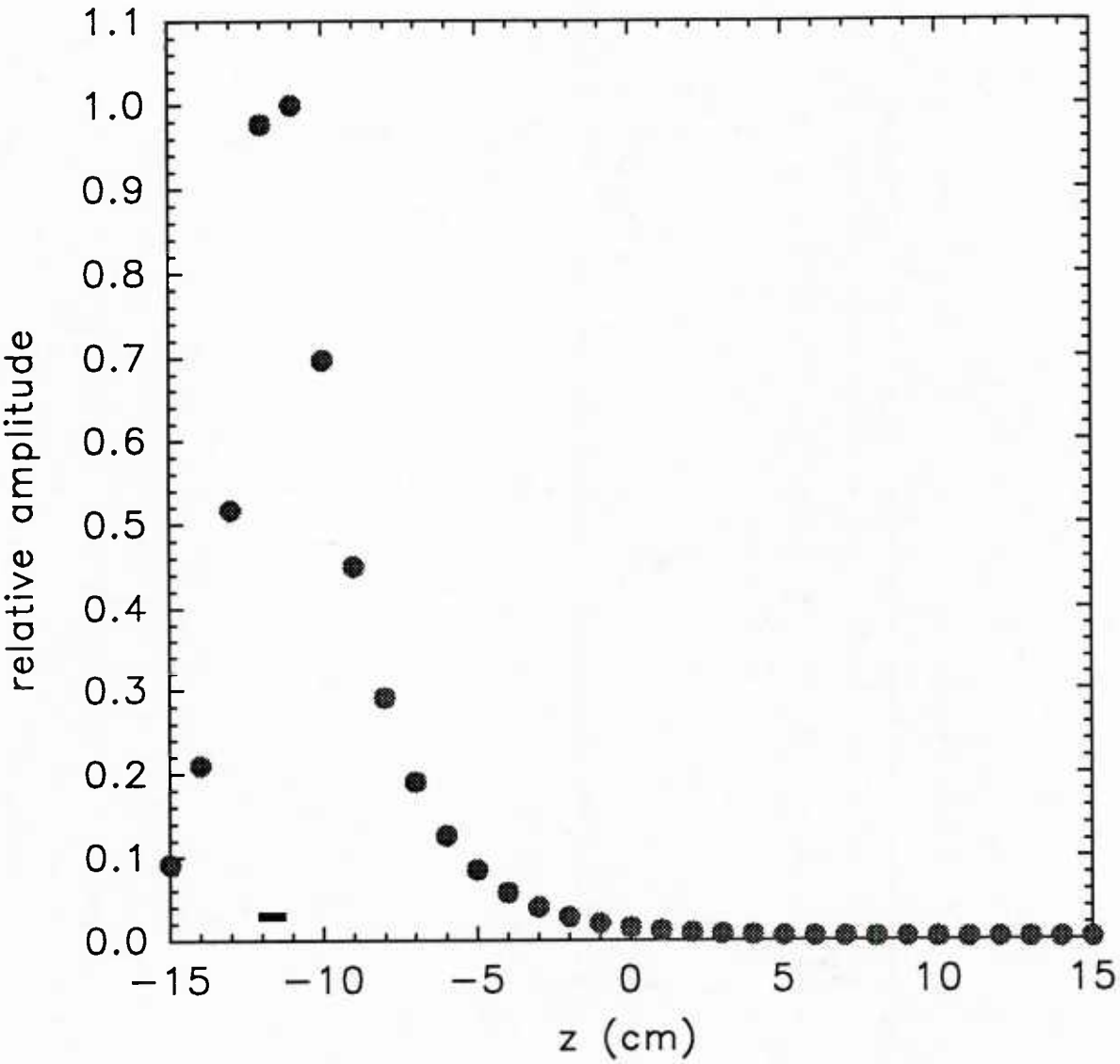

Fig. 23 — Predicted pressures along the centerline of a rigid CWC with a 0.75-mm wall. Pressures were computed using CHIEF with band 1 having unity velocity at 2772 Hz.

It is believed that the problem with CHIEF is from errors introduced when evaluating the surface integrals for points that are very near the integration surface. In particular, that errors are encountered when numerically evaluating the surface integral for a point that is on the "back" side of the integration surface. To make CHIEF usable for the 0.75-mm-wall CWC, the program was modified to perform these integrals using the same approach that CHIEF uses for its self integrals. This essentially consists of dividing the surface to be integrated into four triangular surfaces that meet at a point in the center of the original surface and changing the integration variable. A more detailed description of the modifications made to CHIEF to model the CWC are given in Appendix C. For this modification to CHIEF to work, the front and back of the thin part of the radiating body must both be divided into the same arrangement of subregions. To put it more precisely, the front and back surfaces must be divided in such a way that (in CHIEF's u,v coordinates) the center of the back subregion approaches the center of the front subregion as the thickness of the thin body approaches zero. Although this

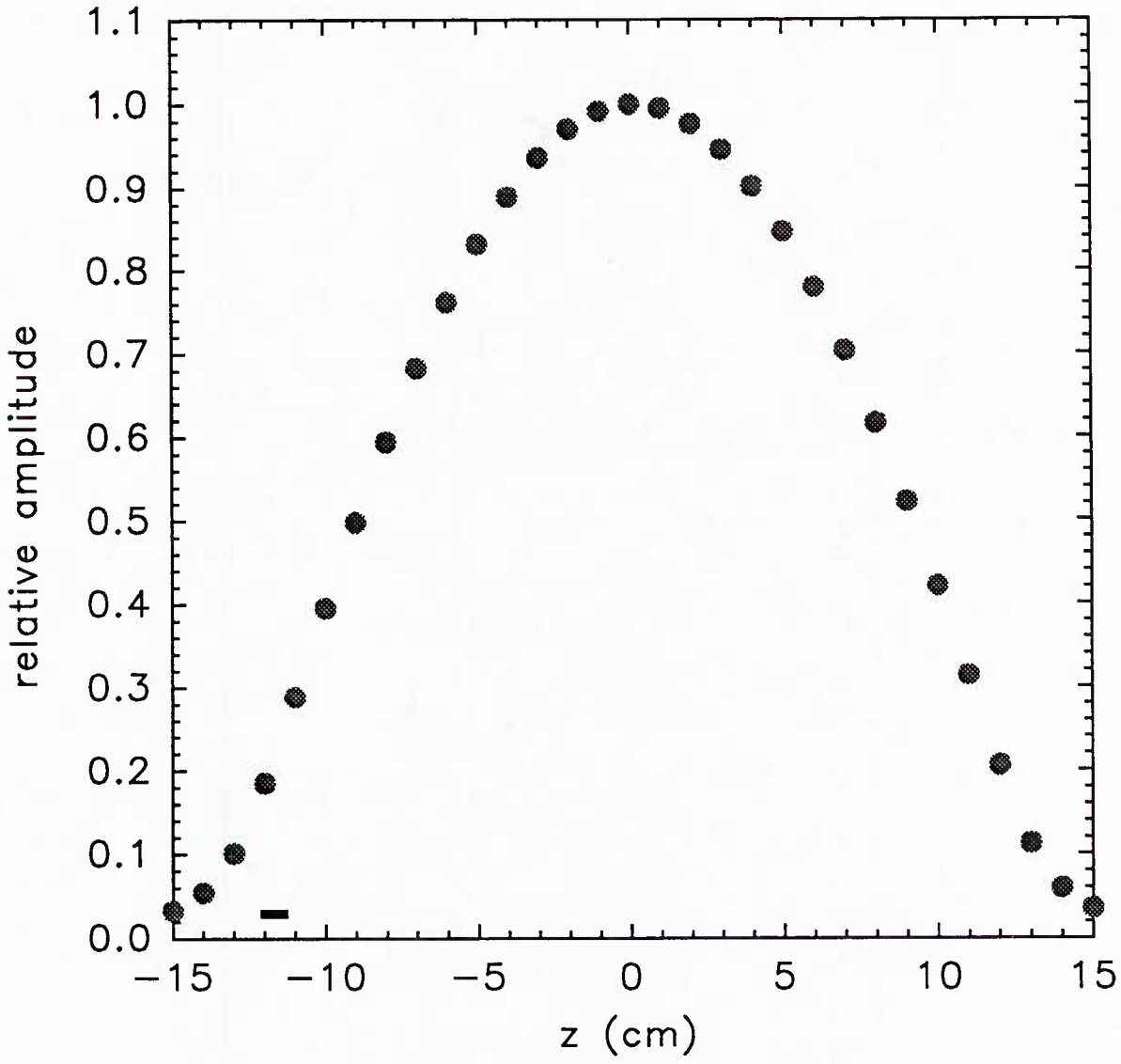

Fig. 24 — Predicted pressures along the centerline of a rigid CWC with a 6.00-mm wall. Pressures were computed using CHIEF with band 1 having unity velocity at 2772 Hz.

requirement limits the general application of the technique, the requirement is satisfied for the CWC models.

The modified CHIEF model was then run with the CWC's actual dimensions (0.75-mm wall) and the pressures within the CWC were computed. Figure 25 shows a comparison of these pressures with the previously shown pressures from the unmodified CHIEF model of a 6.00-mm-wall CWC. The results show that the modified CHIEF program gives excellent agreement with the 6.00-mm-wall model. The only differences one would expect between 0.75-mm-wall and 6.00-mm-wall rigid tubes would be slightly different end corrections and a small difference in coupling at the ends between the water outside and inside the tube. The modified CHIEF program was used for all further CHIEF models of the 0.75-mm-wall CWC.

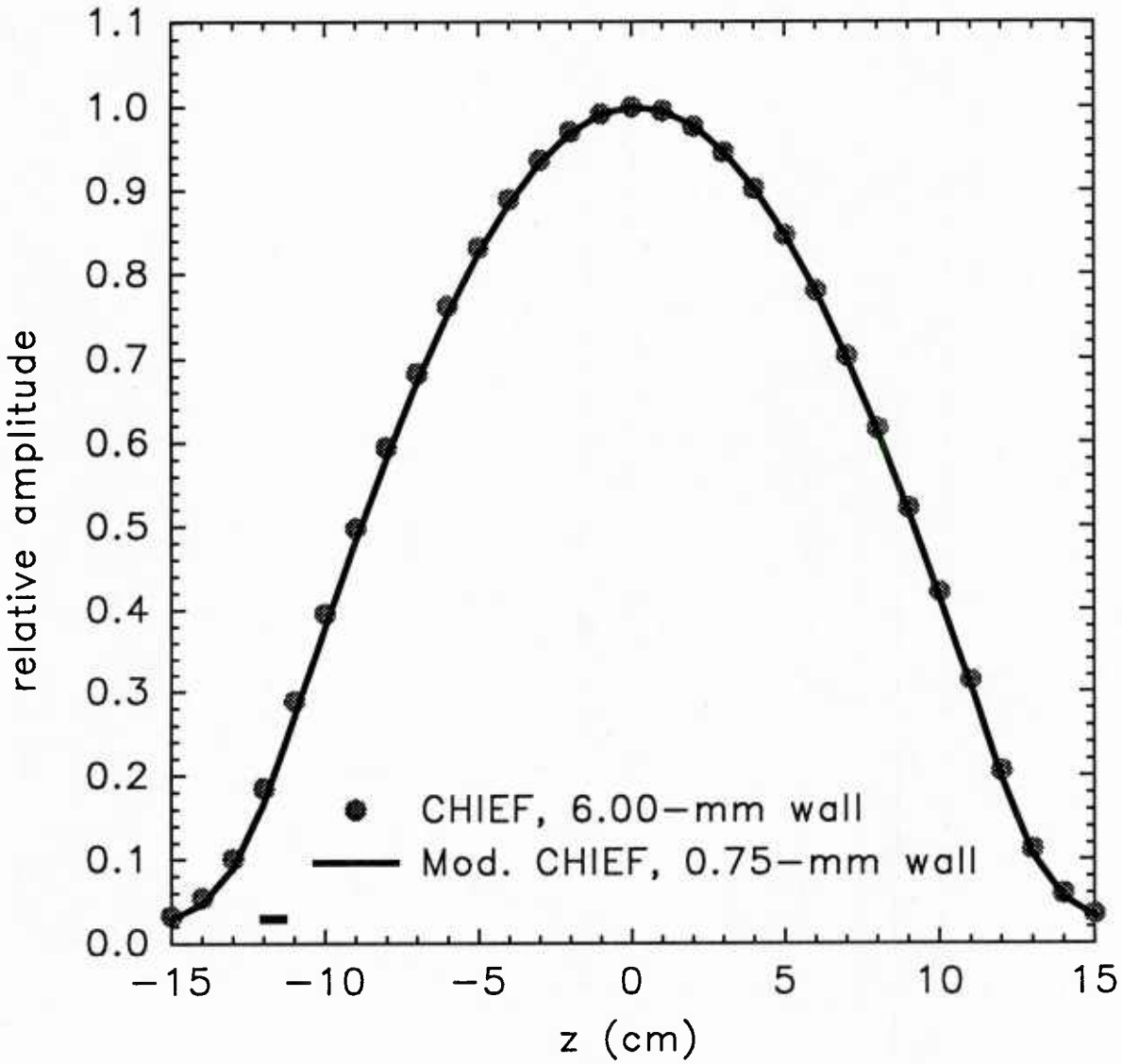

Fig. 25 — Predicted pressures at 2772 Hz from standard CHIEF with a 6.00-mm wall and CHIEF modified for the thin wall with a 0.75-mm wall.

CHIEF-I Model

The CWC was modeled using the modified-CHIEF model with the interior-wall impedance specified (CHIEF-I). This model was described earlier.

Comparison with a Single Band Driven

The CHIEF-I model was used to calculate the predicted pressure within the CWC if only band 4 were driven. The pressure within the CWC was then measured with only band 4 driven. The CWC was air-backed for this measurement. Figure 26 shows a comparison of the modeled and measured pressures along the centerline of the CWC with band 4 driven alone at 800 Hz. The position of band 4 (from z = -10.2 cm to z = -9.6 cm) is indicated by the short line just above the z axis. It can be seen that there is fairly good agreement between the CHIEF-I model and the measured pressures for

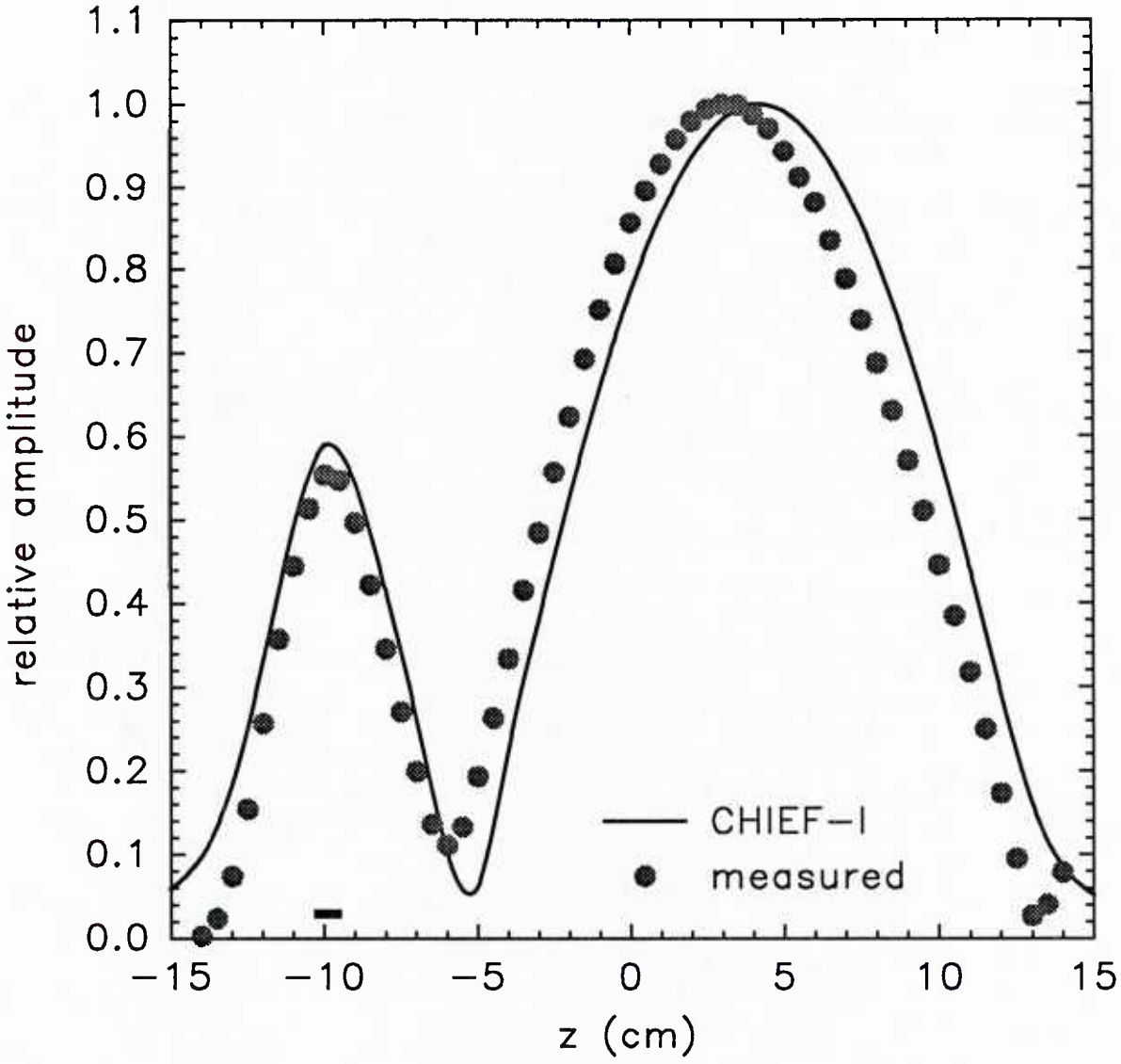

Fig. 26 — Predicted and measured pressures within the air-backed CWC with only band 4 driven at 800 Hz. The predicted pressure was calculated using the CHIEF-I model.

this simple model. The shape of the pressure field standing wave pattern is determined by how much of the energy supplied by the driven band is coupled into each of the allowed modes within the CWC. This pattern is different for each driven band because the bands are located at different positions along the CWC and therefore excite the modes in different proportions (see Figs. 15 and 16).

RING-CHIEF Model

The CWC was modeled using the RING-CHIEF model. This model considers the bands of the CWC thin-walled piezoelectric rings and includes the effects of the mutual radiation impedances. The radiation impedance matrix for this model was calculated using CHIEF.

Comparison with a Single Band Driven

The RING-CHIEF model was used to calculate the predicted pressure within the CWC if only band 4 were driven. Since the radiation impedance matrix computed by CHIEF assumes that the CWC is filled with and surrounded by water, the LEXAN mounting box was filled with castor oil. The pressure within the CWC was then measured with only band 4 driven. Figure 27 shows a comparison of the modeled and measured pressures along the centerline of the CWC with band 4 driven alone at 800 Hz. It can be seen that there is fairly good agreement between the RING-CHIEF model and the measured pressures for this model.

ATILA-CHIEF Model

In order to obtain a more complete model of the CWC, the ATILA-CHIEF model was used. Because of problems encountered in the first attempt to model the CWC with the ATILA-CHIEF combination, an effort was undertaken to measure the wall velocities of the CWC so that these could be compared with the predicted velocities from ATILA. This would allow the evaluation of the performance of the ATILA model with and without the fluid loading provided by CHIEF but without the added complication of then using CHIEF to calculate field pressures from the ATILA velocities.

Radiation-Impedance Matrix

The ATILA-CHIEF model, like the RING-CHIEF model, requires that CHIEF be used first to determine the radiation-impedance matrix for the radiating surface. The radiation impedances must be calculated by CHIEF using a surface division scheme that matches the nodal pattern for ATILA. This was accomplished using the 170 CHIEF surface divisions given in Table 2. A surface plot of the imaginary part of the radiation-impedance matrix is shown in Fig. 28. The imaginary part is about an order of magnitude larger that the real part. Only every fourth element of every fourth row is plotted to improve clarity. The surfaces run up the outside of the CWC then back down the inside (see Table 2). The diagonal elements are the self impedances. The plot shows that there is very little interaction between the inside and the outside of the CWC. It also shows that there is a relatively large amount of interaction between elements inside the CWC. This would be expected since the CWC is essentially a duct. The shapes of the curves within the CWC are similar to the pressure field within a rigid CWC for each band driven alone at this frequency.

Figure 29 shows the erroneous radiation-impedance matrix computed with the unmodified CHIEF program (i.e., without the thin-wall modifications described in Appendix C) for this same model. This figure shows large interactions between the inside and outside of each band that fade away quickly as the distance from the band increases. It should be noted that this model divides the surface into finer divisions (i.e., 3-mm-wide subregions rather than 6-mm-wide subregions) than were used in the previous CHIEF models, but the standard CHIEF program still gives errors with the 0.75-mm wall. These results again demonstrate problems that can occur using the standard CHIEF program with relatively thin vibrating bodies.

Predicted and Measured Surface Velocities

Different methods were considered for measuring the surface velocity of the CWC. An accelerometer was first considered but was rejected for the following reasons:

- The CWC wall is thin and made of fairly light material. The motion of the wall could easily be effected by the additional loading of an accelerometer.
- The accelerations anticipated were smaller than could be effectively measured with small accelerometers. Larger accelerometers might be sensitive enough, but this would

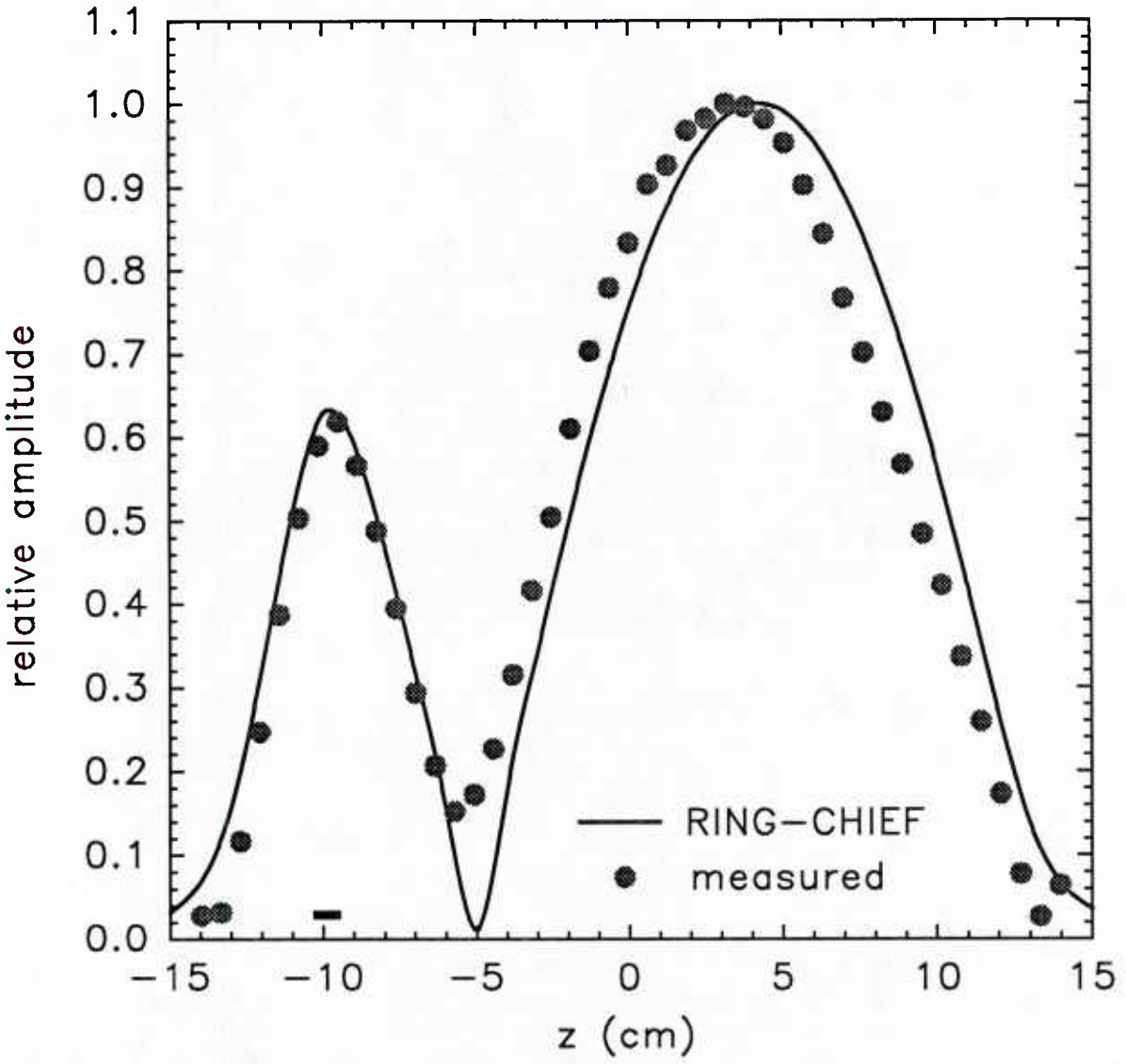

Fig. 27 — Predicted and measured pressures within the oil-backed CWC with only band 4 driven at 800 Hz. The predicted pressure was calculated using the RING-CHIEF model.

aggravate the loading problem.

- It was desirable to measure the velocity at numerous places along the surface of the CWC. This would either require numerous accelerometers or removal and reattachment of a single accelerometer.

To avoid these problems, it was decided to measure the surface velocity with the Dantec 55X Laser Doppler Vibrometer (LDV) available at USRD [70]. This system measures the surface velocity by detecting the Doppler shift of laser light reflected or scattered by the surface. For a light beam impinging on and reflected back in a direction normal to the reflecting surface, the frequency of the light is shifted upon reflection according to the Doppler equation [71]

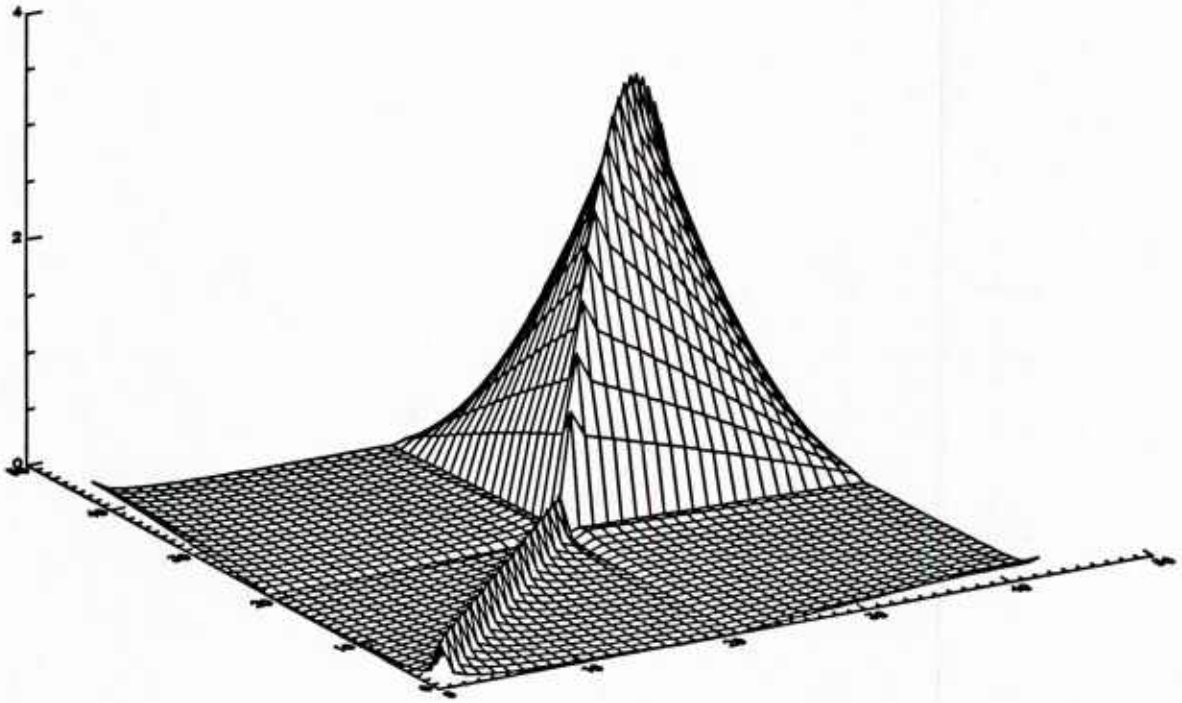

Fig. 28 — Surface plot of the imaginary part of the radiation-impedance matrix computed with CHIEF (modified to handle the thin-walled CWC) at 800 Hz.

$$\Delta f = \frac{2v}{\lambda}, \tag{67}$$

where Δf is the Doppler frequency shift, v is the normal velocity of the surface, and λ is the wavelength of the light. The LDV system used has a He-Ne laser with a wavelength of 632.8 nm. The optical system detects the Doppler shift of the reflected light by an optical heterodyne process, where the received light beam is mixed with a reference beam. Using an LDV to measure the normal surface velocity did not load the surface at all and could measure the surface velocity at numerous places along the outer wall of the CWC by just moving the LDV beam along the wall.

The LDV was placed so that it could be translated parallel to the axis of the CWC. With this arrangement, the beam could be aimed at any point along a line on the outer wall of the CWC running parallel to the axis while keeping the beam perpendicular to the CWC surface. This was required because a measurement of the normal velocity was desired and the LDV indicates the velocity component parallel to the beam. Although this arrangement limited surface velocity measurements to the outer wall of the CWC, it was felt that these measurements could verify correct operation of at least that much of the ATILA-CHIEF model. The model predicts that the outer and inner wall surfaces of each band have similar velocities, which is characteristic of thin walled tubes. The CWC was removed from the LEXAN box and suspended by its leads in air. Band 4 was driven at 1000 Hz while all the other bands were shorted to ground. Figure 30 shows the amplitude of the outer-wall surface velocity as measured by the LDV. Also shown in the figure is the surface velocity predicted by ATILA-CHIEF. For this ATILA run the CWC was modeled operating in a vacuum by setting all the radiation-impedance matrix values equal to zero. This is a reasonable approximation of the CWC

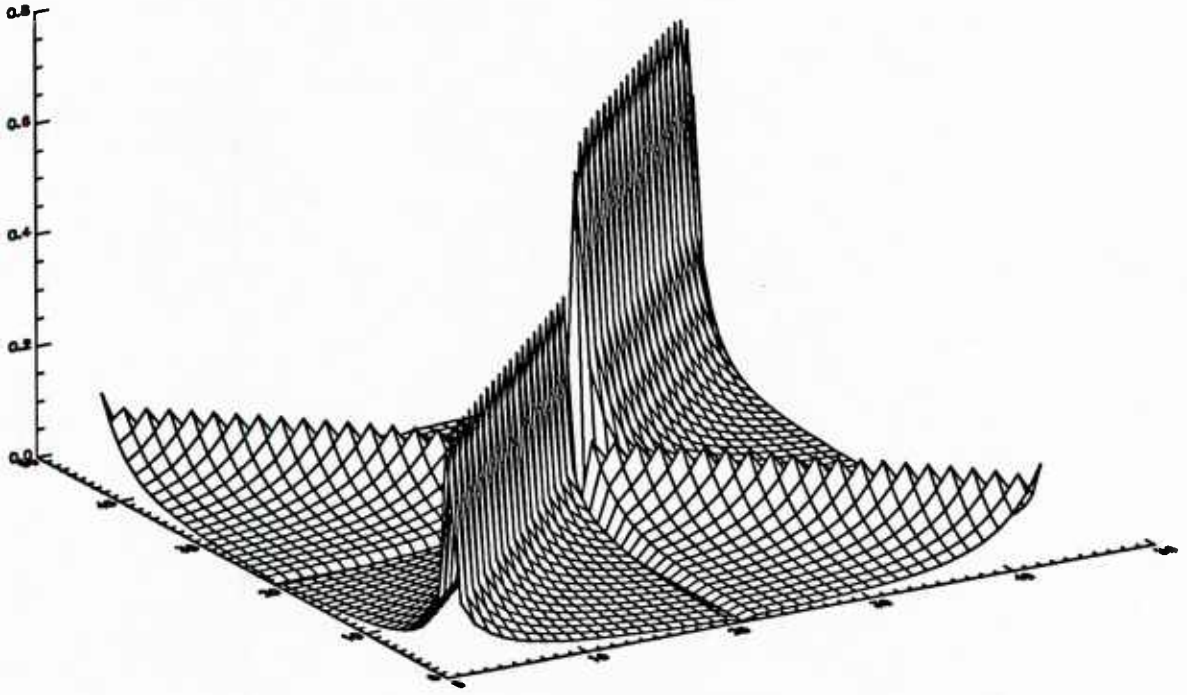

Fig. 29 — Surface plot of the imaginary part of the erroneous radiation-impedance matrix computed with CHIEF (without the thin-wall modifications) at 800 Hz.

operating in air because air provides negligible loading for the CWC. This technique had the advantage of removing CHIEF from the analysis. Although the signal-to-noise ratio of the LDV measurements is fairly low, it can be seen that the only surface velocity that stands out from the pack is on the surface of the driven band, as predicted.

The CWC was then suspended by its leads in a tank of castor oil so that it was filled and surrounded by the oil. Oil rather than water was used in the tank, because the CWC was only lightly coated with a sealer on the outside. It was felt that water would present too much danger of shorting across the outer electrode bands. Castor oil was chosen because it is a good insulator and has a density and sound speed close to water. The tank had clear glass walls. The LDV was set up as before with the LDV laser beam passing through the tank wall and castor oil to measure the CWC wall velocity. The CWC was driven at 1000 Hz, as before, and the wall velocity was measured. Figure 31 shows the measured and modeled CWC outer-wall surface velocities for this setup. The results show the velocity of the driven band riding on a wall velocity profile that coincides with the pressure field in the fluid column within the CWC, as would be expected for a tube with fairly flexible walls. The second fluid column resonance is near 1000 Hz. This also indicates why a frequency of 1000 Hz was used for the LDV measurements. As the frequency moves away from a resonance, the pressure amplitude within the CWC drops rapidly. This causes the effect of the wall velocity to drop into the background noise of the LDV velocity measurement. The LDV results indicate that the ATILA-CHIEF velocity profile prediction shows fairly good agreement with the measured velocities.

Comparison with a Single Band Driven

In order to utilize the ATILA-CHIEF model, the CWC was again operated with castor oil rather than air, inside the LEXAN mounting box. This was done because the ATILA-CHIEF model also

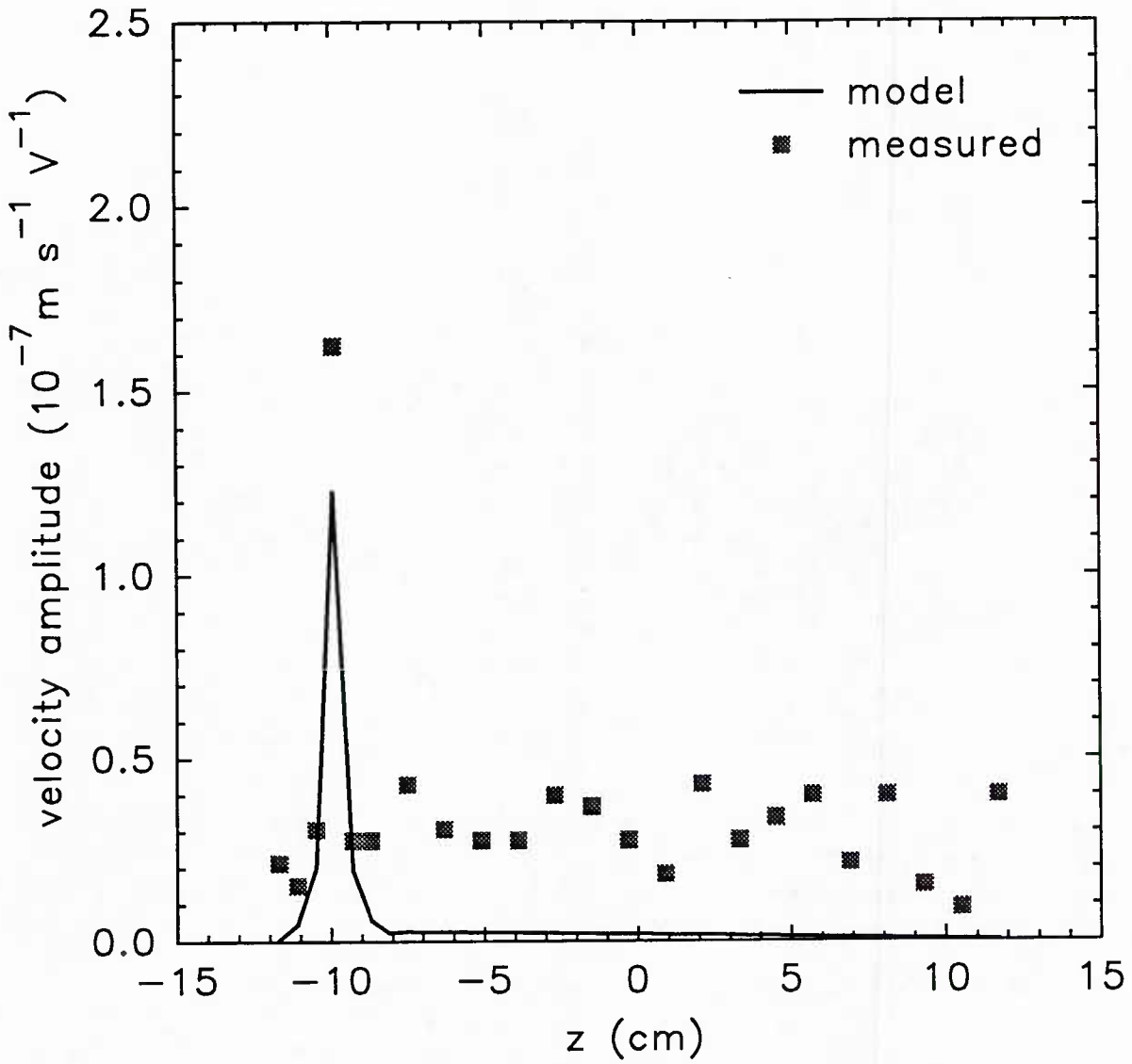

Fig. 30 — Measured and modeled CWC outer-wall surface velocities with the CWC operated in air. Band 4 was driven at 1000 Hz with all other bands shorted to ground.

assumes that the CWC is totally emersed in the liquid. The CWC was then operated with only band 4 driven at 800 Hz and the pressure along the centerline was measured. Figure 32 shows the measured pressure and the pressure predicted from the ATILA-CHIEF model. The pressure predicted from the RING-CHIEF model with band 4 driven alone is also plotted again. This graph show that there is little difference between the pressures predicted by RING-CHIEF and ATILA-CHIEF at this frequency. It also shows that there is fairly good agreement between both models and the measured pressure.

RING-CHIEF Model with Modified Radiation-Impedance Matrix

The three different models of the CWC that have been presented consist of:

- CHIEF-I — Specifies the interior-wall impedance based on a simple vacuum-backed tube equation and specifies that the outer-wall surfaces have zero velocity.

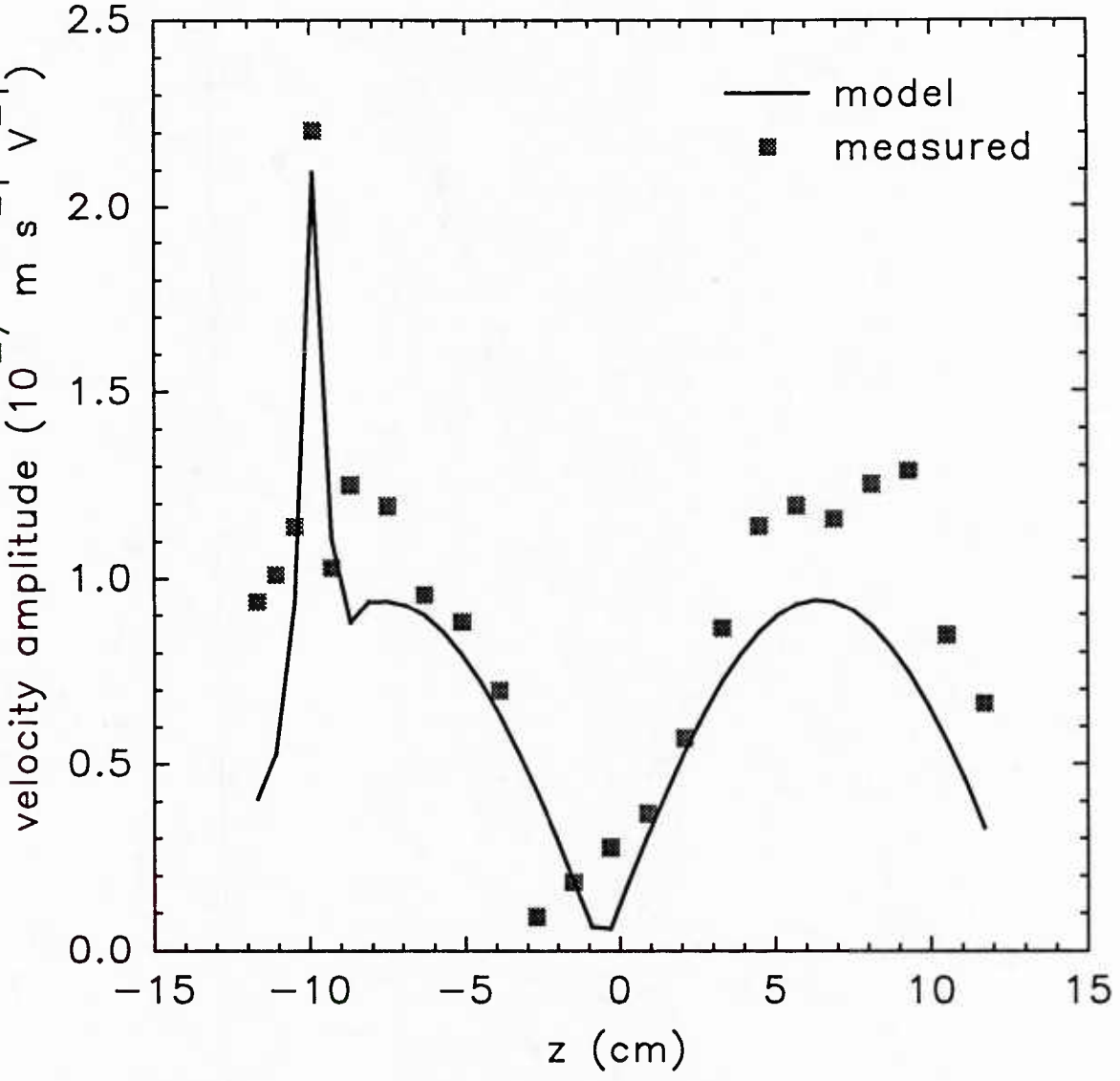

Fig. 31 — Measured and modeled CWC outer-wall surface velocities with the CWC operated in castor oil. Band 4 was driven at 1000 Hz with all other bands shorted to ground.

- RING-CHIEF — Models the CWC bands as thin-walled piezoelectric rings and includes the effects of the fluid loading with the radiation impedance matrix.
- ATILA-CHIEF — Uses a finite-element of the piezoelectric PVDF tube and includes the effects of the fluid loading with the radiation impedance matrix.

All of these models assume that the CWC is filled with and surrounded by the same fluid. However, the CHIEF-I model was used to predict the pressures within the CWC when it is air backed. The assumption was made that the surface velocities on the outside wall of the CWC had little effect on the pressure within the CWC. The RING-CHIEF model was used to confirm this assumption. Since this model includes the effects of the outer-surface velocity through the radiation-impedance matrix, it is possible to remove these effects by zeroing the appropriate elements of the matrix. The radiation-impedance was modified by zeroing all elements that related to surfaces outside of the CWC.

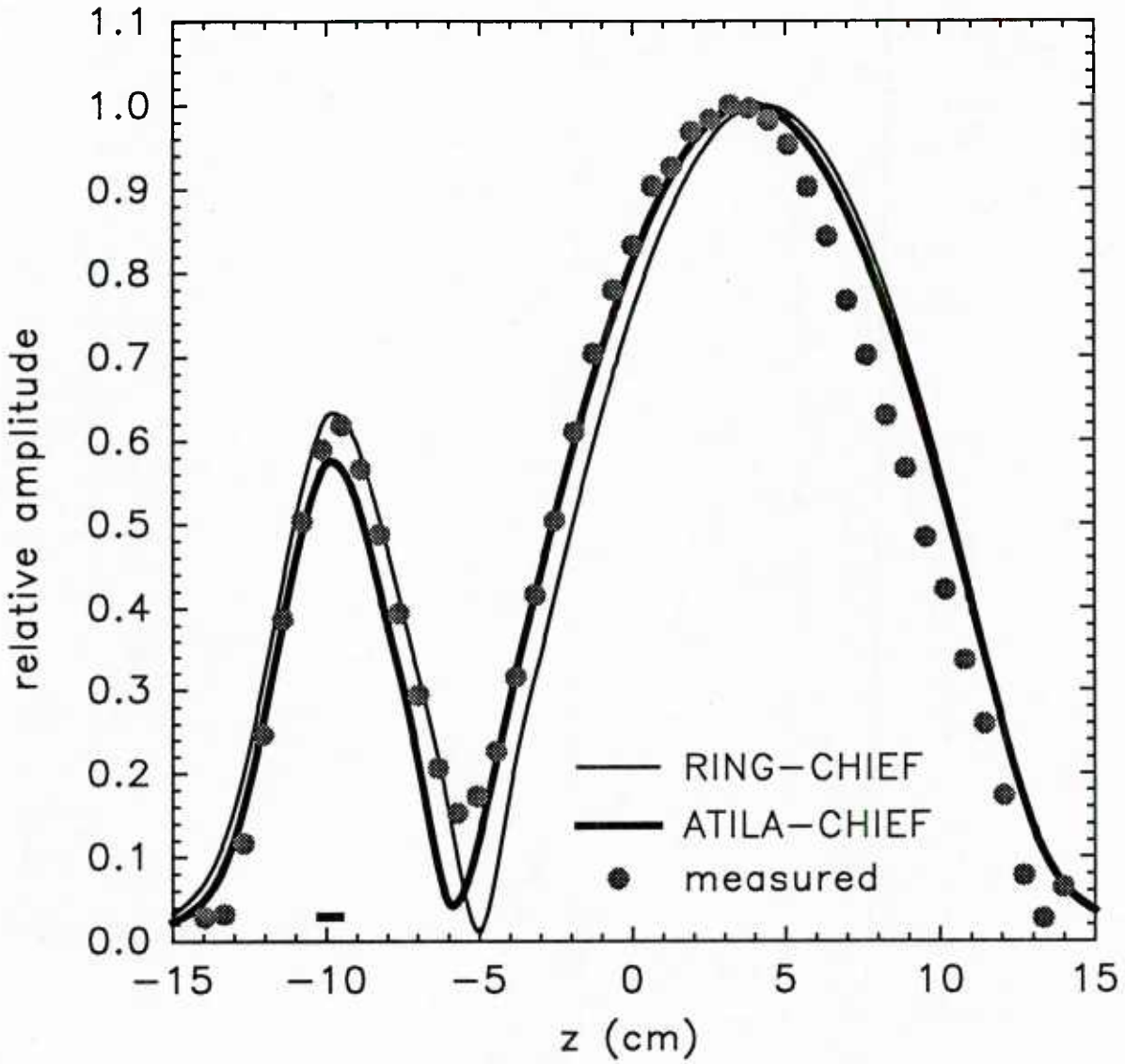

Fig. 32 — Pressures within the oil-backed CWC with only band 4 driven at 800 Hz using the RING-CHIEF model and the ATILA-CHIEF models.

Referring to Fig. 28, this would be all elements except the elements in the rear-most quadrant of the surface.

The RING-CHIEF model was used to predict the pressure within the CWC using the modified radiation-impedance matrix at 800 Hz with band 4 driven alone. Figure 33 shows a comparison of the predicted pressures using the full matrix and the partially zeroed matrix. The measured pressure within the air-backed CWC is also shown (see Fig. 26). The results do show some difference between the pressures predicted using the full matrix and the modified matrix. However, the difference is small and is comparable to the differences previously noted between the different models. Since the results with the partially zeroed radiation-impedance matrix do show somewhat better agreement with the measured pressures in the air-backed CWC, this technique is used to predict the pressures for the air-backed configuration.

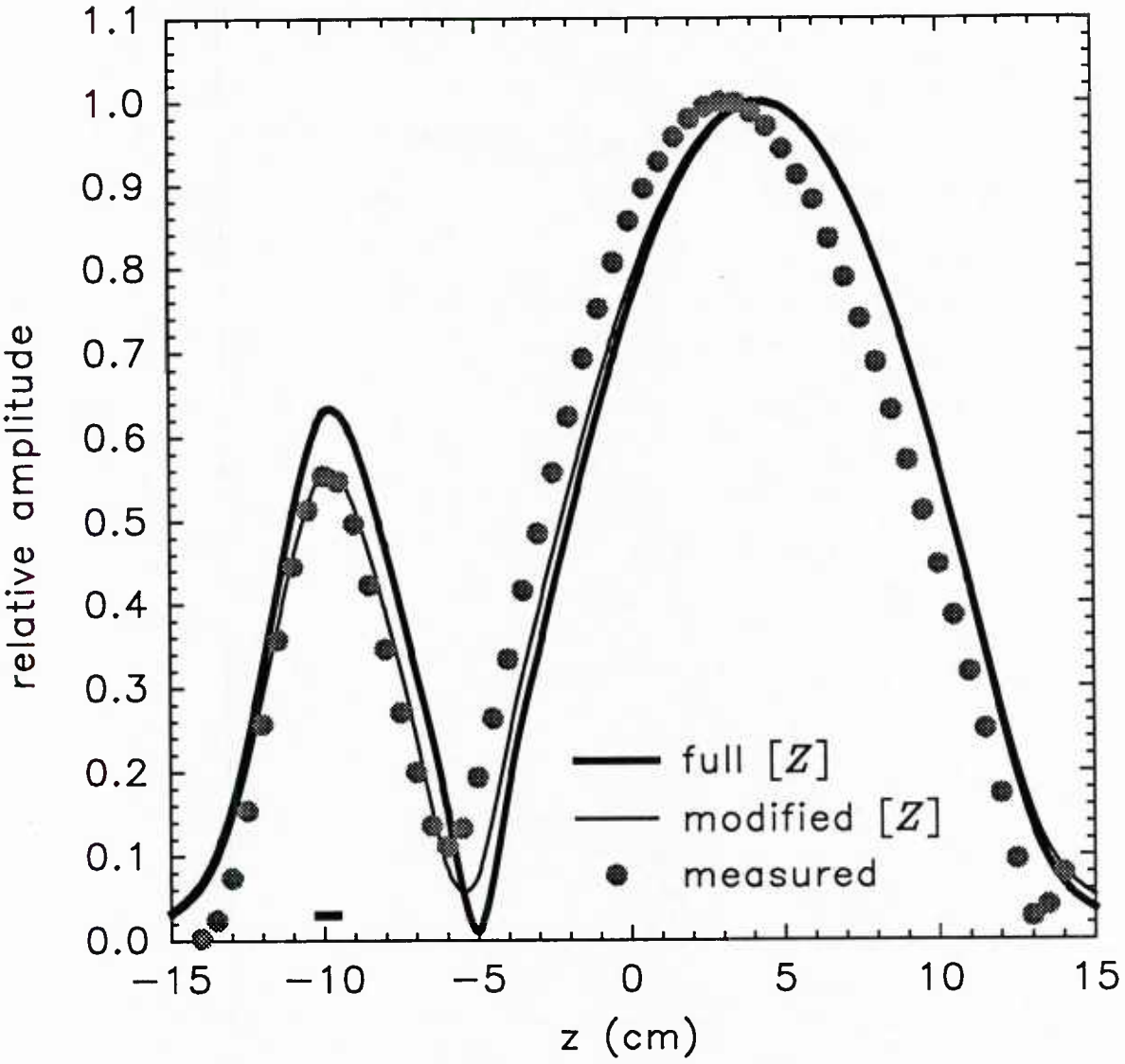

Fig. 33 — Predicted pressures within the CWC from RING-CHIEF with band 4 driven at 800 Hz. [Z] was modified by zeroing elements involving outer surfaces.

Comparison of Evanescent-Field Results

To evaluate the performance of the CWC prototype as an evanescent-wave generator, drives were computed to produce evanescent waves within the CWC. Various phase speed and window width combinations were investigated. The pressures fields resulting from drives computed using measured transfer matrices and modeled transfer matrices are now presented and compared.

800 Hz with Air Outside the CWC

To evaluate the air-backed configuration, the CWC was operated at 800 Hz with air inside the LEXAN box. Drives designed to produce a 57 m/s evanescent wave were calculated using the 42 measured transfer-matrix points running from -8.2 to +8.2 cm. The CWC was then operated with these drives and the pressure field within the CWC mapped. Figure 34 shows the predicted and

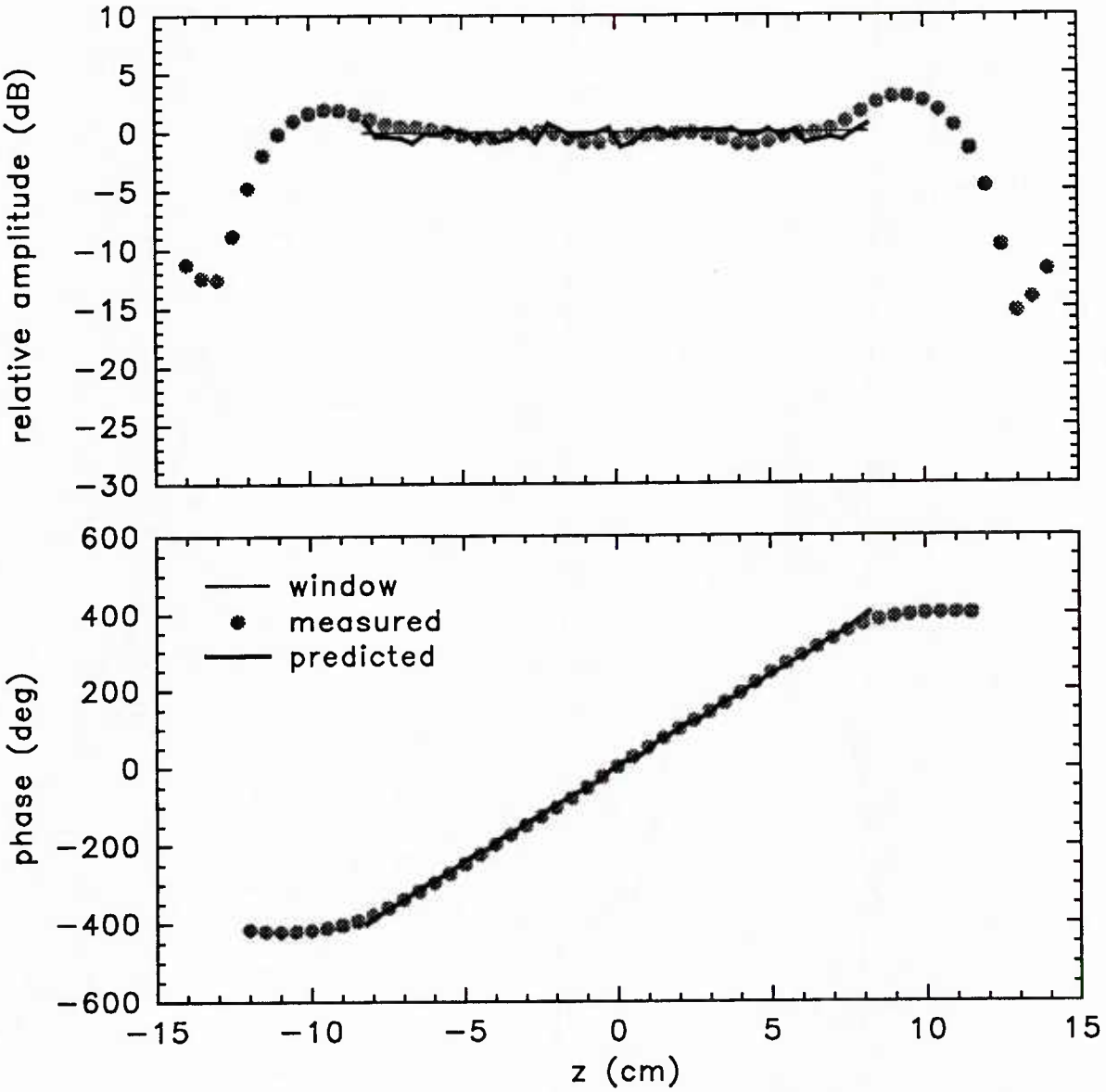

Fig. 34 — Pressures within the air-backed CWC for a 57-m/s evanescent field at 800 Hz. The measured transfer-matrix for 42 positions running from -8.2 to +8.2 cm was used.

measured pressure fields within the CWC. Drives were then computed for the same scenario using the CHIEF-I model to determine the transfer matrix rather than measured values. Figure 35 shows the measured pressure field within the CWC for this set of drives. Although the measured phase does show a trend toward the desired phase, the phase error is quite large. The amplitude error is certainly much too large for use as a calibrator. It is believed that the demands placed on the accuracy of the model are more than the model is capable of producing and that the deviations between the modeled pressures and actual pressures are causing the poor performance.

It can be observed that the measured pressure field within the CWC is not dropping in amplitude outside of the window but is remaining large until forced to drop by the low impedances encountered

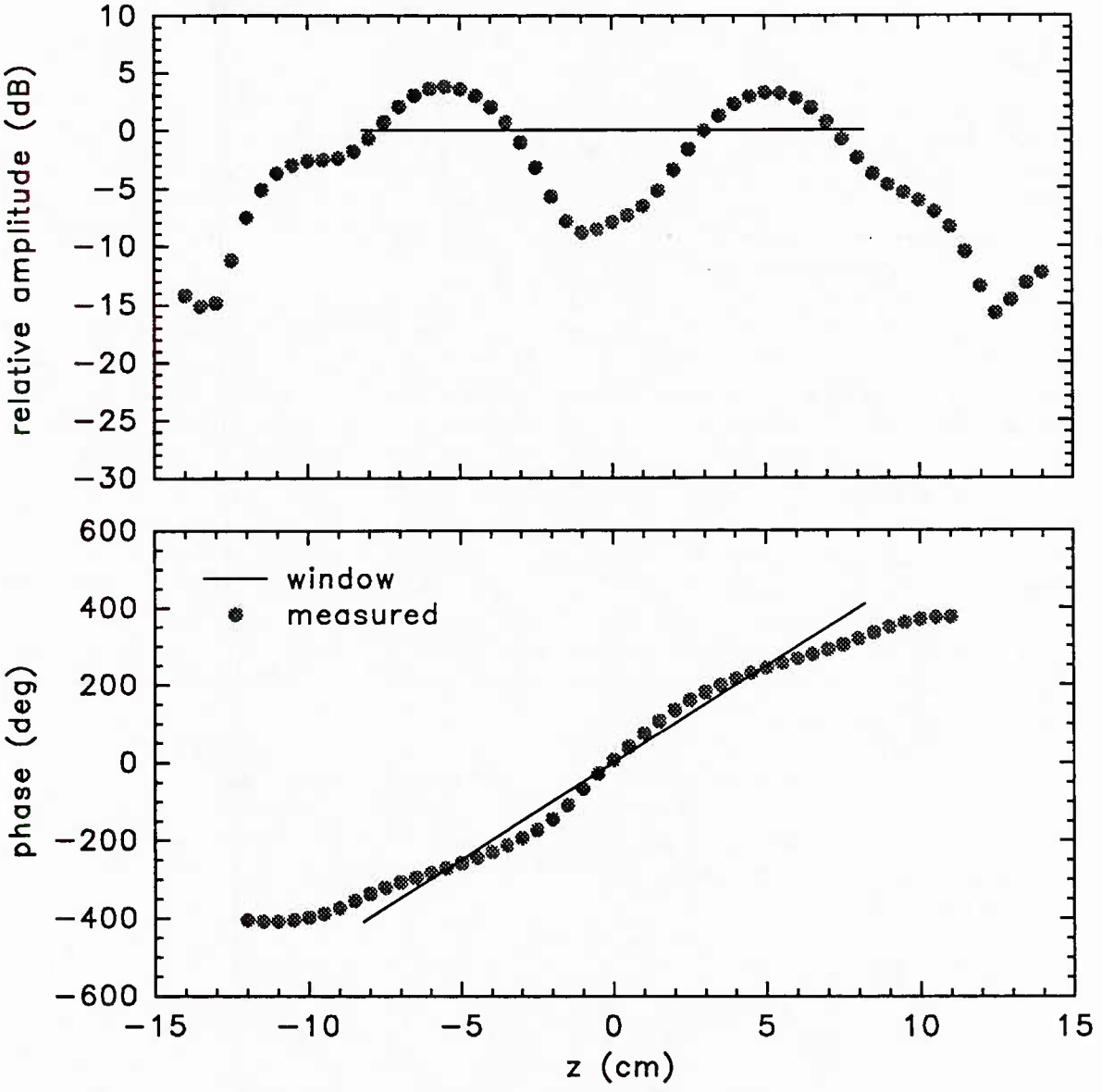

Fig. 35 — Pressures within the air-backed CWC for a 57-m/s evanescent field at 800 Hz. CHIEF-I pressure values for 42 positions running from -8.2 to +8.2 cm were used.

at (or, more precisely, just beyond) the ends of the CWC (see Figs. 34 and 35). This situation allows the large reflections from the ends of the CWC to have a major effect on the pressure field within the CWC. This places stringent demands on the accuracy of the pressures predicted by the model. An effort was undertaken to minimize these reflections and, thereby, reduce the requirements on the accuracy of the model.

It was felt that if drives could be found that reduced the pressure to a relatively small value in the regions between the window and the ends of the CWC there would be little energy left to reflect from the ends. To accomplish this, all 70 points of transfer matrix were used to compute the drives. It should be noted that previously only transfer matrix points that were inside the window were used

and no demands were placed on the solution outside of the window. The new desired pressure field ***P*** consists of pressures with amplitudes and phases matching the evanescent field inside the window and zero amplitudes for the points outside the window.

Drives were computed using this technique and the measured transfer matrix. Figure 36 shows the predicted and measured pressure fields within the CWC for this set of drives. The plot shows that the pressure is indeed dramatically reduced before the ends of the CWC. It should be noted that both the predicted and measured pressures show a decrease in uniformity inside the window. This is not surprising since the new technique is a tradeoff in that the 40 complex drives to the bands now have to also try to drive the field to zero outside of the window.

Drives were then computed specifying the same desired pressure field but using the CHIEF-I model to determine the transfer matrix rather than measured values. Figure 37 shows the measured pressure field within the CWC for this set of drives. It can be seen that the pressures field outside the window is driven down considerably, and that there is a dramatic improvement in the uniformity of the pressure field inside the window. This indicates that reducing the pressure outside the window does make it easier to achieve the desired pressures inside the window using the model.

Another advantage of reducing the pressure outside the window becomes apparent when one considers the use of a full scale CWC in actual operation as a calibrator. If a device was placed in the CWC and an evanescent field created in a window within the CWC, it would be more desirable to have little or no pressure field outside of the window to effect other portions of the device. For these reasons it was decided to use the technique of reducing the pressure outside the window for the further evaluation of the CWC.

Drives were then computed specifying the same desired pressure field but using the RING-CHIEF model to determine the transfer matrix. Since this is an air-backed case, the partially-zeroed radiation-impedance matrix was used. Figure 38 shows the measured pressure field within the CWC for this set of drives. The resultant pressure field is very similar to that obtained using CHIEF-I. This is not surprising since the predicted pressure field from driving a single band was also very similar for both of these models.

800 Hz with Oil Outside the CWC

In order to study evanescent fields within the liquid-backed CWC, it was again operated with castor oil inside the LEXAN box. The transfer matrix was then measured for the oil-backed CWC at 800 Hz at the 70 field points used previously for the air-backed case. The measured transfer matrix was used to calculate a set of drives to produce a 55-m/s evanescent wave in a window running from -8.5 to +8.5 cm. Figure 39 shows the predicted and measured pressure fields within the CWC for this set of drives. These results are very similar to the air-backed case shown in Fig. 36. This is not surprising since the previous analysis has shown that the characteristics of the CWC do not change very much at 800 Hz whether the CWC is air or oil backed and the phase speeds and window widths specified for these two cases are almost the same. Any differences in characteristics of the CWC are automatically taken into account by the measured transfer matrix.

Drives were then computed specifying the same desired pressure field but using the CHIEF-I model to determine the transfer matrix rather than measured values. Figure 40 shows the measured pressure field within the CWC for this set of drives. The measured pressure field is similar to Fig. 37 but shows slightly less uniformity inside the window.

Drives were then computed specifying the same desired pressure field but using the ATILA-CHIEF model to determine the transfer matrix, and predicted pressure fields were computed. Figure

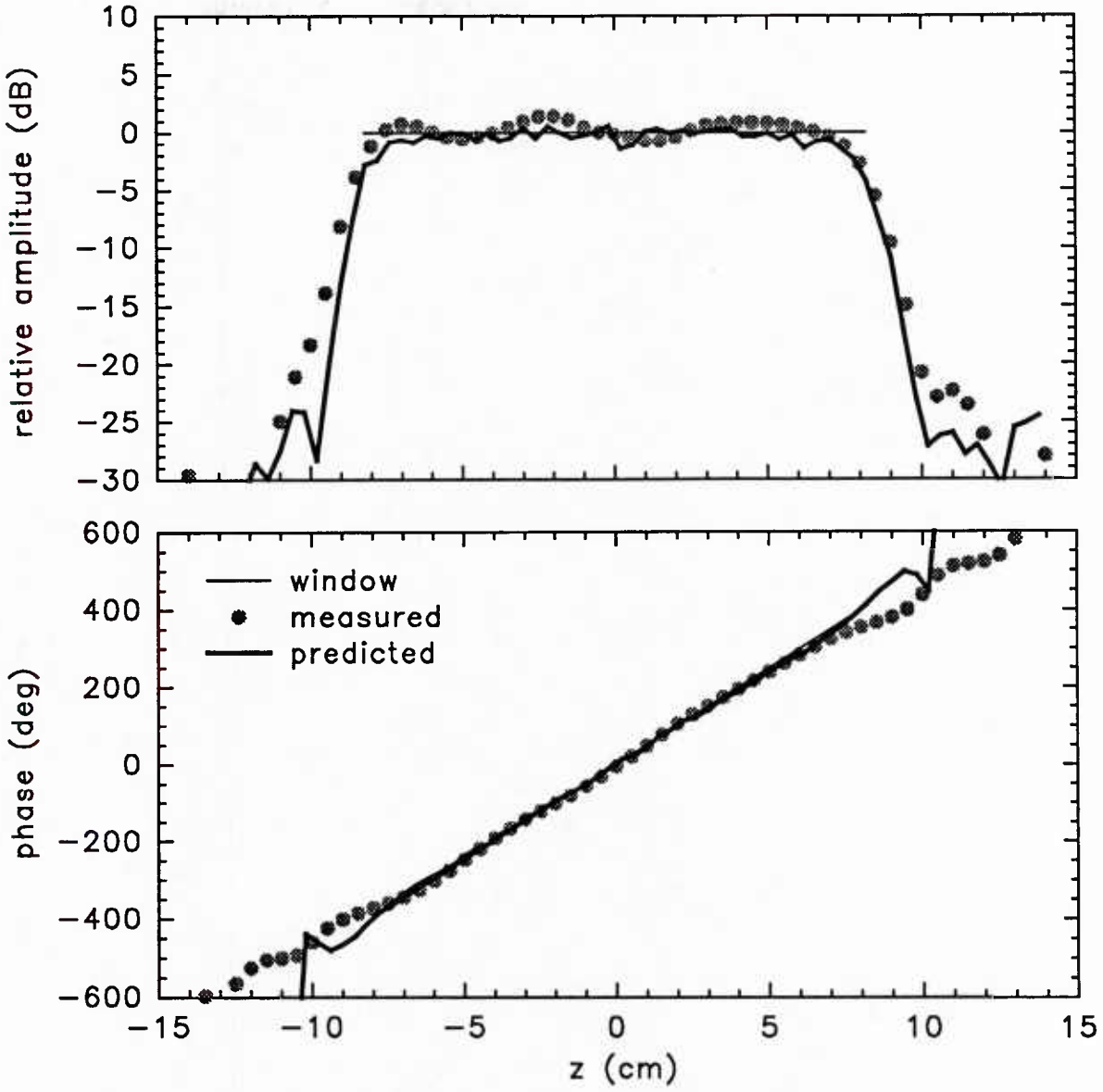

Fig. 36 — Pressures within the air-backed CWC for a 57-m/s evanescent field at 800 Hz in a window running from -8.2 to +8.2 cm using the measured transfer matrix.

41 shows the predicted and measured pressure fields within the CWC for this set of drives. These results are similar to those obtained with the CHIEF-I model. Neither model performed as well as when using the measured transfer matrix.

The measured transfer matrix was then used to calculate a set of drives to produce a 92-m/s evanescent wave in the same window (from -8.5 to +8.5 cm). Figure 42 shows the predicted and measured pressure fields within the CWC for this set of drives. The uniformity inside the window is not quite as good as it was for the 55-m/s case. It is also apparent that the pressure field was not driven down as low outside the window.

Drives were then computed specifying the same desired pressure field but using the CHIEF-I

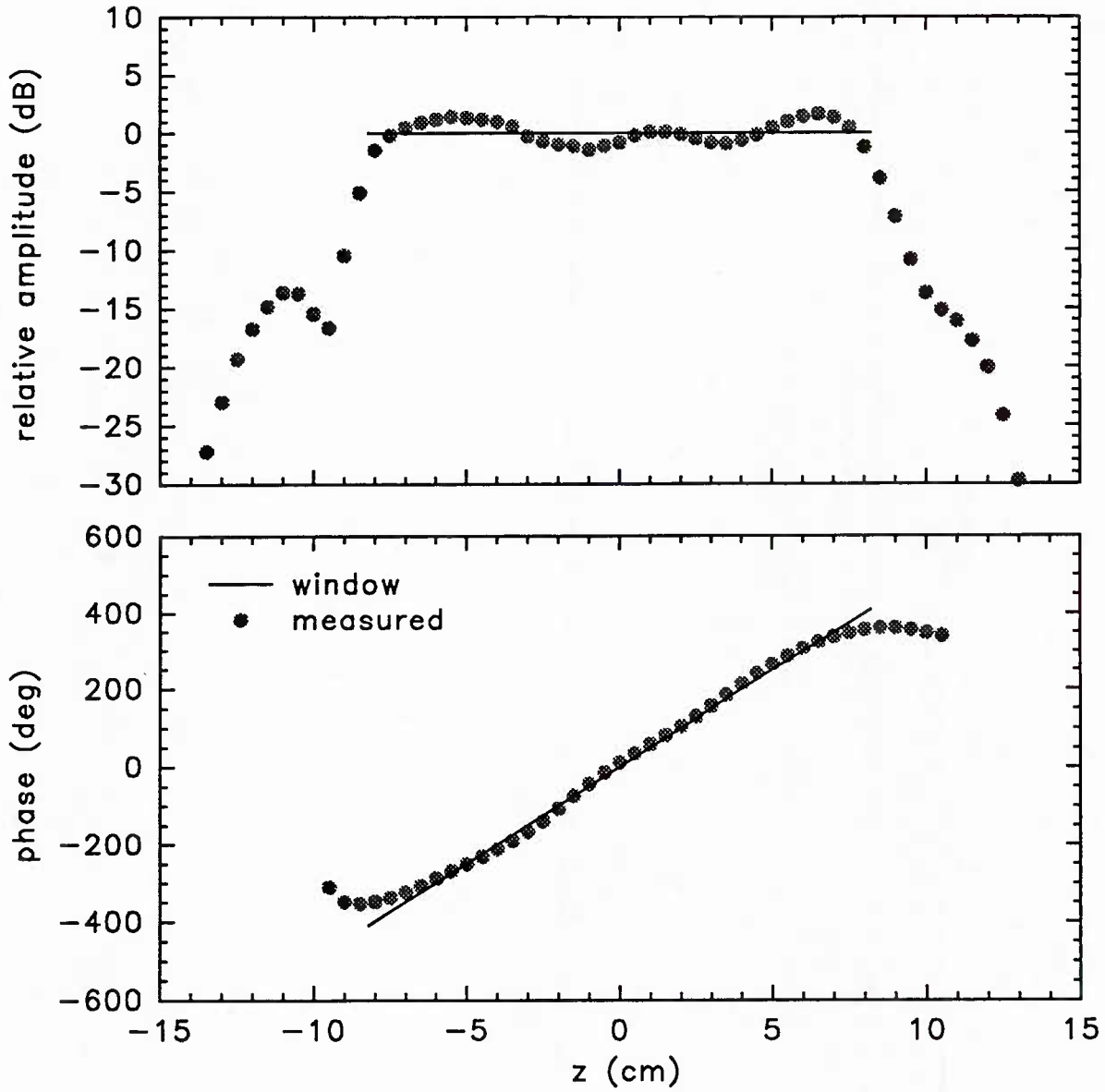

Fig. 37 — Pressures within the air-backed CWC for a 57-m/s evanescent pressure field at 800 Hz in a window running from -8.2 to +8.2 cm using CHIEF-I.

model to determine the transfer matrix rather than measured values. These results are shown in Fig. 43. The field shows much more variation inside the window than the results for the measured transfer matrix.

Finally, drives were computed specifying the same desired pressure field but using the ATILA-CHIEF model to determine the transfer matrix. These results, shown in Fig. 44, indicate a significant improvement of the uniformity of the field inside the window compared with the CHIEF-I model.

In the evanescent-field results presented thus far, the window sizes and evanescent phase speeds were chosen to make Eq. (1) equal zero at the effective acoustic wavenumber within the CWC. This minimizes contamination of the evanescent field from acoustic energy propagating axially within the

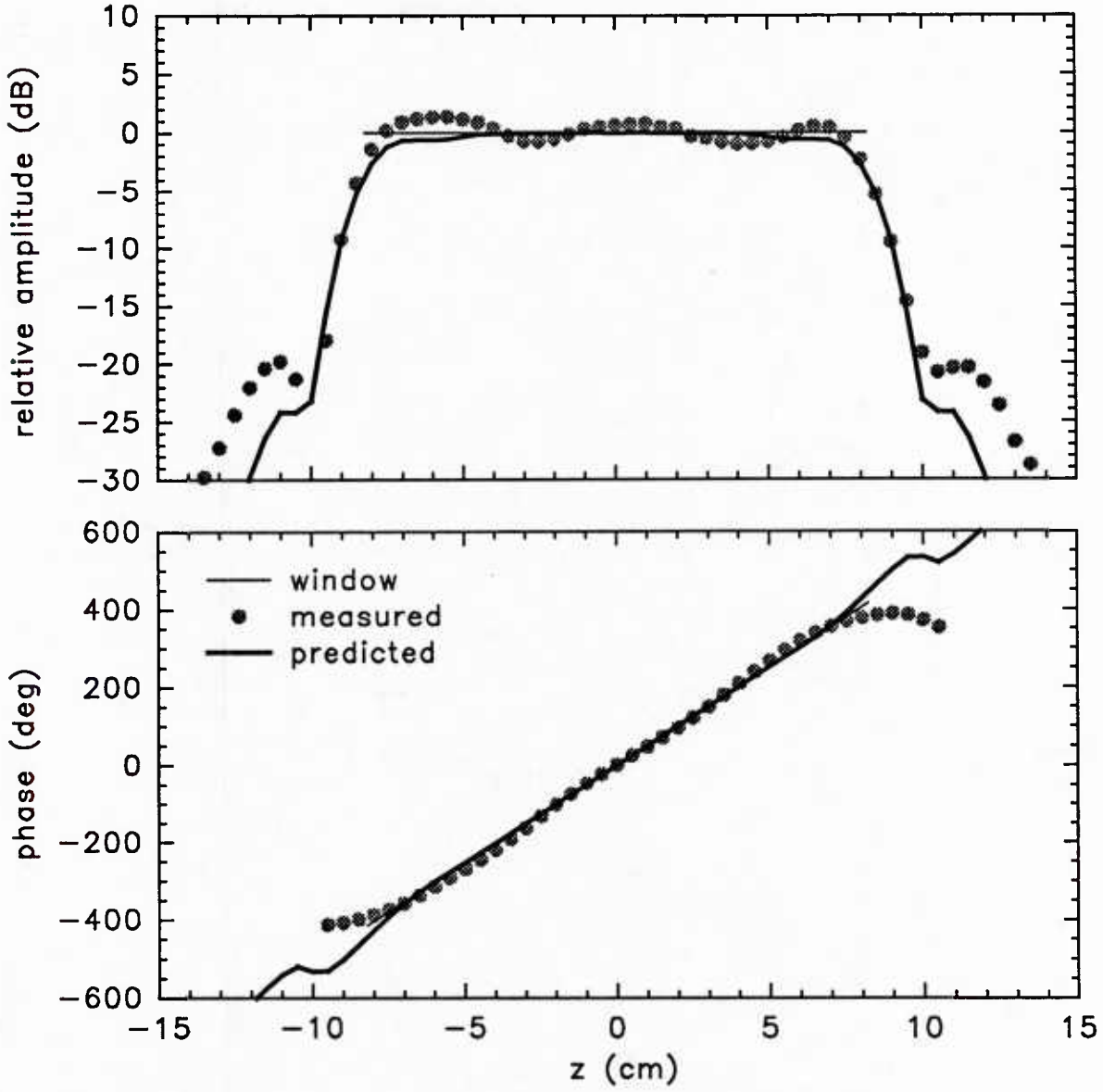

Fig. 38 — Pressures within the air-backed CWC for a 57-m/s evanescent pressure field at 800 Hz in a window running from -8.2 to +8.2 cm using RING-CHIEF.

CWC. The window half-width w was determined from

$$w_n = \frac{n\, c_a c_e}{2f(c_a - c_e)}, \qquad n = 1, 2, 3, \ldots \tag{68}$$

where c_a is the propagation speed for sound of this frequency freely propagating down the inside of the CWC, c_e is the desired evanescent phase speed, and f is the frequency. Figure 45 shows a plot of Eq. (1) for the 92-m/s case described in Figs. 42 through 44. A value of one was chosen for n to find the narrowest window that would satisfy the equation. The evanescent wavenumber $k_e = \omega/c_e$ and the effective acoustic wavenumber within the CWC $k_a = \omega/c_a$ are also indicated in Fig. 45. Other

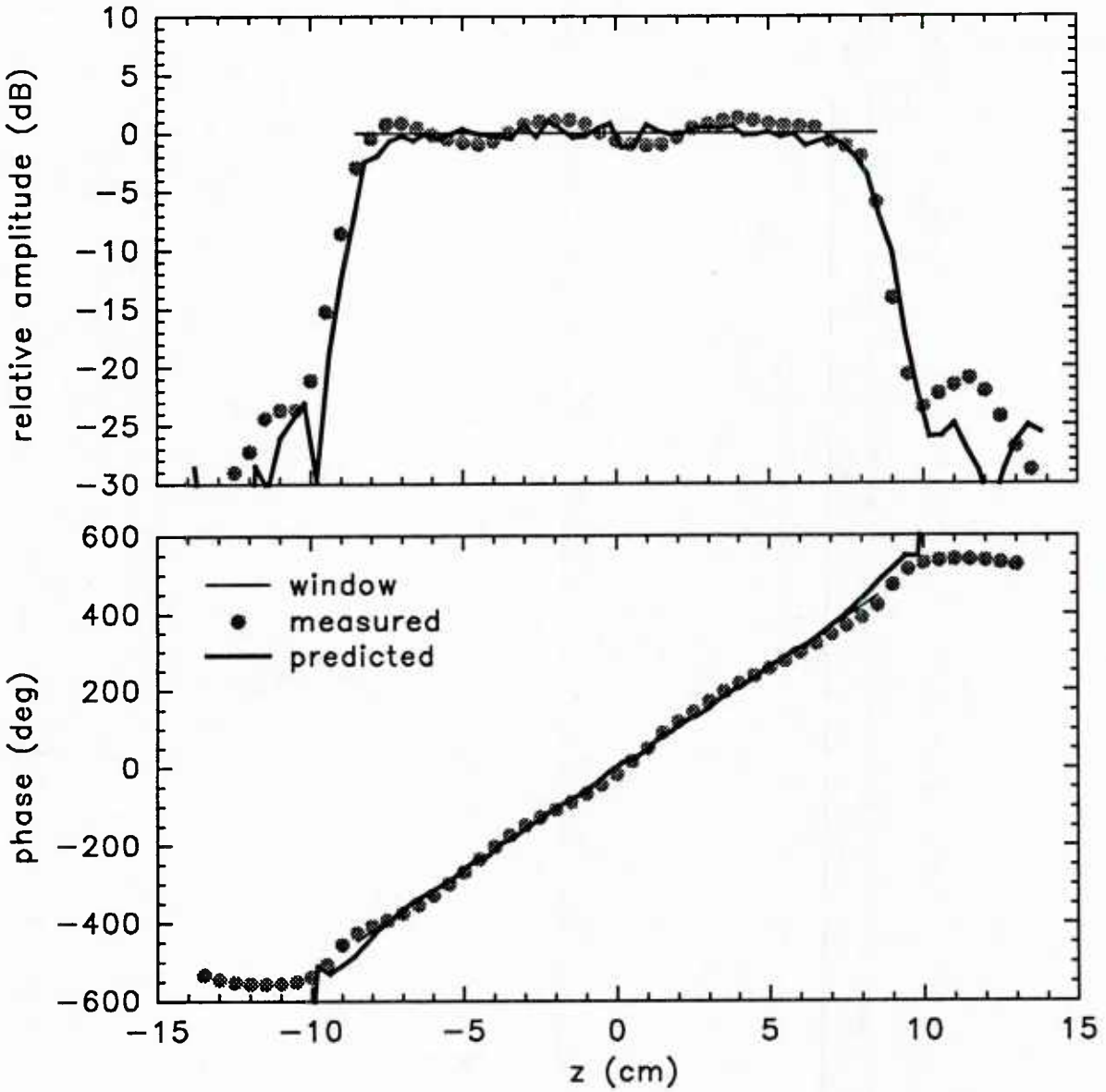

Fig. 39 — Pressures within the oil-backed CWC for a 55-m/s evanescent field at 800 Hz in a window running from -8.5 to +8.5 cm using the measured transfer matrix.

evanescent phase speeds that satisfy Eq. (1) for this window width can be found from

$$c_{e_m} = \frac{1}{\frac{1}{c_a} + \frac{m}{2fw}}, \qquad m = 1, 2, 3, \cdots \tag{69}$$

where larger values of m give lower allowed evanescent phase speeds.

In an attempt to improve the performance of the CWC, it was decided to try and eliminate any monopole component of the acoustic energy by forcing Eq. (1) to also equal zero for a wavenumber of

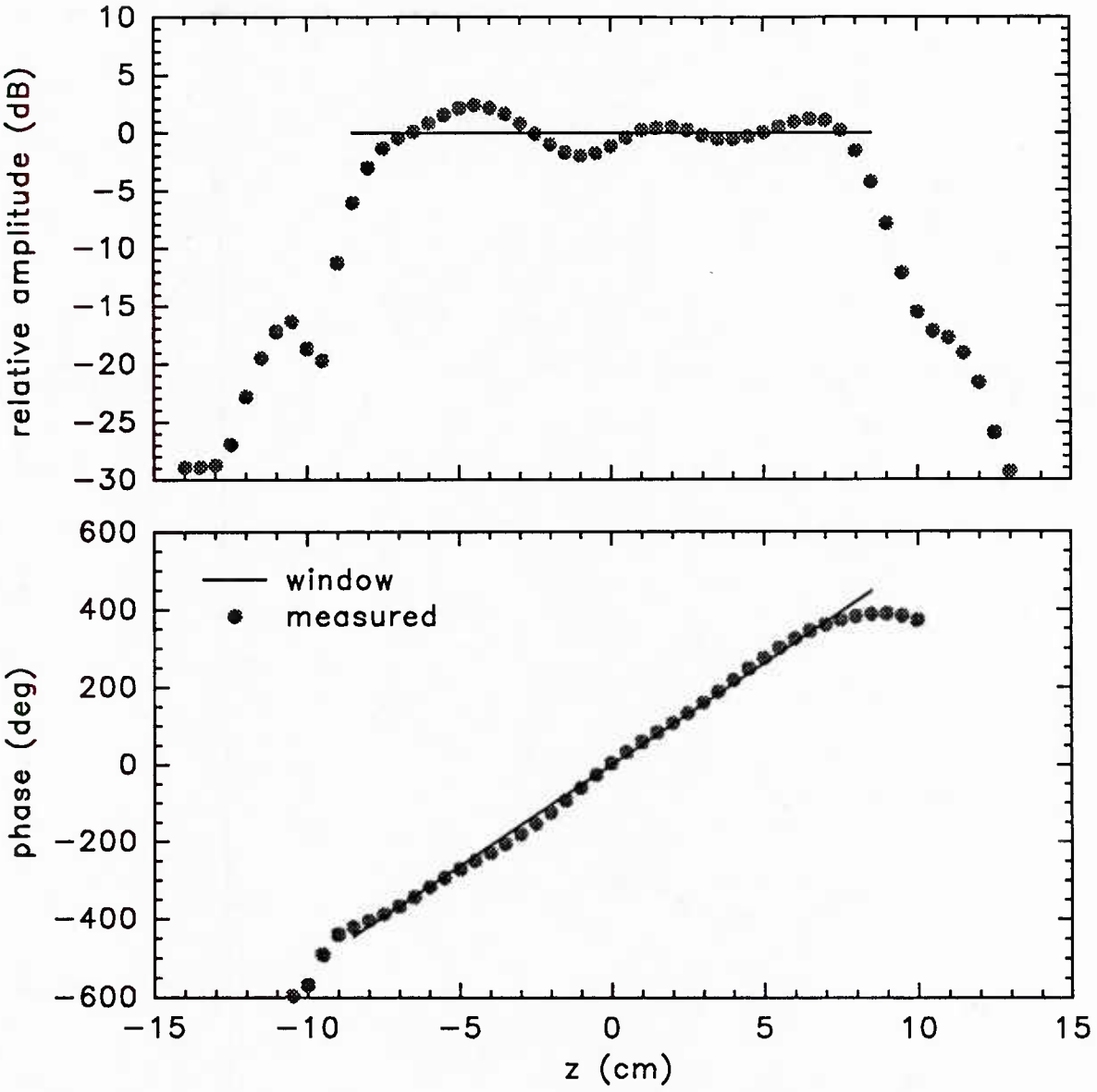

Fig. 40 — Pressure within the oil-backed CWC for a 55-m/s evanescent field at 800 Hz in a window running from -8.5 to +8.5 cm using CHIEF-I.

zero. This can be achieved with a window half-width computed from Eq. (68) using an evanescent phase speed equal to $c_a/2$. This gives window widths that contain integral numbers of evanescent wavelengths. Figure 46 shows the wavenumber spectrum for the oil-backed CWC (c_a = 282 m/s) satisfying this requirement at 800 Hz with $m = n = 1$. This gives an evanescent phase speed of 141 m/s. Unfortunately, it also gives a window half-width of 17.6 cm, which requires a window considerably larger than the prototype CWC. This would not be a problem with a full scale CWC, however, because it would be several times as long. Since the window half-width w is inversely proportional to the frequency [see Eq. (68)], it was decided to reduce the window width to a usable size for the prototype by increasing the operating frequency.

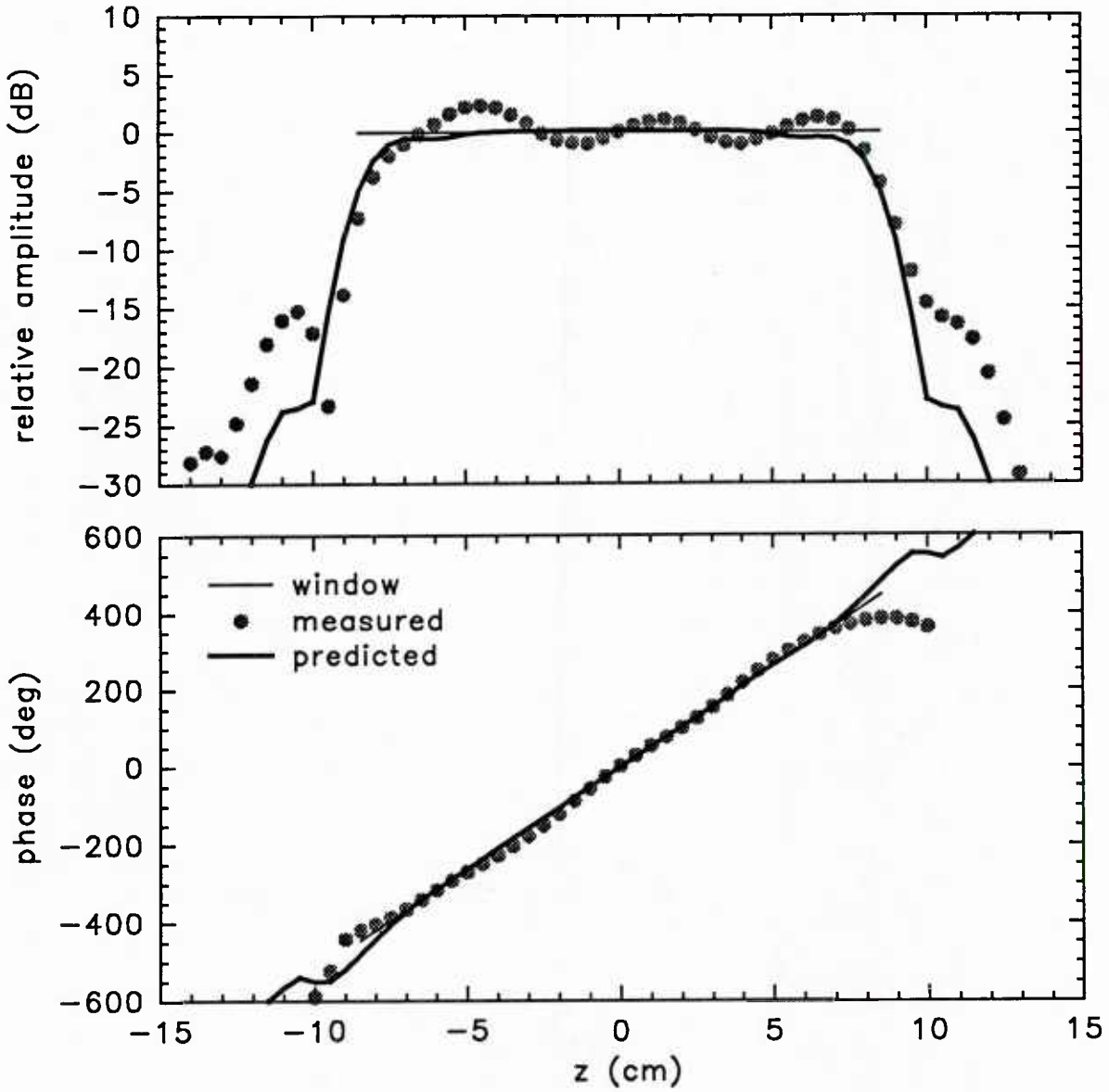

Fig. 41 — Pressures within the oil-backed CWC for a 55-m/s evanescent field at 800 Hz in a window running from -8.5 to +8.5 cm using ATILA-CHIEF.

1600 Hz with Air Outside the CWC

The frequency of operation of the CWC was raised to 1600 Hz to permit the use of a window-width, evanescent-phase-speed combination that made Eq. (1) equal zero when the wavenumber equalled both zero and the k_a within the CWC. Figure 47 shows a wavenumber spectrum for the air-backed CWC operating at 1600 Hz. For this case c_a = 284 m/s, c_e = 71 m/s, and w = 8.9 cm. It can be seen that the criteria mentioned above are satisfied. This window is four evanescent wavelengths wide.

The transfer matrix was measured for the air-backed CWC at 1600 Hz at the 70 field points used

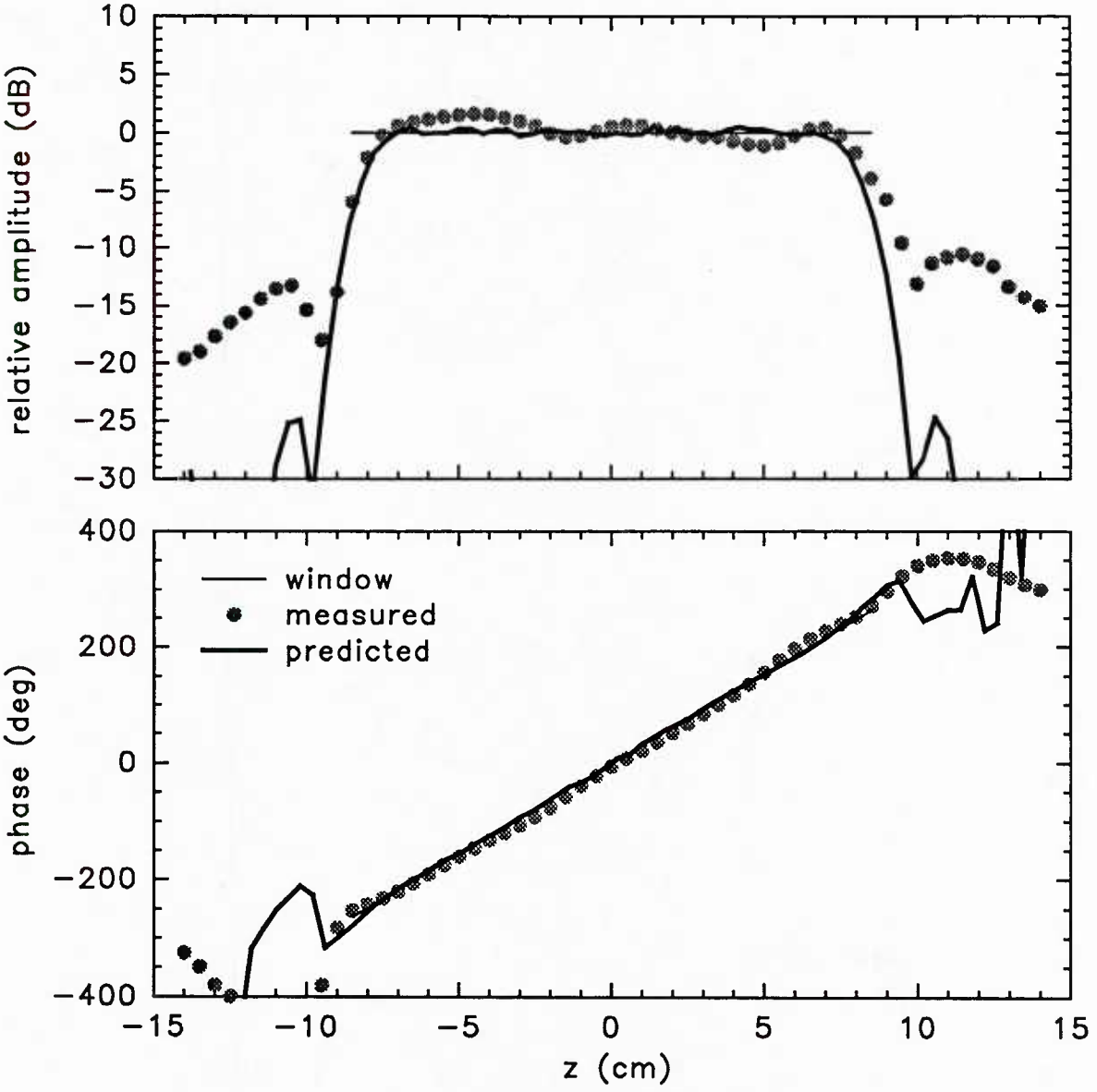

Fig. 42 — Pressures within the oil-backed CWC for a 92-m/s evanescent field at 800 Hz in a window running from -8.5 to +8.5 cm using the measured transfer matrix.

previously at 800 Hz. The measured transfer matrix was then used to calculate a set of drives to produce a 71-m/s evanescent wave in a window running from -8.9 to +8.9 cm. Figure 48 shows the predicted and measured pressure fields within the CWC for this set of drives. The measured pressure shows good agreement with the predicted pressure.

The CWC was then modeled using CHIEF-I with band 4 driven alone at 1600 Hz. The predicted and measured pressures within the CWC for this case are shown in Fig 49. These results show that the agreement between the modeled and measured pressures was not as good as it was at 800 Hz. The higher frequency (1600 Hz) is just above the third water-column resonance within the CWC. This places more demands on how accurately an idealized model duplicates the actual CWC. One example of this is the influence of the air-filled LEXAN box. If the box changes the conditions at the ends of

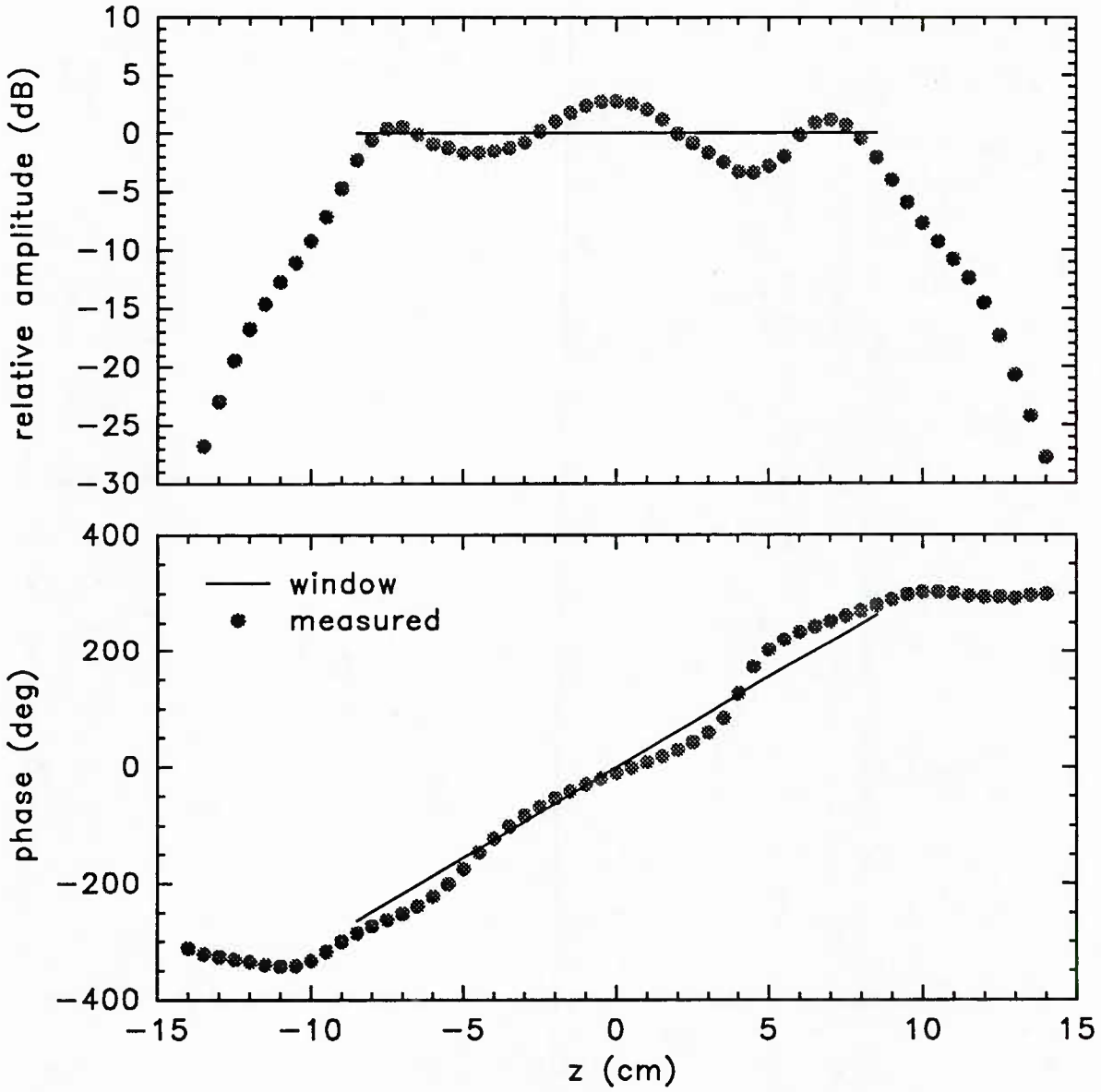

Fig. 43 — Pressure within the oil-backed CWC for a 92-m/s evanescent field at 800 Hz in a window running from -8.5 to +8.5 cm using CHIEF-I.

the CWC so that the effective length of the water column within the CWC is altered, this will change the pressure field in the water column. This effect is more pronounced at higher frequencies and especially near resonances.

Drives were then computed specifying the same desired pressure field as for Fig. 48 but using the CHIEF-I model to determine the transfer matrix. Figure 50 shows the measured pressure field within the CWC for this set of drives. These results show poor performance in both amplitude and phase. This is most likely due to the inaccuracy of the model. Although the differences between the model and the measured pressures may not appear to be very great when a single band is driven, the results from single-band drives are being used here to calculate a set of 40 complex drives intended to produce an evanescent field within the CWC that has a wavelength of only 4.4 cm, thereby increasing

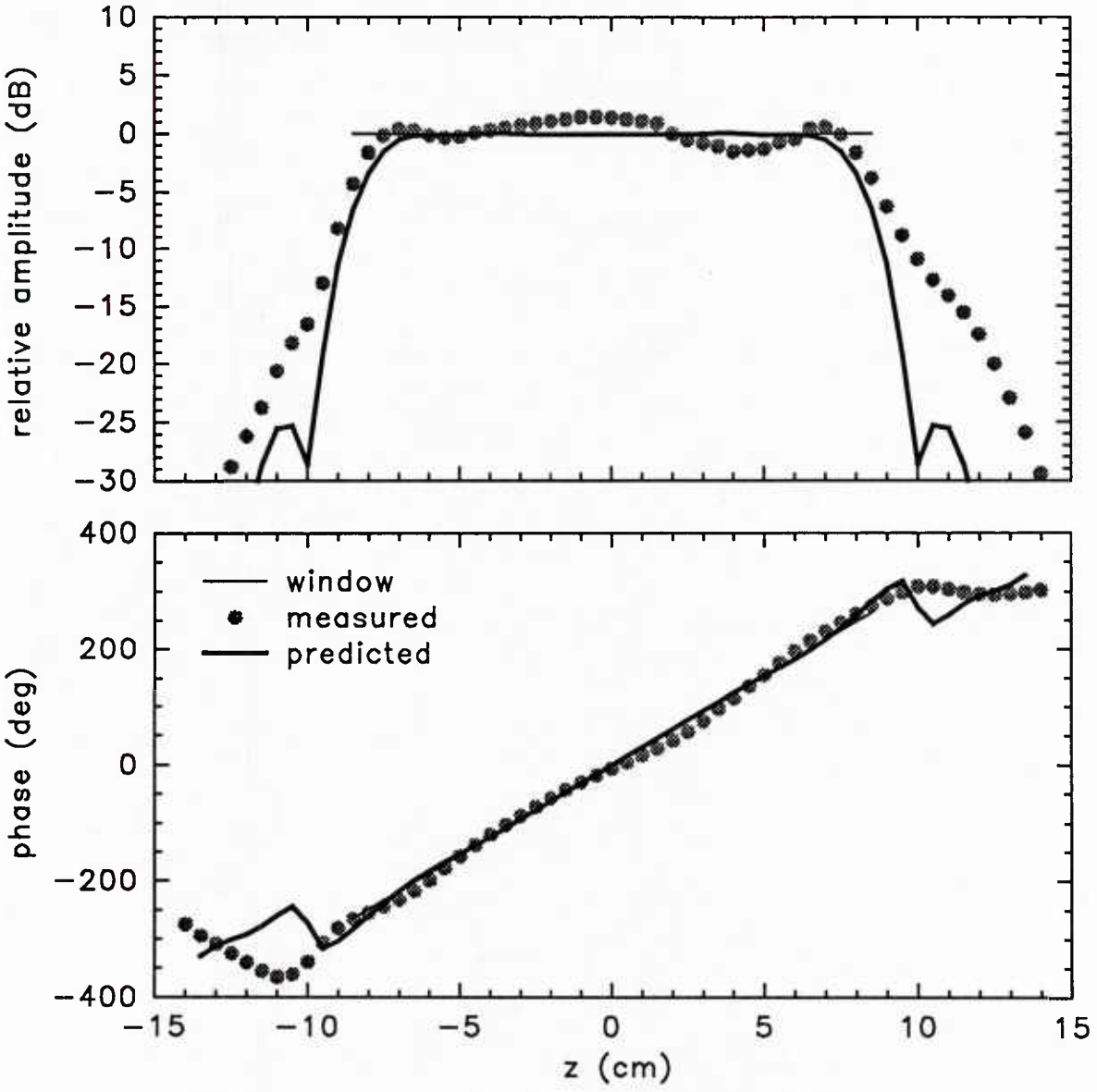

Fig. 44 — Pressures within the oil-backed CWC for a 92-m/s evanescent field at 800 Hz in a window running from -8.5 to +8.5 cm using ATILA-CHIEF.

the effects of the errors. This situation is aggravated by the fact that at this evanescent wave speed there are only 7.4 bands per wavelength. This is below the minimum of 10 bands per wavelength recommended for planar arrays [19].

Drives were also computed for this case using the RING-CHIEF model to determine the transfer matrix. Figure 51 shows the predicted and measured pressure fields within the CWC for this set of drives. These data also show poor performance as with the CHIEF-I model.

To determine if the performance of the model would improve with higher evanescent wave speeds, drives were calculated for the same window size but with an evanescent wave speed of 142 m/s using the measured transfer matrix. Figure 52 shows the predicted and measured pressure fields

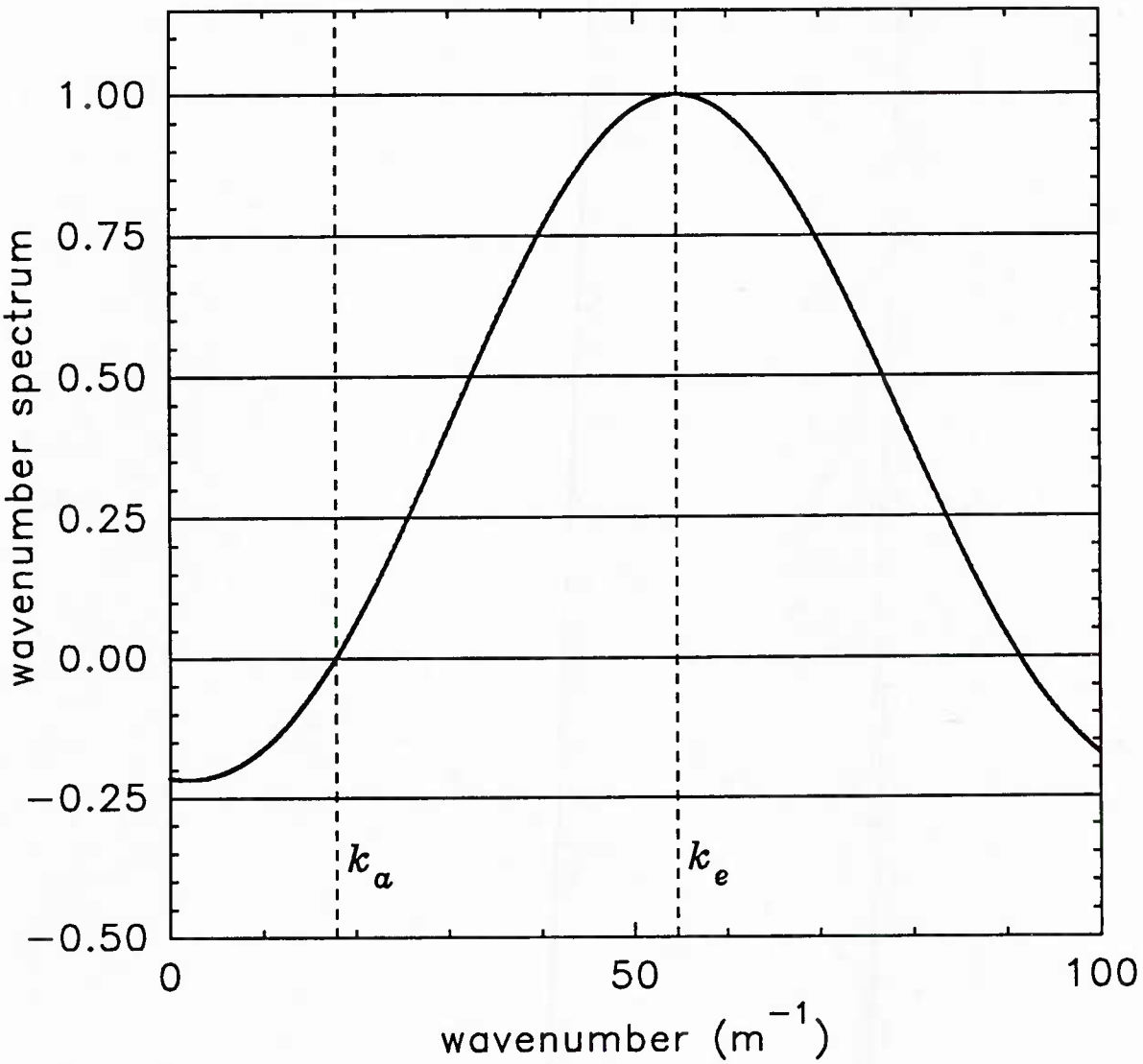

Fig. 45 — Wavenumber spectrum [Eq. (1)] for a 92-m/s pressure field at 800 Hz in a window from -8.5 to +8.5 cm in the oil-backed CWC.

within the CWC for this set of drives. The results show uniformity inside the window that is almost as good as the 71-m/s case for the measured transfer matrix.

Drives were then computed for this case using the CHIEF-I model and the RING-CHIEF model to determine the transfer matrices. Figures 53 and 54 show the pressure fields within the CWC for these two cases. These results show general agreement with the results from the measured transfer matrix although the amplitude uniformity inside the window is not as good. The greatly improved results with the models (compared to the 71-m/s case) do indicate that the demands on the accuracy of the models are lessened for higher evanescent wave speeds.

1600 Hz with Oil Outside the CWC

To evaluate the oil-backed configuration at 1600 Hz, the CWC was operated with castor oil

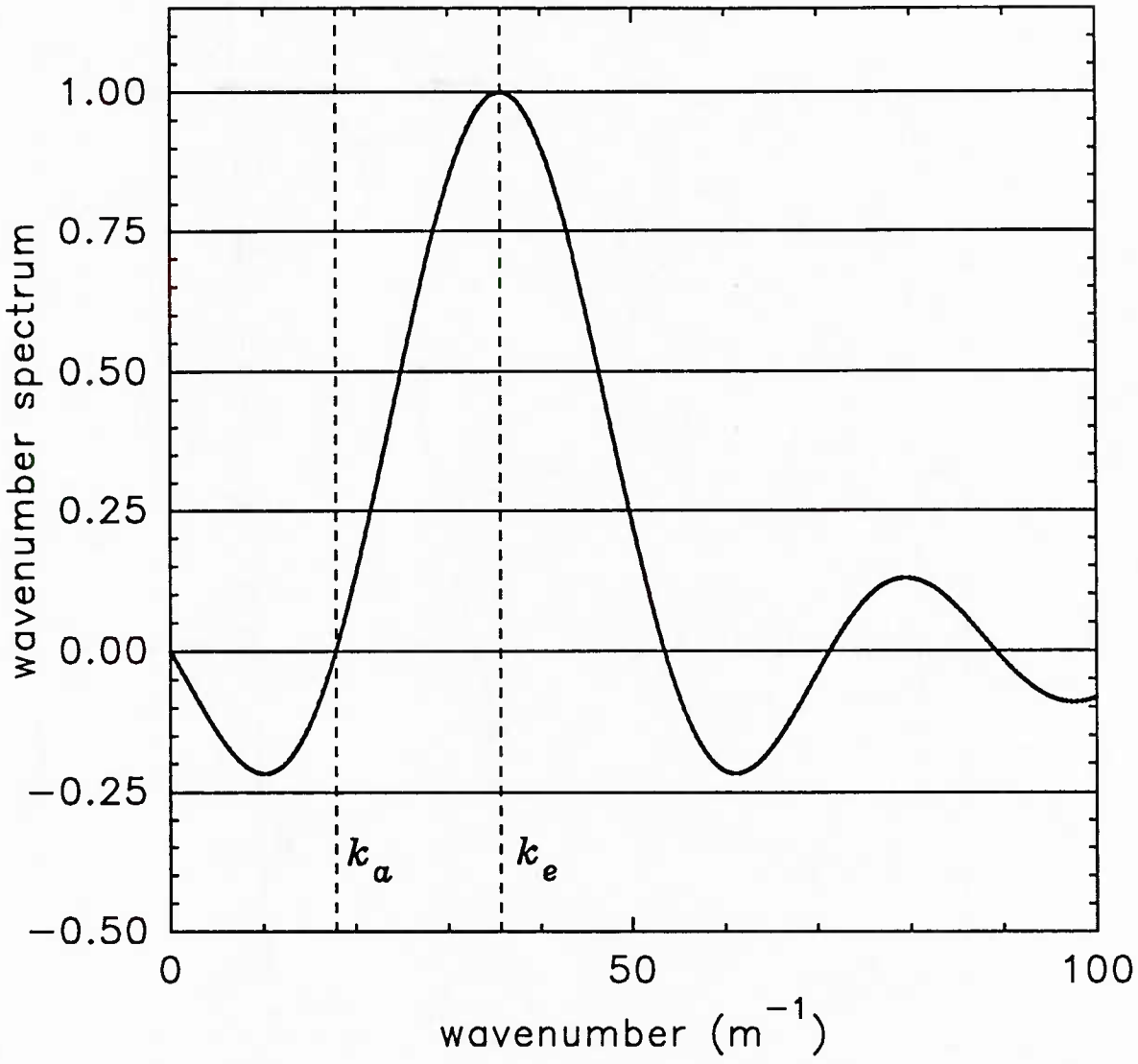

Fig. 46 — Wavenumber spectrum for a 141-m/s evanescent pressure field at 800 Hz in a window from -17.6 to +17.6 cm in the oil-backed CWC (c_a = 282 m/s).

inside the LEXAN box. The transfer matrix was measured with this configuration and used to calculate drives to produce a 66-m/s evanescent wave in a window running from -8.3 to +8.3 cm. Figure 55 shows the predicted and measured pressure fields within the CWC for this set of drives. This evanescent phase speed corresponds to 7 bands per wavelength. This data shows that the uniformity of the pressure inside the window is degrading even when using the measured transfer matrix.

Radiation-impedance matrices for 1600 Hz were computed with CHIEF for use by RING-CHIEF and ATILA-CHIEF. Predicted pressures were then computed using both of these models with band 4 driven alone. Figure 56 shows the pressures predicted by RING-CHIEF and ATILA-CHIEF and the measured pressures within the CWC for this case. This data shows that ATILA-CHIEF definitely does a better job of modeling the CWC at 1600 Hz than RING-CHIEF but still shows significant variation from the measured pressure.

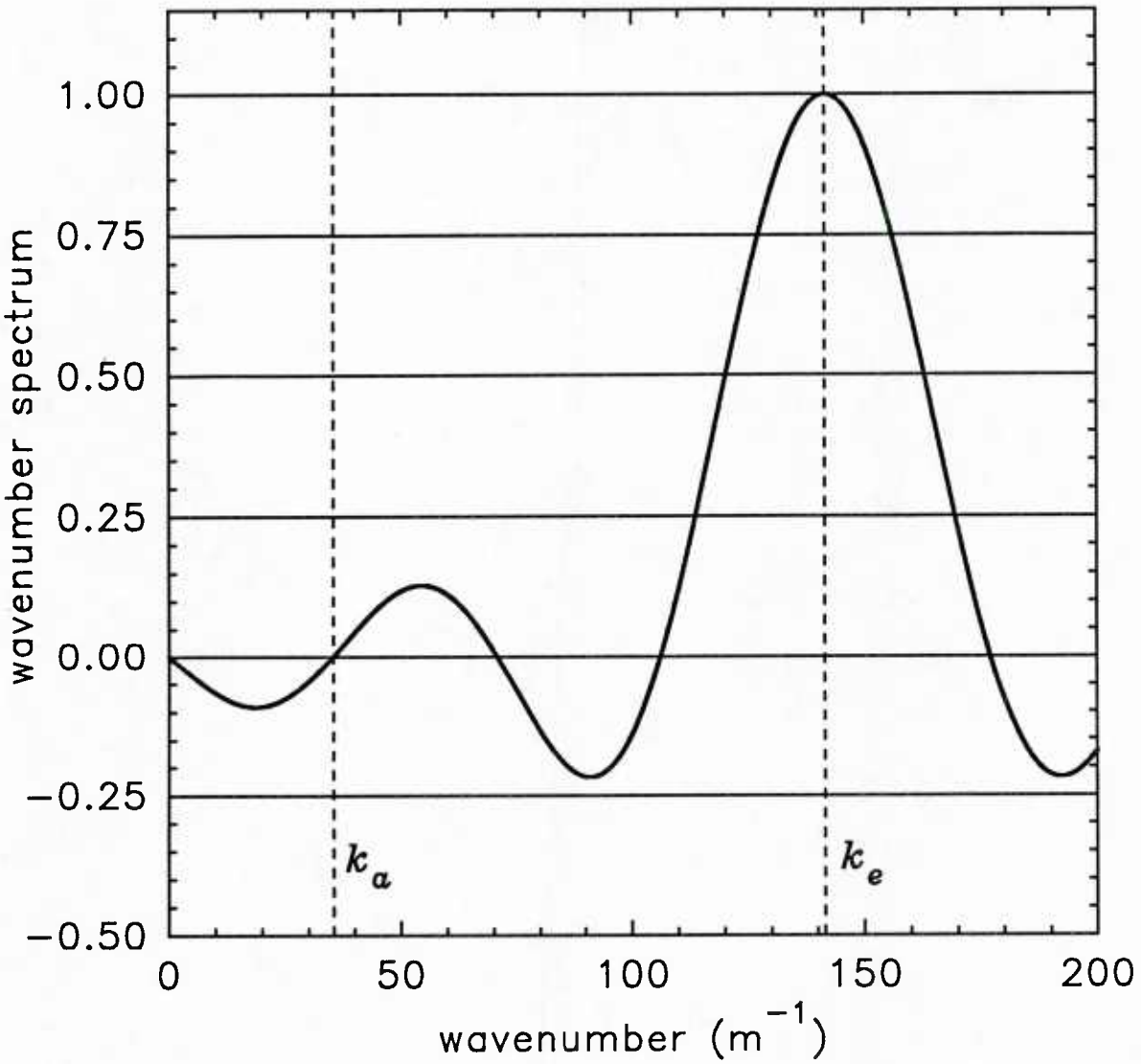

Fig. 47 — Wavenumber spectrum for a 71-m/s evanescent pressure field at 1600 Hz in a window from -8.9 to +8.9 cm in the air-backed CWC (c_a = 284 m/s).

Drives were then computed to produce a 66 m/s evanescent wave using the ATILA-CHIEF model to determine the transfer matrix. Figure 57 shows the predicted and measured pressure fields within the CWC for this set of drives. This shows very poor uniformity as with the air-backed case at 71 m/s for the same reasons.

To reduce the number of bands per evanescent wavelength, drives were computed for an 88-m/s evanescent wave in the same window using the measured transfer matrix. This corresponds to 9.2 bands per evanescent wavelength. Figure 58 shows the predicted and measured pressure field within the CWC for this set of drives. This shows much better uniformity than for the 66-m/s field.

Drives were computed for this case using the ATILA-CHIEF model to determine the transfer matrix. Figure 59 shows the pressure fields within the CWC for this set of drives. The results show

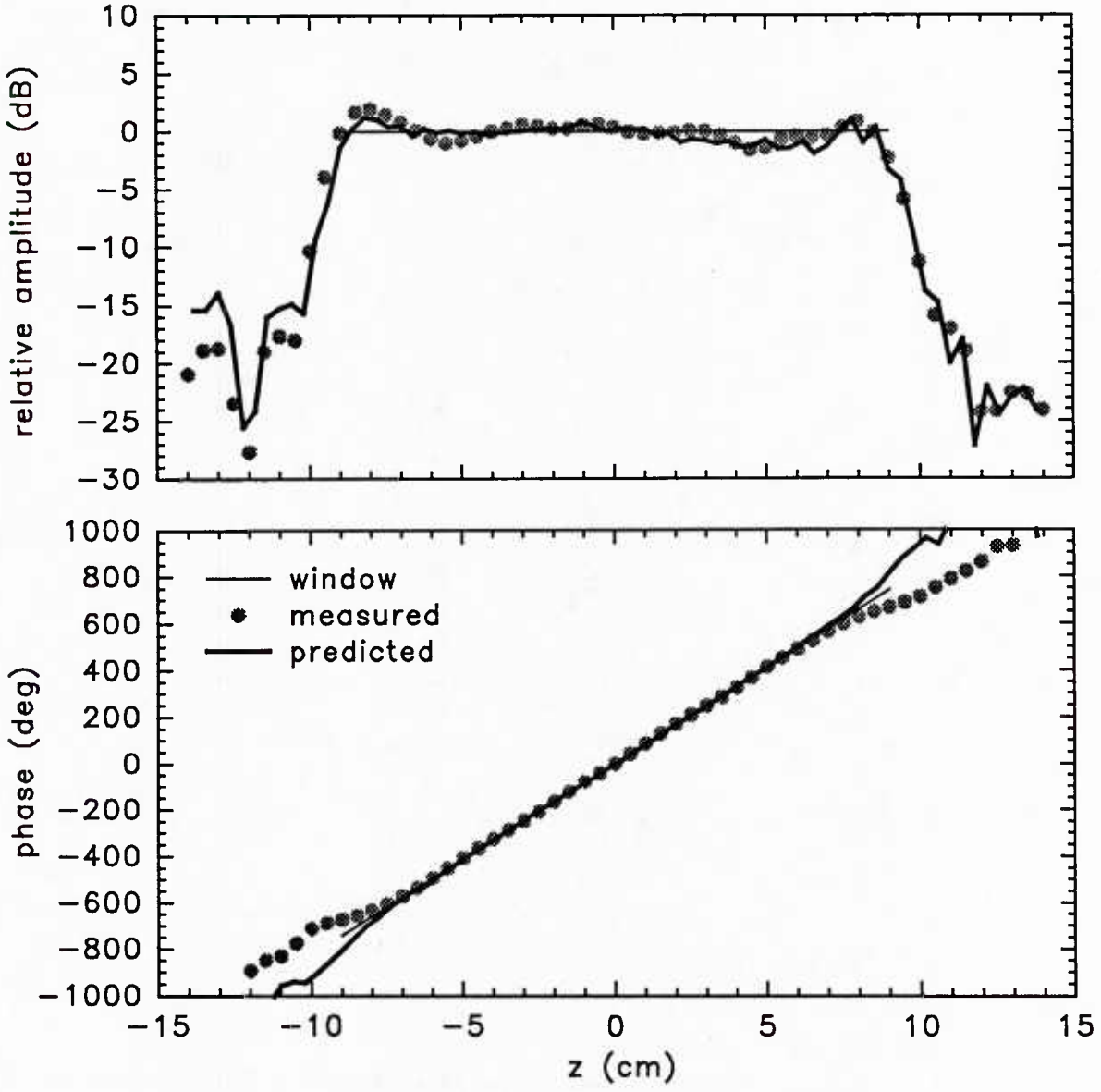

Fig. 48 — Pressures within the air-backed CWC for a 71-m/s evanescent field at 1600 Hz in a window running from -8.9 to +8.9 cm using the measured transfer matrix.

much better performance than for the ATILA-CHIEF model at 66-m/s but still not as good as with the drives computed using the measured transfer matrix.

Radial Variation in Pressure

On numerous occasions, at various evanescent wave speeds, attempts were made to measure any variation in the pressure within the CWC as a function of radial position. This was done by deflecting the monofilament line, and therefore the hydrophone, from the centerline to the inner wall of the CWC at a fixed z position while measuring the amplitude. No significant variations in amplitude were ever observed. This uniformity was made possibly because of the relatively slow natural propagation speed within the PVDF CWC. Although the lowest evanescent speed for which data is presented (55-m/s) is

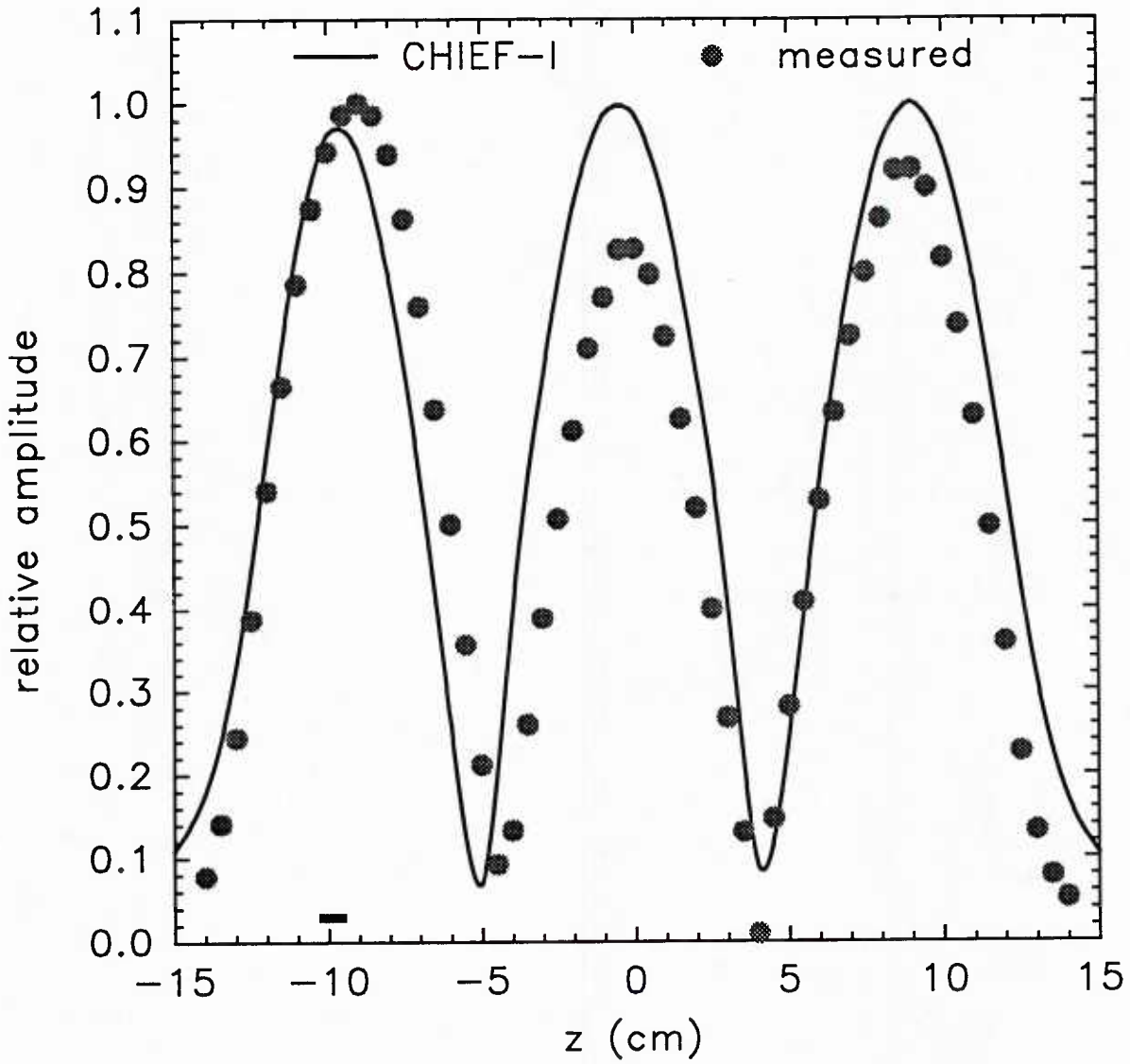

Fig. 49 — Predicted and measured pressures within the air-backed CWC with only band 4 driven at 1600 Hz. The predicted pressures were calculated using the CHIEF-I model.

1/27 of the sound speed in open water, this only requires a wavenumber multiplier of about 5 for the PVDF CWC. As can be seen from Fig. 2, the pressure would only be expected to drop by about 0.2 dB at the center of the CWC relative to the wall for this wavenumber multiplier. If a rigid-walled CWC were used, the pressure drop near the center would be about 6 dB.

CONCLUSIONS AND RECOMMENDATIONS

An investigation of a prototype CWC has been performed. The study included both theoretical and experimental investigations of the CWC. Various methods for determining the transfer matrix for the CWC were explored. The results of the investigations show that reasonably uniform nonacoustic-wavenumber pressure fields can be created within the CWC.

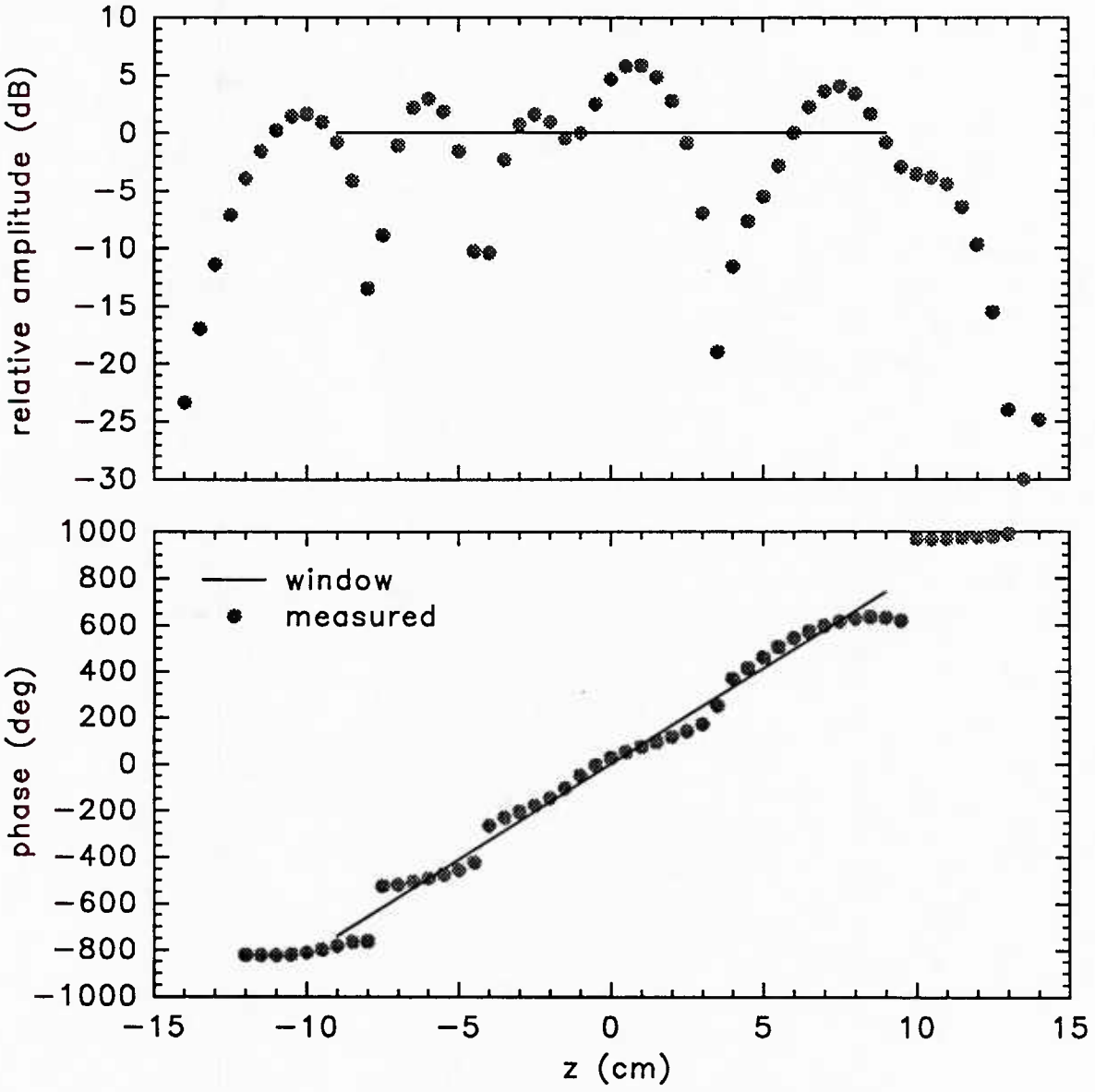

Fig. 50 — Pressures within the air-backed CWC for a 71-m/s evanescent pressure field at 1600 Hz in a window running from -8.9 to +8.9 cm using CHIEF-I.

The analysis of the pressure field inside an infinite-length cylindrical shell with a specified normal velocity showed the radial dependence of the evanescent pressure field inside the shell. From this it was concluded that the wavenumber multiplier should be kept small to keep the pressure within the CWC from dropping rapidly as the distance from the wall is increased. This can be accomplished if a CWC is constructed with a low natural propagation speed in the water within the CWC. The analysis of an infinite-length, cylindrical, elastic tube filled with a fluid and surrounded by another fluid showed that a PVDF CWC can be constructed that has propagation speeds in the water within the CWC that are less than one-fifth the open-water sound speed. These results were verified by calculating the propagation speed within the CWC using measured resonant frequencies.

The measured pressure fields within the CWC with a single band driven were compared with the

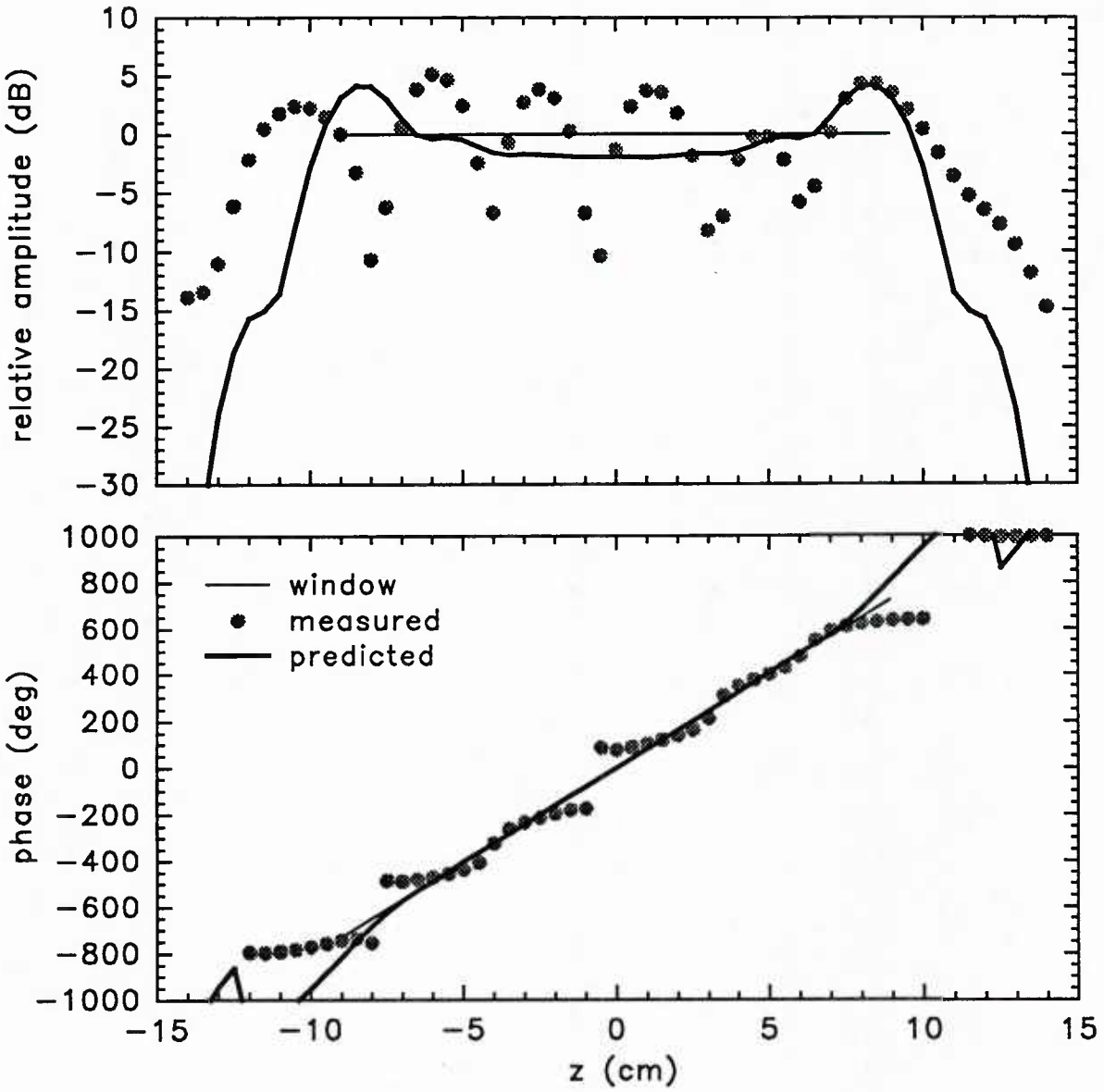

Fig. 51 — Pressures within the air-backed CWC for a 71-m/s evanescent field at 1600 Hz in a window running from -8.9 to +8.9 cm using RING-CHIEF.

pressure fields predicted by the CHIEF-I, RING-CHIEF, and ATILA-CHIEF models. With a drive frequency of 800 Hz the pressures predicted by the models are very similar and show fairly good agreement with the measured pressure. With a drive frequency of 1600 Hz the ATILA-CHIEF model does a better job of matching the measured pressures than RING-CHIEF but still shows significant differences.

Evanescent pressure fields were created within the CWC with drives that were computed using transfer matrices that were either measured or determined using the models. The technique of adding a small real quantity to the diagonals of the reduced transfer matrix resulted in drives with more uniform amplitudes and phases that were more usable by the drive system to produce uniform evanescent fields. It was also found that the uniformity of the evanescent field was poor using

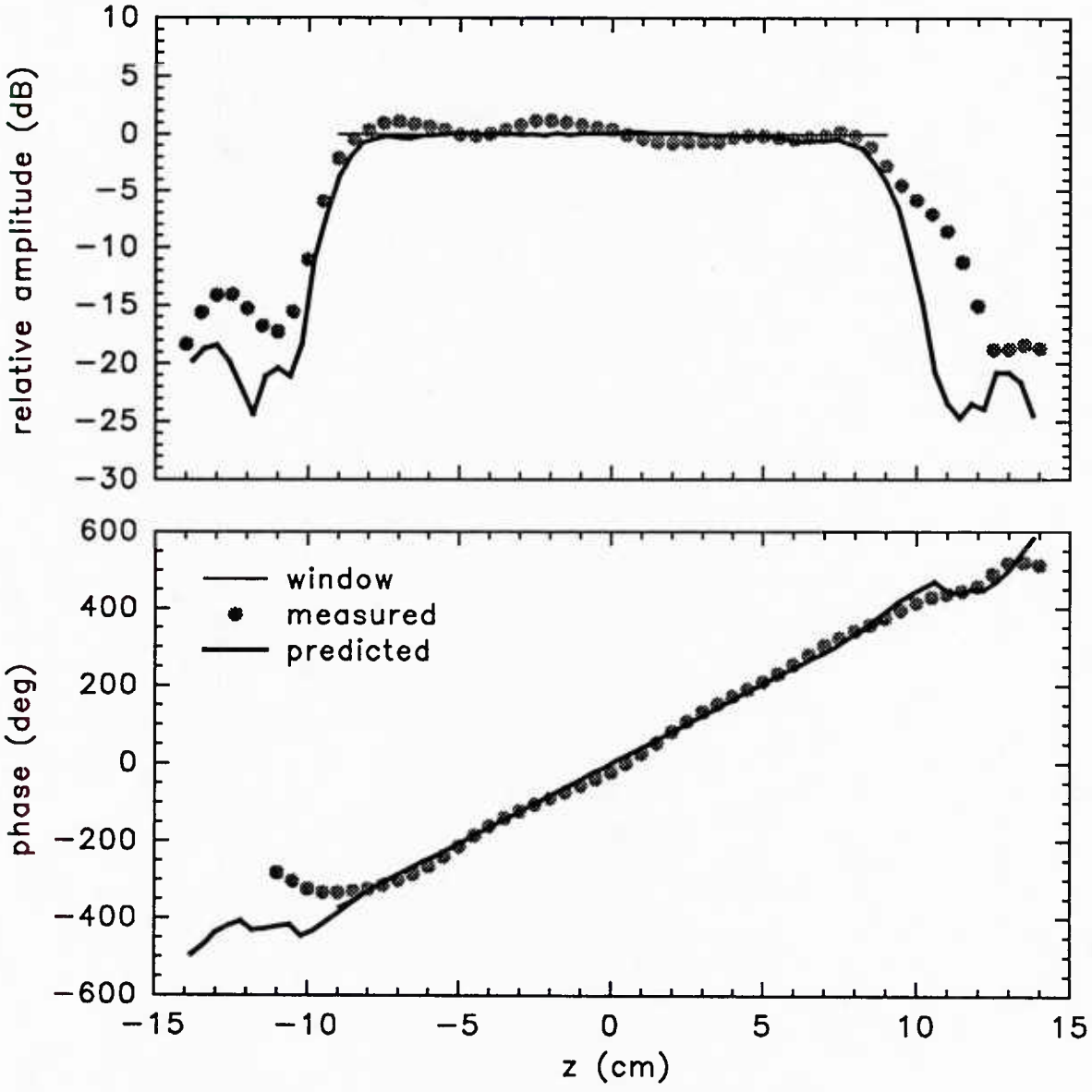

Fig. 52 — Pressures within the air-backed CWC for a 142-m/s evanescent field at 1600 Hz in a window running from -8.9 to +8.9 cm using the measured transfer matrix.

modeled transfer matrices if the pressure within the CWC was allowed to remain large out to the ends of the CWC. The performance was greatly improved if drives were computed that forced the pressure down in the region between the window and the ends of the CWC.

With 800-Hz drive, the uniformity of the evanescent pressure field inside the window was about as good with any of the models. However, none of the models produced evanescent-field uniformity that was as good as that achieved from measured transfer matrices.

The technique of minimizing any monopole energy by forcing Eq. (1) to equal zero when the wavenumber equals zero seemed to improve the performance of the CWC slightly when using

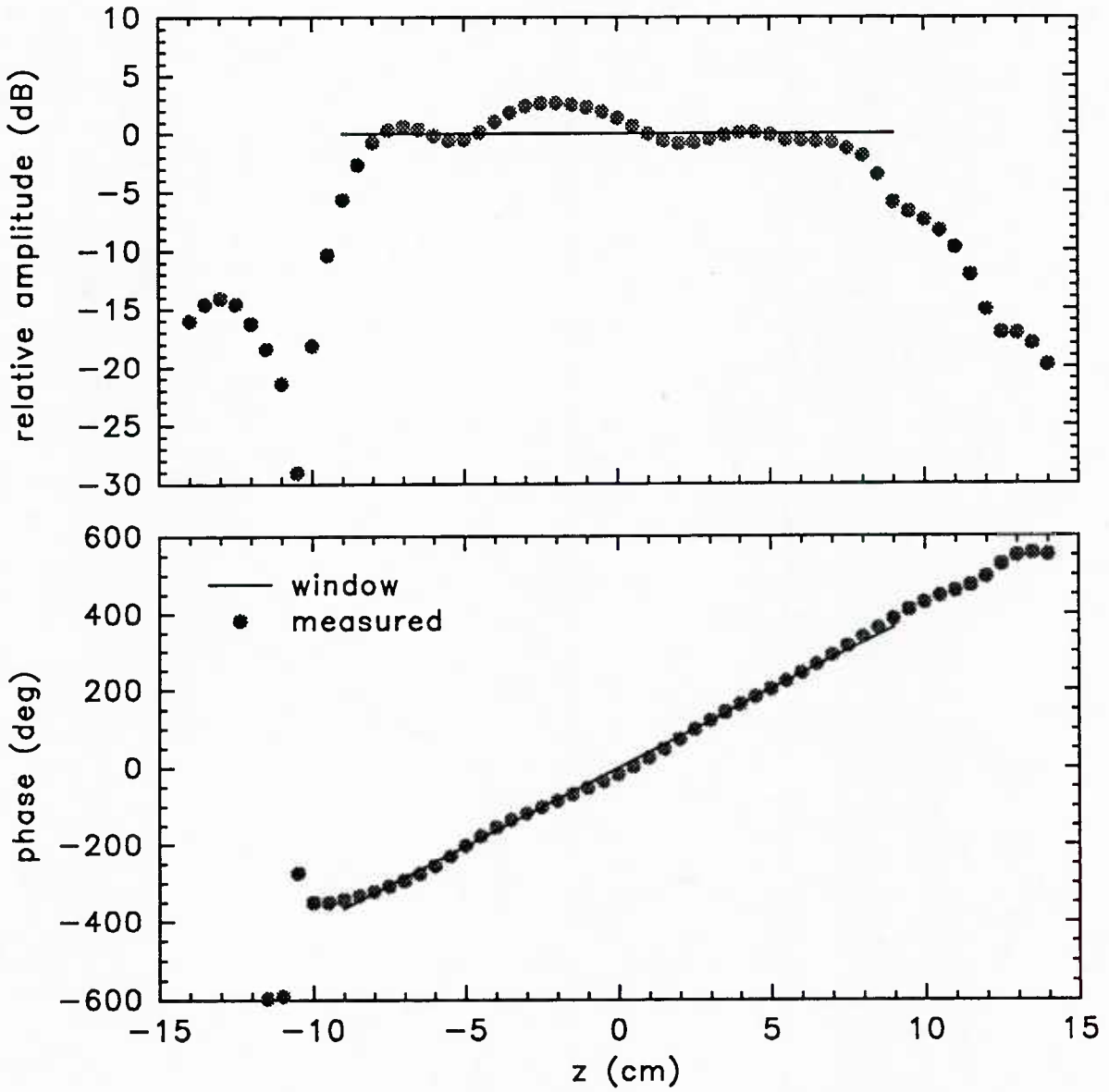

Fig. 53 — Pressures within the air-backed CWC for a 142-m/s evanescent field at 1600 Hz in a window running from -8.9 to +8.9 cm using CHIEF-I.

measured transfer matrices. The agreement with predicted pressures throughout most of the window was generally within ±1.5 dB. Unfortunately, the shift to higher frequency (required because of the short length of the prototype) also brought about more differences between measured pressures within the CWC and pressures predicted by the models. Using transfer matrices computed from models at 1600 Hz, the uniformity of the evanescent pressure field inside the window was definitely better with the more accurate ATILA-CHIEF model. This difference was greatest for higher evanescent wavenumbers (i.e., lower evanescent wave speeds). The performance at 1600 Hz with drives computed using measured transfer matrices was considerable better than the results using transfer matrices computed from models.

It was found that the criterion of a minimum of ten bands per evanescent wavelength that was

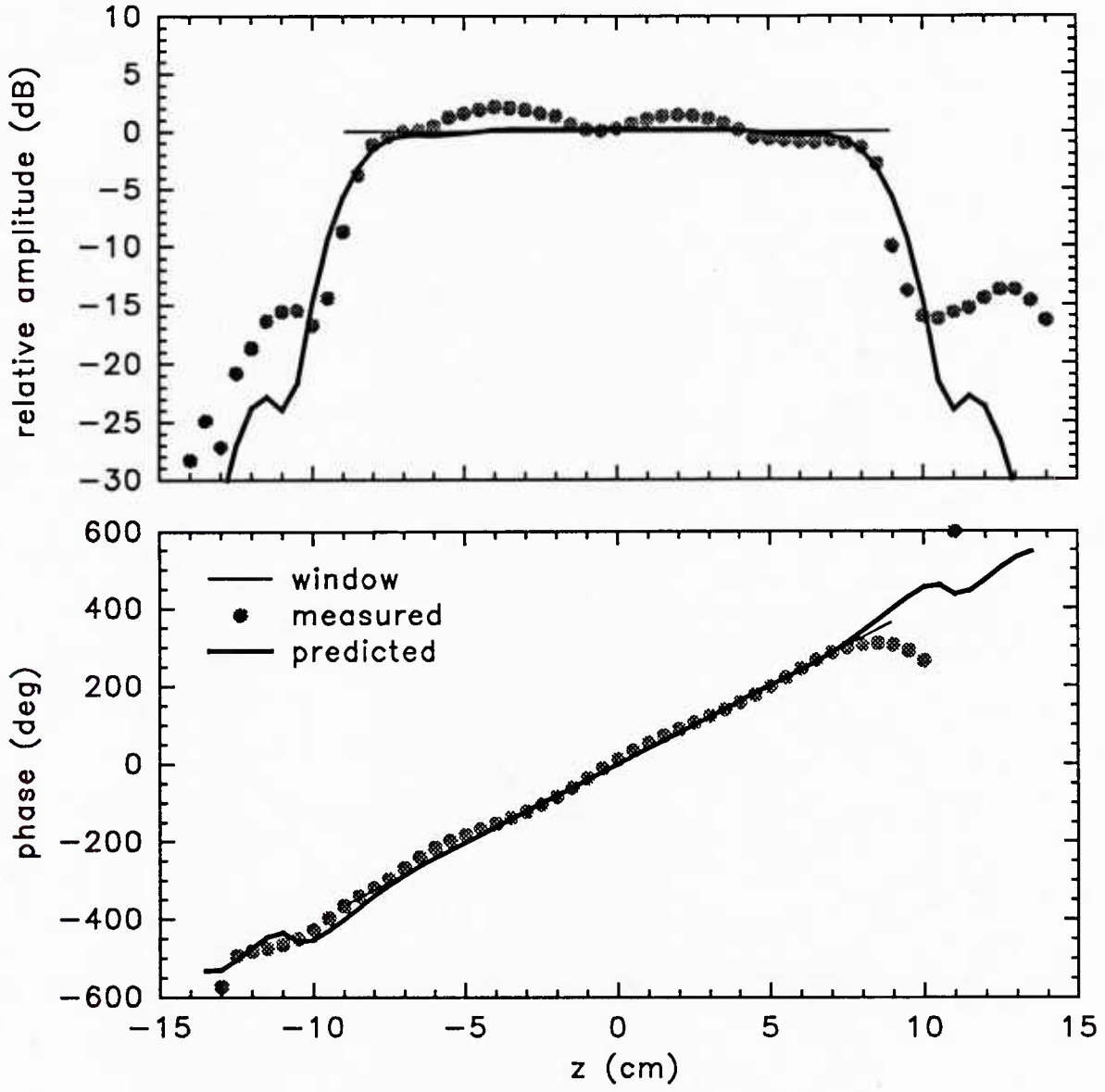

Fig. 54 — Pressures within the air-backed CWC for a 142-m/s evanescent field at 1600 Hz in a window running from -8.9 to +8.9 cm using RING-CHIEF.

previously recommended for planar arrays is about right for the CWC. Degradation of the evanescent field was obvious at seven bands per wavelength with measured transfer matrices and was evident below about nine bands per wavelength when using the models to determine the transfer matrices.

Overall, the performance of the CWC with measured transfer matrices was always as good as or better than with the models. In many cases (particularly at the higher frequency) the results with measured transfer matrices were much better than with the models. This should not be surprising since the models are idealized approximations of a perfect CWC while the measured transfer matrices determine the true interactions for the actual CWC in its operating environment. This situation would be even worse with an invariably more complex full-size CWC than with the simple prototype. This leads to the conclusion that a practical CWC should be capable of measuring the transfer matrix rather

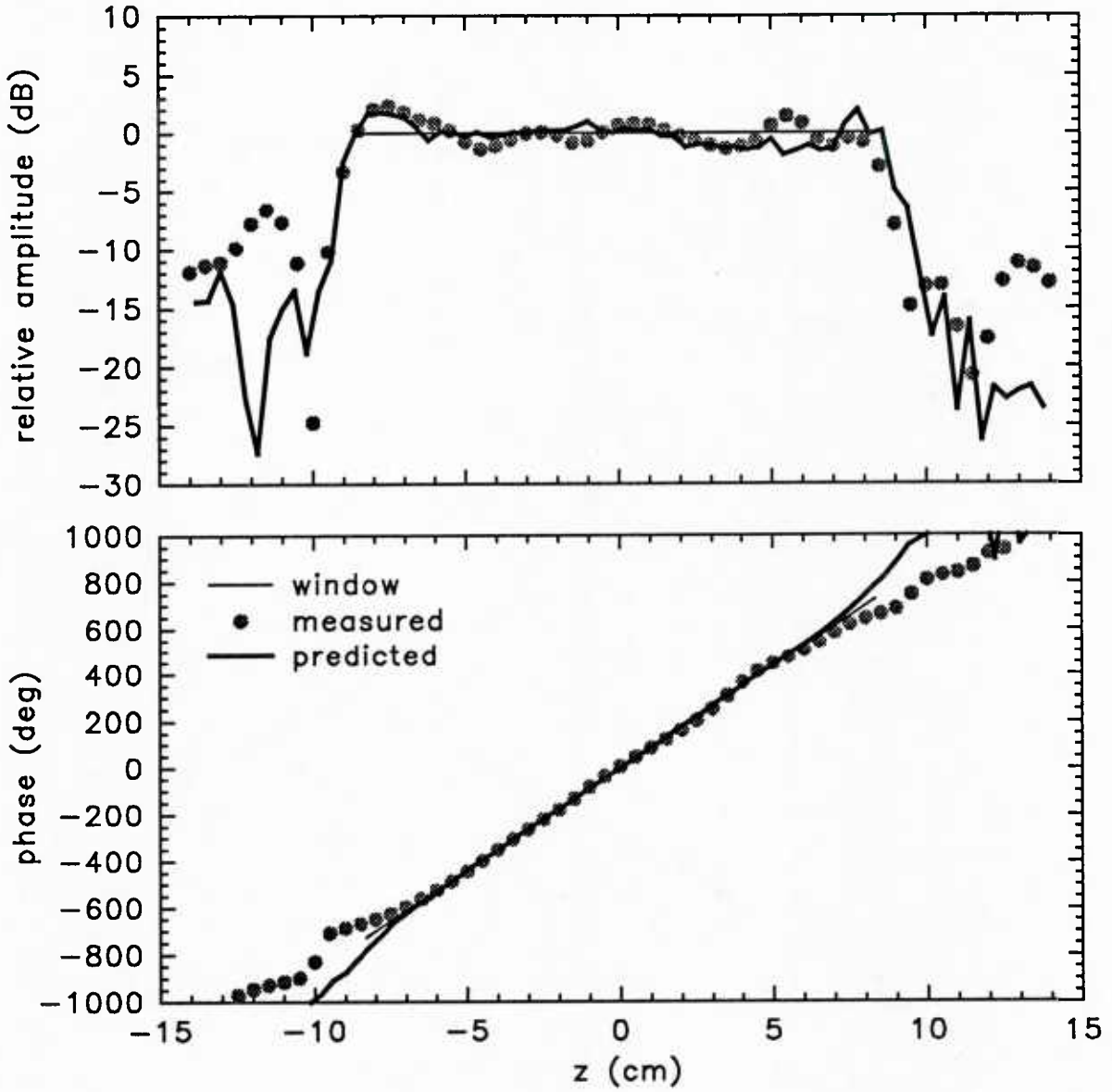

Fig. 55 — Pressures within the oil-backed CWC for a 66-m/s evanescent field at 1600 Hz in a window running from -8.3 to +8.3 cm using the measured transfer matrix.

than relying on a model of the system.

An operational CWC would have a diameter several times as large as the prototype and be several times as long in order to accommodate towed-sonar-array modules. It must have narrower bands in order to produce higher evanescent wavenumbers. This fact, combined with the additional length, means that there would have to be many times the number of driven bands used in the prototype. If each drive must be independently controlled, there must be hundreds (perhaps thousands) of sets of drive electronics (i.e., power amplifiers, etc.). It is possible that this number could be dramatically reduced, however. It was noted that the drives to the interior bands (bands that were not near the ends of the CWC) tended to have relatively uniform amplitudes and a constant phase increment that coincided with the phase of the evanescent wave. It is therefore possible that many of

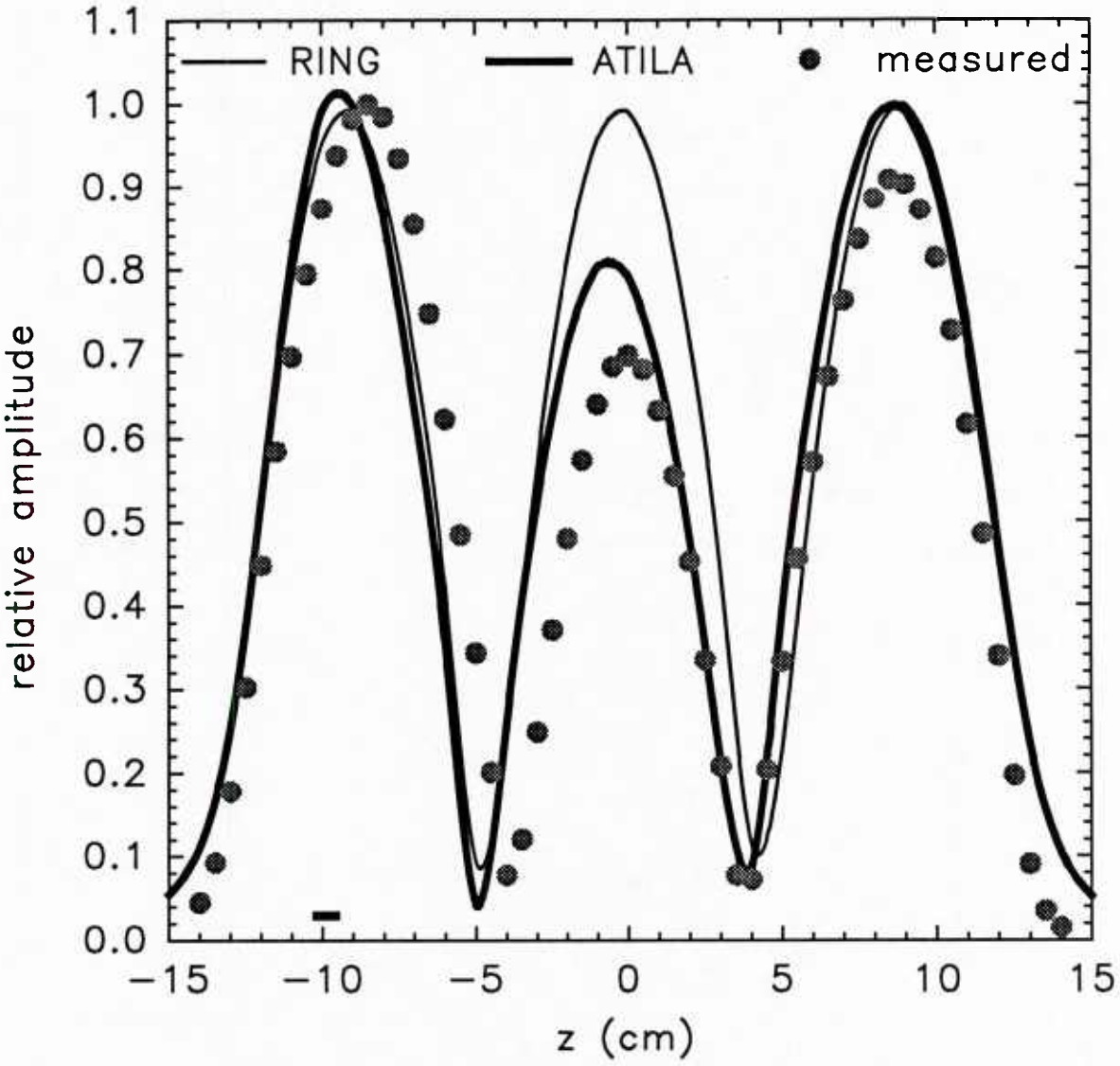

Fig. 56 — Pressures within the oil-backed CWC with only band 4 driven at 1600 Hz. Predicted pressures were calculated using RING-CHIEF and ATILA-CHIEF models.

the interior bands could be driven in parallel by a single set of drives that exploits this periodicity (one period per evanescent wavelength). This would have to be confirmed by additional experimentation, however, with a CWC that is longer and has more bands than the current prototype.

ACKNOWLEDGEMENTS

This research would never have reached fruition were it not for my doctoral committee chairman, Dr. Peter Rogers. His encouragement before and during my residency at Georgia Institute of Technology and his advice during the course of this research have been invaluable. The theoretical and experimental work was performed at the facilities of the Naval Research Laboratory - Underwater Sound Reference Detachment in Orlando, Florida. Several members of the technical staff at NRL and other individuals provided valuable assistance during this endeavor. Dr. A. Lee Van Buren on many occasions made valuable suggestions and critiques of the research. The prototype CWC and much of

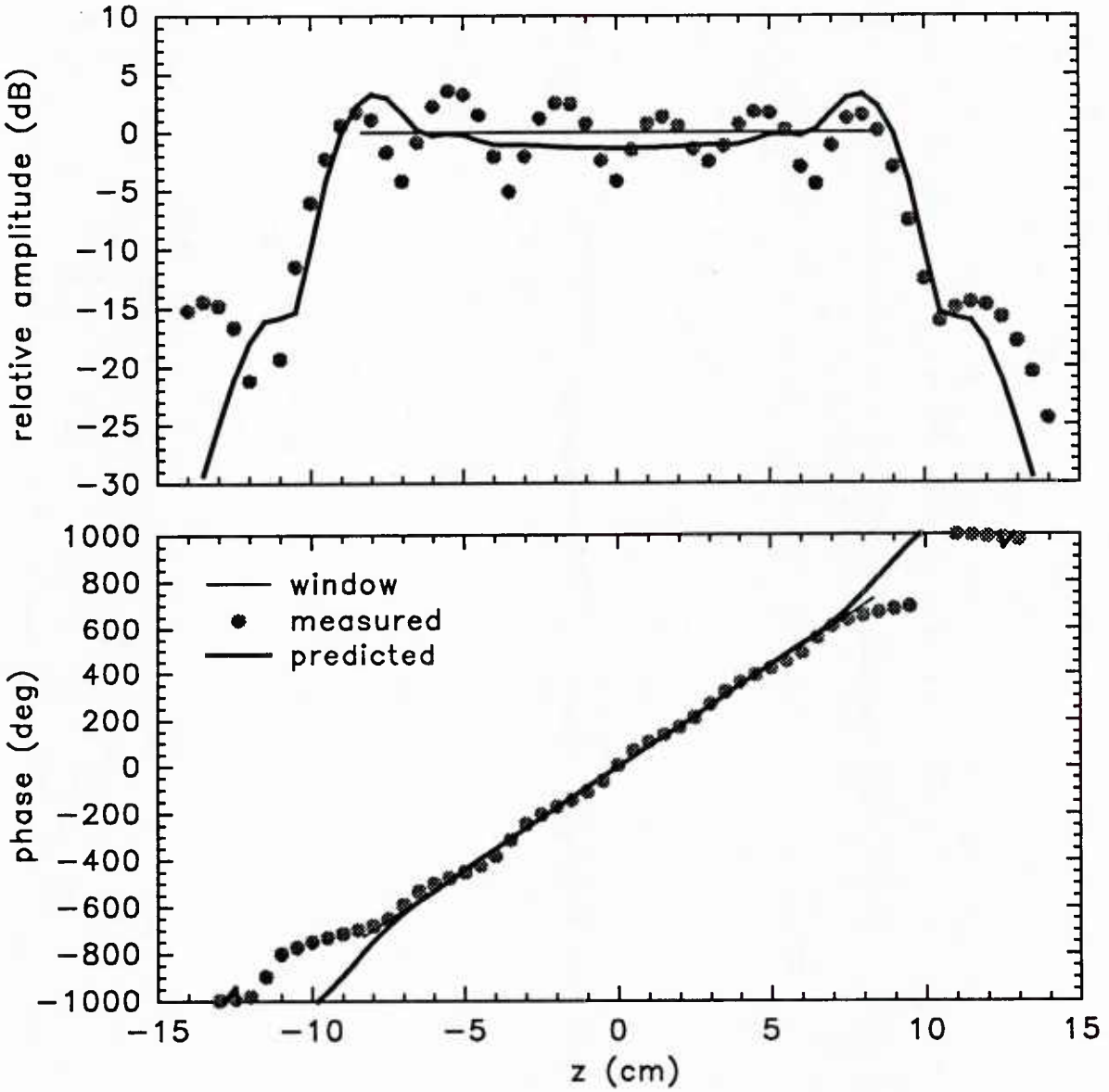

Fig. 57 — Pressures within the oil-backed CWC for a 66-m/s evanescent field at 1600 Hz in a window running from -8.3 to +8.3 cm using ATILA-CHIEF.

the experimental rigging were constructed by Mr. Sam Petrie. Ms. Clementina Siders, Dr. Michele McCollum, and Dr. Bertrand Dubus provided valuable assistance in setting up the ATILA-CHIEF model of the CWC. Dr. Pieter Dubbelday and Dr. Kurt Rittenmyer provided and operated the LDV equipment used to measure the wall velocity of the CWC. Mr. David Trivett contributed several valuable suggestions during the course of this research. I am very grateful to my wife, June, for the many sacrifices she has made and for the unwavering support she has provided, without which this lengthy undertaking would not have been completed.

This research was jointly supported by the Office of Naval Research and the Office of Naval Technology.

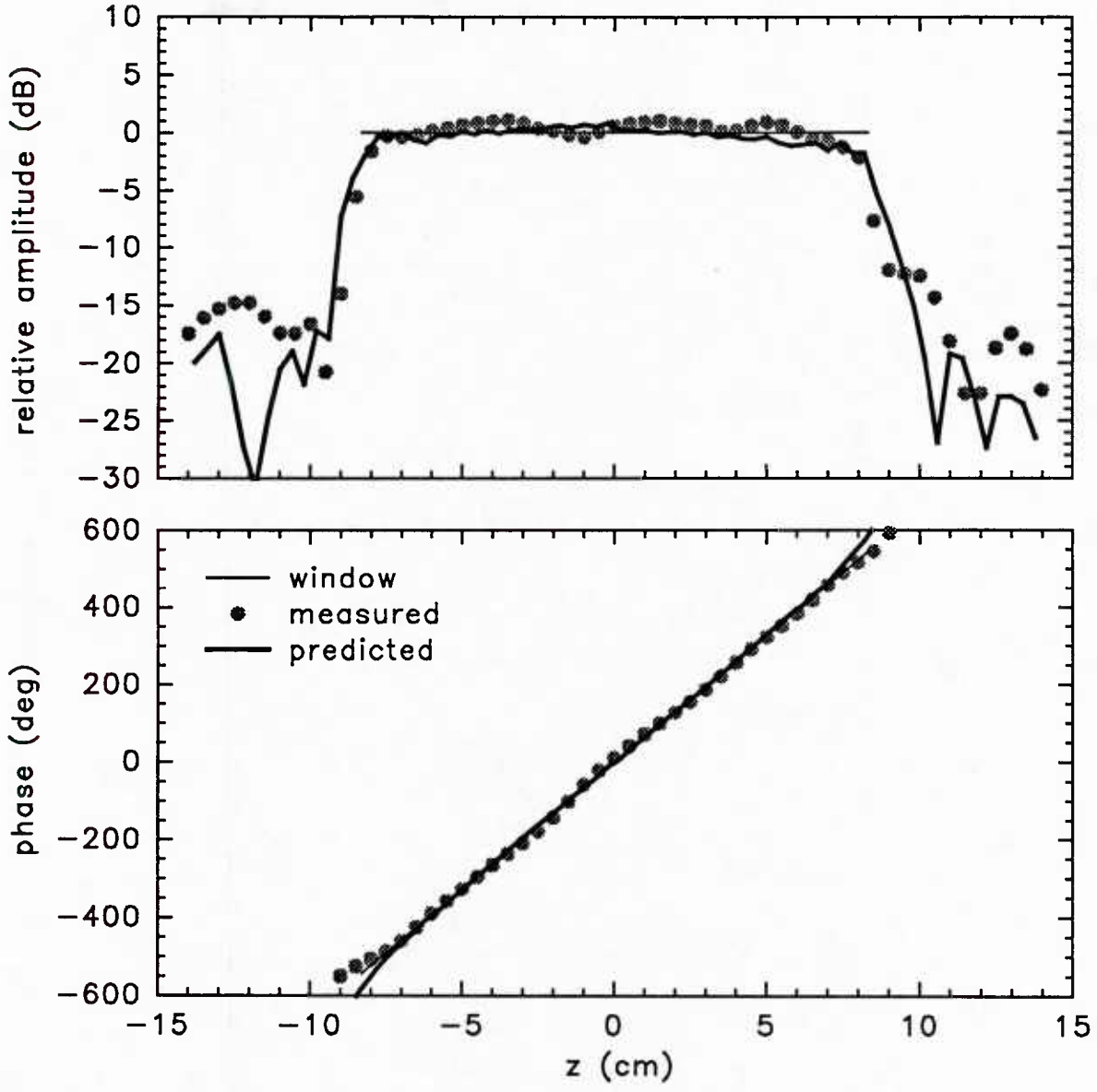

Fig. 58 — Pressures within the oil-backed CWC for a 88-m/s evanescent field at 1600 Hz in a window running from -8.3 to +8.3 cm using the measured transfer matrix.

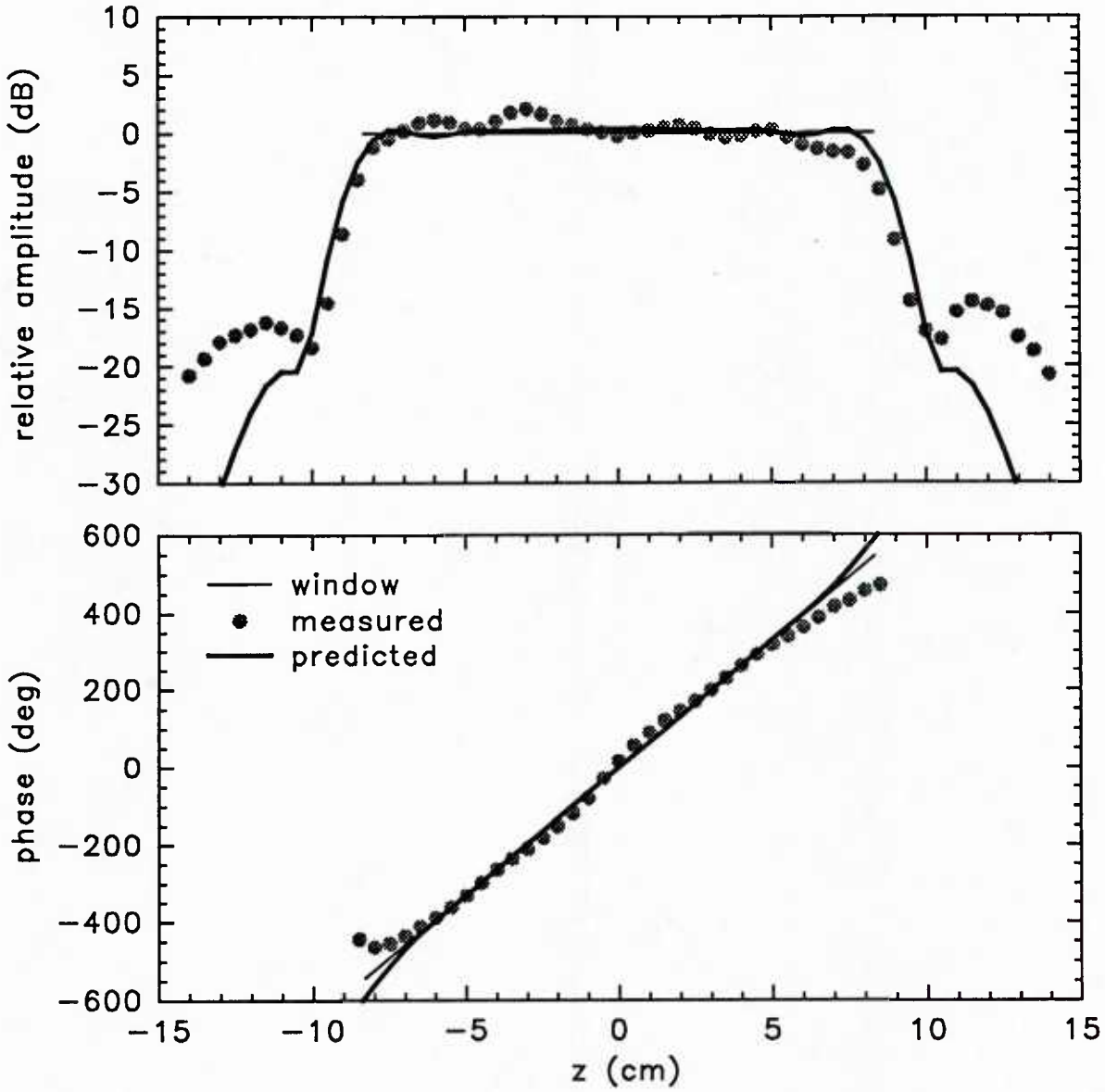

Fig. 59 — Pressures within the oil-backed CWC for a 88-m/s evanescent field at 1600 Hz in a window running from -8.3 to +8.3 cm using ATILA-CHIEF.

REFERENCES

1. W. A. Strawderman, "Wavevector-frequency analysis with applications to acoustics," NUSC Technical Document 8209, Naval Underwater Systems Center, New London, Connecticut, 1988.

2. D. H. Munro and K. U. Ingard, "On acoustic intensity measurement in the presence of mean flow," J. Acoust. Soc. Am. **65**, 1402-1406 (1979).

3. G. C. Lauchle, "Effect of turbulent boundary layer flow on measurement of acoustic pressure and intensity," Noise Control Engineering Journal, Sep.-Oct., 52-59, (1984).

4. D. M. Chase, "Modeling the wavevector-frequency spectrum of turbulent boundary layer pressure," J. Sound Vib. **70**, 29-67 (1980).

5. G. M. Corcos, "Resolution of pressure in turbulence," J. Acoust. Soc. Am. **35**, 192-199 (1963).

6. R. B. Gilchrist and W. A. Strawderman, "Experimental hydrophone-size correction factor for boundary-layer pressure fluctuations," J. Acoust. Soc. Am. **38**, 298-302 (1965).

7. H. S. Heaps, "Effect of turbulence nearfield on a shielded transducer," J. Acoust. Soc. Am. **40**, 1331-1336 (1966).

8. K. L. Chandiramani, "Vibrational response of fluid-loaded structures to low-speed flow noise," J. Acoust. Soc. Am. **61**, 1460-1470 (1977).

9. K. L. Chandiramani, "Response of underwater structures to convective component of flow noise," J. Acoust. Soc. Am. **73**, 835-839 (1983).

10. L. M. Brekhovskikh, *Waves in Layered Media* (Academic, New York, 1960).

11. G. Maidanik and D. W. Jorgensen, "Boundary wave-vector filters for the study of the pressure field in a turbulent boundary layer," J. Acoust. Soc. Am. **42**, 494-501 (1967).

12. W. K. Blake, "Turbulent boundary-layer wall-pressure fluctuations on smooth and rough walls," J. Fluid Mech. **44**, 637-660 (1970).

13. W. K. Blake and D. M. Chase, "Wavenumber-frequency spectra of turbulent-boundary-layer pressure measured by microphone arrays," J. Acoust. Soc. Am. **49**, 862-877 (1971).

14. J. M. Powers and C. H. Sherman, "Wavenumber calibration techniques for hydrophones — status report," NUSC-TM-811050 Naval Underwater Systems Center, New London, Connecticut, 1981.

15. H. C. Schau, L. D. Luker, S. Petrie, and A. L. Van Buren, "An evanescent wave array for wavenumber calibration," J. Acoust. Soc. Am. **80**, Suppl. 1, S27, (1986).

16. H. C. Schau, L. D. Luker and S. Petrie, "An array to produce convected normal velocity and pressure fields for wavenumber calibration and boundary layer modification," J. Acoust. Soc. Am. **82**, Suppl. 1, S2, (1987).

17. R. Ting, "Evaluation of new piezoelectric composite materials for hydrophone applications," Ferroelectrics **67**, 143-157 (1986).

18. I. A. Victorov, *Rayleigh and Lamb Waves* (Plenum, New York, 1979).

19. D. H. Trivett, L. D. Luker, S. Petrie, A. L. Van Buren, and Joseph E. Blue, "A planar array for the generation of evanescent waves," J. Acoust. Soc. Am. **87**, 2535-2540 (1990).

20. G. M. Sessler, "Piezoelectricity in polyvinylidene fluoride," J. Acoust. Soc. Am. **70**, 1596-1608 (1981).

21. H. Stefanou and S. Chen, "Piezoelectric PVDF polymers for underwater applications," ONR Contract No. N00014-80-C-0770, Pennwalt Corporation, King of Prussia, PA. (1982).

22. G. W. Benthien, D. Barach and D. Gillette, "CHIEF Users Manual," Naval Ocean System Center — Technical Document 970, Revision 1, (1988).

23. ATILA — Finite-Element Code for Piezoelectric and Magnetostrictive Transducer Modeling (Laboratoire d'Acoustique, Institut Supérior d'Electronique du Nord, Lille CEDEX, France, 1991).

24. A. D. Pierce, *ACOUSTICS, An Introduction to Its Physical Principles and Applications* (McGraw-Hill, New York, 1980), p. 27.

25. W. F. Hughes and E. W. Gaylord, *Basic Equations of Engineering Science* (McGraw-Hill, New York, 1964), p. 147.

26. P. M. Morse and H. Feshback, *Methods of Theoretical Physics* (McGraw-Hill, New York, 1953), pp. 1360-1376.

27. Reference 24, p. 15.

28. P. M. Morse and K. U. Ingard, *Theoretical Acoustics* (Princeton University Press, Princeton, New Jersey, 1968), p. 265.

29. G. Arfken, *Mathematical Methods for Physicists* (Academic Press, New York, 1970), pp. 413-415.

30. M. Abramowitz and I. A. Stegun, *Handbook of Mathematical Functions* (Dover, New York, 1970), pp. 374-375.

31. P. M. Morse, *Vibration and Sound* (McGraw-Hill, New York, 1948), pp. 246-248.

32. W. J. Thomson, "Transmission of pressure waves in liquid filled tubes," Proceedings of the First National Congress of Applied Mechanics, ASME, New York, NY, 927-933 (1953).

33. M. C. Junger, "The effect of a surrounding fluid on pressure waves in a fluid-filled elastic tube," J. Appl. Mech., **22**, 227-231 (1955).

34. L. D. Luker, J. F. Zalesak, C. K. Brown, and R. E. Scott, Jr., "Automated digital benchtop calibration system for hydrophone arrays," J. Acoust. Soc. Am. **73**, 1212-1216 (1983).

35. L. W. Johnson and R. D. Riess, *Numerical Analysis*, 2nd ed. (Addison-Wesley, New York, 1982), pp. 71-73.

36. J. B. Scarborough, *Numerical Mathematical Analysis*, 6th ed. (Johns Hopkins, Baltimore, MD, 1966), pp. 533-545.

37. A. L. Van Buren, "Steered planar calibration array," J. Acoust. Soc. Am. **63**, 1052-1059 (1978).

38. J. R. Mautz and R. F. Harrington, "Computational methods for antenna synthesis," IEEE Trans. Antennas Propag. **AP-23**, 507-512 (1975).

39. H. Schenck, "Improved integral formulation for acoustic radiation problems," J. Acoust. Soc. Am. **44**, 41-58 (1968).

40. G. W. Benthien, D. Barach and D. Gillette, "CHIEF Users Manual," Naval Ocean System Center Technical Document 970, Revision 1, Naval Ocean Systems Center, San Diego, CA (1988).

41. B. B. Baker and E. T. Copson, *The Mathematical Theory of Huygen's Principle* (The Clarendon Press, Oxford, England, 1950).

42. L. G. Copley, "Integral equation method for radiation from vibrating bodies," J. Acoust. Soc. Am. **41**, 807-816 (1967).

43. A. L. Van Buren, "A test of the capabilities of CHIEF in the numerical calculation of acoustic radiation from arbitrary surfaces," NRL Report 7160 (1970).

44. L. G. Copley, "Fundamental results concerning integral representations in acoustic radiation," J. Acoust. Soc. Am. **44**, 28-32 (1968).

45. P. Businger and G. H. Golub, "Linear least squares solutions by Householder transformations," Nomer. Math. **7**, 269-279 (1965).

46. Reference 22, p. A6-1.

47. C. M. Siders and R. A. Raymond, "CHIEF Preprocessor," NRL Memorandum Report No. 6536, (1989).

48. W. Thompson, Jr., "Modifications of Program CHIEF to Compute Sound Radiation from an Arbitrary Body with Mixed Boundary Conditions," Pennsylvania State University Applied Research Laboratory Technical Memorandum, File No. 90-375, State College, PA (1990).

49. W. Thompson, B. Dubus, and C. M. Siders, "Modifications of Programs CHIEF and CID to Compute Sound Radiation from an Arbitrary Body with Mixed Boundary Conditions," NRL Memorandum Report 6813, (1991).

50. R. D. Fay, R. L. Brown, and O. V. Fortier, "Measurement of acoustic impedances of surfaces in water," J. Acoust. Soc. Am. **19**, 850-856 (1947).

51. D. Stansfield, *Underwater Electroacoustic Transducers* (Bath University Press, Bath, U.K., 1991), p. 143.

52. Reference 51, p. 151.

53. Reference 24, p. 164.

54. Reference 22, p. A1-5.

55. L. Camp, *Underwater Acoustics* (John Wiley and Sons, New York, NY, 1970), p. 137.

56. O. B. Wilson, *An Introduction to the Theory and Design of Sonar Transducers* (U.S. Government Printing Office, Washington, D.C., 1985), p. 52.

57. Reference 56, p. 92.

58. Reference 23, ATILA_Analysis, p. 17.

59. H. A. Schenck and G. W. Benthien, "Numerical solution of acoustic-structure interaction problems," Naval Ocean System Center — Technical Report 1263 Naval Ocean Systems Center, San Diego, CA (1989), p. 3.

60. Reference 22, p. A1-5.

61. B. Hamonic, O. B. Wilson, S. R. Baker, "Coupling finite elements and Helmholtz equations for solving radiation and scattering problems," J. Acoust. Soc. Am. **84**, Suppl. 1, S220, (1988).

62. Reference 23, ATILA_Analysis, p. 27.

63. Reference 23, ATILA_Elements, p. 20.

64. Reference 23, ATILA_Elements, p. 50.

65. H. R. Gallantree, "Review of transducer applications of polyvinylidene fluoride," IEEE Proceedings **130**, Pt. 1, No. 5, 219-224 (1983).

66. C. K. Brown and M. T. McCord, "Wavenumber Calibrator Hardware Manual," USRD Technical Document No. 23, (1986).

67. R. E. Scott, Jr. and J. D. George, "A Microcomputer-Based Sampling Digital Voltmeter," NRL Memorandum Report No. 4872, (1983).

68. G. Goertzel, in *Mathematical Methods for Digital Computers*, edited by A. Ralston and H. S. Wilf (John Wiley and Sons, New York, NY, 1960), Vol I, Chap. 24, pp. 258-262.

69. Mathcad User's Guide, Version 3.1 (MathSoft Inc., Cambridge, MA, 1992)

70. K. M. Rittenmyer and P. S. Dubbelday, "Direct measurement of the temperature-dependent piezoelectric coefficients of composite materials by laser Doppler vibrometry," J. Acoust. Soc. Am. **91**, Pt. 1, 2254-2260 (1992).

71. L. E. Drain, *The Laser Doppler Technique* (John Wiley and Sons, New York, NY, 1980).

72. M. Redwood, *Mechanical Waveguides* (Pergamon Press, New York, 1960), p. 71.

73. Reference 72, pp. 10-14.

74. Reference 25, p. 57.

75. Reference 25, p. 62.

76. Symbolic Manipulation Program (SMP) (Inference Corporation, Los Angeles, CA, 1983)

77. Reference 30, p. 358.

78. W. H. Press, B. P. Flannery, S. A. Teukolsky, and W. T. Vetterling, *Numerical Recipes* (Cambridge University Press, New York, 1986), p. 176.

79. A. L. Van Buren, "A test of the capabilities of CHIEF in the numerical calculation of acoustic radiation from arbitrary surfaces," NRL Report 7160 (1970).

80. Reference 22, p. A3-1.

APPENDIX A

PROPAGATION SPEED WITHIN AN ELASTIC TUBE

To determine the predicted propagation within the PVDF CWC prototype, a study of the propagation speed in the fluid within an infinite-length elastic tube surrounded by another fluid was undertaken. Figure A1 shows a cross-section view of the tube and the fluid regions. Region I is filled with a fluid with density ρ_i and sound speed c_i. Region II consists of an elastic tube with density ρ_t, dilatational

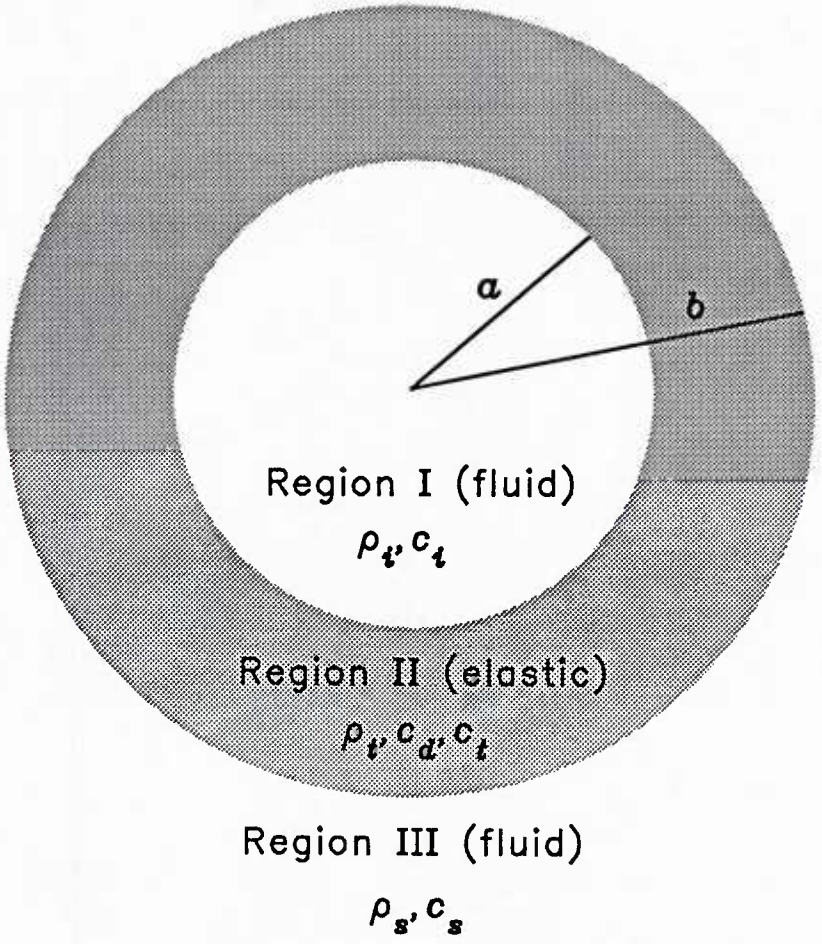

Fig. A1 — Infinite-length, cylindrical, fluid-elastic-fluid arrangement.

propagation speed c_d, and transverse propagation speed c_t. Region III is the fluid outside the tube extending to infinity with density ρ_s and sound speed c_s.

General Solutions

Region I

The fluid in region I can be described by the displacement potential function Φ_I with [72]

$$\nabla^2 \Phi_I = \frac{1}{c_i^2} \frac{\partial^2 \Phi_I}{\partial t^2} . \tag{A1}$$

Assuming radial symmetry in cylindrical coordinates (r,θ,z), and $\exp(i\omega t)$ time dependence, Eq. (A1) becomes

$$\frac{1}{r} \frac{\partial}{\partial r}\left(r \frac{\partial \Phi_I}{\partial r} \right) + \frac{\partial^2 \Phi_I}{\partial z^2} + k_i^2 \Phi_I = 0 , \tag{A2}$$

where $| k_i | = \omega / c_i$. The radial and axial displacements and pressure in region I are related to the potential function by

$$u_{ir} = \frac{\partial \Phi_I}{\partial r} , \tag{A3}$$

$$u_{iz} = \frac{\partial \Phi_I}{\partial z} , \tag{A4}$$

$$p_i = -\rho_i \frac{\partial^2 \Phi_I}{\partial^2 t} . \tag{A5}$$

Separating Φ_I into the product of a function of r only $R_I(r)$ and a function of z only $Z_I(z)$, one has

$$\frac{\partial^2 R_I}{\partial r^2} + \frac{1}{r} \frac{\partial R_I}{\partial r} + k_{ir}^2 R_I = 0 \tag{A6}$$

and

$$\frac{\partial^2 Z_I}{\partial z^2} + k_z^2 Z_I = 0 , \tag{A7}$$

where k_{ir} and k_z are the r and z components of k_i. Equation (A6) has the solution

$$R_I(r) = A_I J_0(k_{ir} r) + B_I Y_0(k_{ir} r) , \tag{A8}$$

where A_I and B_I are arbitrary constants. Requiring that the solution be finite at $r = 0$ forces B_I to equal zero. Therefore,

$$R_I(r) = A_I J_0(k_{ir} r) . \tag{A9}$$

Equation (A7) has the solution

$$Z_I(z) = C_I \exp(-ik_z z) . \tag{A10}$$

The solution for Φ_I can then be written as

$$\Phi_I = A\, J_0(k_{ir} r) \exp[i(\omega t - k_z z)] , \tag{A11}$$

where A is an arbitrary constant combining A_I and C_I.

Region II

The elastic solid in region II can be described [73] by the scalar potential Φ_{II} and the vector potential Ψ. Assuming axial symmetry, the radial and axial displacements in region II are related to these potential functions by

$$u_r = \frac{\partial \Phi_{II}}{\partial r} - \frac{\partial W}{\partial z} \tag{A12}$$

and

$$u_z = \frac{\partial \Phi_{II}}{\partial z} + \frac{1}{r}\left[\frac{\partial (rW)}{\partial r}\right], \tag{A13}$$

where $W(r,z)$ is the azimuthal component of Ψ.

The potential functions Φ_{II} and W must be solutions to

$$\nabla^2 \Phi_{II} = \frac{1}{c_d^2} \frac{\partial^2 \Phi_{II}}{\partial t^2} \tag{A14}$$

and

$$\nabla^2 W - \frac{1}{r^2} W = \frac{1}{c_t^2} \frac{\partial^2 W}{\partial t^2} , \tag{A15}$$

respectively, where c_d is the dilatational wave speed and c_t is the shear wave speed in the elastic solid. Assuming solutions of Eqs. (A14) and (A15) in the form of waves traveling in the z direction, one has

$$\Phi_{II} = [CJ_0(k_{dr}r) + DY_0(k_{dr}r] \exp[i(\omega t - k_z z)] \tag{A16}$$

and

$$W = [FJ_1(k_{tr}r) + GY_1(k_{tr}r] \exp[i(\omega t - k_z z)] , \tag{A17}$$

where

$$k_{dr} = \sqrt{k_d^2 - k_z^2} \tag{A18}$$

and

$$k_{tr} = \sqrt{k_t^2 - k_z^2} . \tag{A19}$$

Region III

The fluid in region III can be described by the potential function Φ_{III}, which is identical with the function Φ_I for region I. Following the same procedure as in region I one arrives at the solution

$$R_{III}(r) = A_{III}J_0(k_{sr}r) + B_{III}Y_0(k_{sr}r) , \tag{A20}$$

where k_{sr} is the r components of k_s. Assuming an outgoing wave and combining constants gives

$$R_{III}(r) = BH_0^{(2)}(k_{sr}r) , \tag{A21}$$

where $H_0^{(2)}$ is a Hankel function of the second kind. The solution for region III can then be written as

$$\Phi_{III} = BH_0^{(2)}(k_{sr}r) \exp[i(\omega t - k_z z)] . \tag{A22}$$

Boundary Conditions

The boundary conditions relating the pressures, stresses, and displacements at the region boundaries are:

1. The negative of the pressure in region I must equal the normal stress in region II at $r = a$.
2. The normal component of the particle displacement in region I must equal the normal component of the surface displacement in region II at $r = a$.
3. The tangential stress in region II must be zero at $r = a$.
4. The tangential stress in region II must be zero at $r = b$.
5. The negative of the pressure in region III must equal the normal stress in region II at $r = b$.
6. The normal component of the particle displacement in region III must equal the normal component of the surface displacement in region II at $r = b$.

The following relationships for this axially-symmetric situation are useful for expressing these

boundary conditions mathematically.

The non-zero strains are [74]:

$$e_{rr} = \frac{\partial u_r}{\partial r} , \qquad e_{\theta\theta} = \frac{u_r}{r} , \qquad e_{zz} = \frac{\partial u_z}{\partial z} , \tag{A23}$$

$$e_{rz} = e_{zr} = \frac{1}{2}\left(\frac{\partial u_r}{\partial z} + \frac{\partial u_z}{\partial r}\right) , \tag{A24}$$

$$\Delta = e_{rr} + e_{\theta\theta} + e_{zz} , \tag{A25}$$

where Δ is the dilatation.

The stress-strain relationships are [75]:

$$\tau_{rr} = \lambda\Delta + 2\mu e_{rr} , \tag{A26}$$

$$\tau_{\theta\theta} = \lambda\Delta + 2\mu e_{\theta\theta} , \tag{A27}$$

$$\tau_{zz} = \lambda\Delta + 2\mu e_{zz} , \tag{A28}$$

$$\tau_{rz} = 2\mu e_{rz} , \tag{A29}$$

where λ and μ are Lamé's constants for the elastic material in region II related to c_d and c_t by

$$c_d^2 = \frac{\lambda + 2\mu}{\rho_t} , \qquad c_t^2 = \frac{\mu}{\rho_t} . \tag{A30}$$

The boundary conditions can then be expressed mathematically as:

B. C. # 1

$$\tau_{rr}\big|_{r=a} + p_i\big|_{r=a} = 0 , \tag{A31}$$

B. C. # 2

$$u_{ir}\big|_{r=a} - u_r\big|_{r=a} = 0 , \tag{A32}$$

B. C. # 3

$$\tau_{rz}\big|_{r=a} = 0 \ , \tag{A33}$$

B. C. # 4

$$\tau_{rz}\big|_{r=b} = 0 \ , \tag{A34}$$

B. C. # 5

$$\tau_{rr}\big|_{r=b} + p_s\big|_{r=b} = 0 \ , \tag{A35}$$

B. C. # 6

$$u_r\big|_{r=b} - u_{sr}\big|_{r=b} = 0 \ . \tag{A36}$$

Propagation Speeds

By inserting the appropriate items into the boundary condition equations, taking the required derivatives, and considerable algebraic manipulation (carried out with the aid of SMP [76]), one can arrive at the 6×6 coefficient matrix shown in Fig. A2. After expressing all the wavenumbers in terms of k_z, the values of k_z that make the determinant of the coefficient matrix equal to zero give the propagation speeds for the modes that are supported at that frequency. A FORTRAN computer program was written to evaluate the determinant and search for the zeros at each specified frequency. The program automatically switches from Bessel functions to the appropriate modified Bessel functions, whenever the function arguments become imaginary, using the relationships [77,78]:

$$H_n^{(2)}(x) = J_n(x) - iY_n(x) \ , \tag{A37}$$

$$J_0(ix) = I_0(x) \ , \tag{A38}$$

$$J_1(ix) = iI_1(x) \ , \tag{A39}$$

$$Y_0(ix) = -\frac{2}{\pi}K_0(x) + iI_0(x) \ , \tag{A40}$$

$$Y_1(ix) = i\frac{2}{\pi}K_1(x) - I_1(x) \ . \tag{A41}$$

A	C	D	$-iF$	$-iG$	B
$\frac{a\omega^2\rho_t J_0(k_{tr}a)}{\mu}$	$2k_{dr}J_1(k_{dr}a)$ $-aJ_0(k_{dr}a)\left[\frac{\lambda(k_{dr}^2+k_z^2)}{\mu}+2k_{dr}^2\right]$	$2k_{dr}Y_1(k_{dr}a)$ $-aY_0(k_{dr}a)\left[\frac{\lambda(k_{dr}^2+k_z^2)}{\mu}+2k_{dr}^2\right]$	$2\begin{bmatrix}k_zJ_1(k_{tr}a)\\-ak_{tr}J_0(k_{tr}a)\end{bmatrix}$	$2\begin{bmatrix}k_zY_1(k_{tr}a)\\-ak_{tr}Y_0(k_{tr}a)\end{bmatrix}$	0
$-k_{tr}J_1(k_{tr}a)$	$k_{dr}J_1(k_{dr}a)$	$k_{dr}Y_1(k_{dr}a)$	$k_zJ_1(k_{tr}a)$	$k_zY_1(k_{tr}a)$	0
0	$2k_{dr}k_zJ_1(k_{dr}a)$	$2k_{dr}k_zY_1(k_{dr}a)$	$-J_1(k_{tr}a)(k_{tr}^2-k_z^2)$	$-Y_1(k_{tr}a)(k_{tr}^2-k_z^2)$	0
0	$2k_{dr}k_zJ_1(k_{dr}b)$	$2k_{dr}k_zY_1(k_{dr}b)$	$-J_1(k_{tr}b)(k_{tr}^2-k_z^2)$	$-Y_1(k_{tr}b)(k_{tr}^2-k_z^2)$	0
0	$2k_{dr}J_1(k_{dr}b)$ $-bJ_0(k_{dr}b)\left[\frac{\lambda(k_{dr}^2+k_z^2)}{\mu}+2k_{dr}^2\right]$	$2k_{dr}Y_1(k_{dr}b)$ $-bY_0(k_{dr}b)\left[\frac{\lambda(k_{dr}^2+k_z^2)}{\mu}+2k_{dr}^2\right]$	$2\begin{bmatrix}k_zJ_1(k_{tr}b)\\-bk_{tr}J_0(k_{tr}b)\end{bmatrix}$	$2\begin{bmatrix}k_zY_1(k_{tr}b)\\-bk_{tr}Y_0(k_{tr}b)\end{bmatrix}$	$\frac{b\omega^2\rho_s H_0^{(2)}(k_{tr}b)}{\mu}$
0	$-k_{dr}J_1(k_{dr}b)$	$-k_{dr}Y_1(k_{dr}b)$	$-k_zJ_1(k_{tr}b)$	$-k_zY_1(k_{tr}b)$	$k_{sr}H_1^{(2)}(k_{sr}b)$

Fig. A2 — Coefficient matrix for the fluid-elastic-fluid problem.

APPENDIX B

CWCMDL PROGRAM

Description of the Program

A FORTRAN computer program called CWCMDL was written to calculate sets of electrical band drives that could be used to generate evanescent pressure fields within the CWC. The program computes the complex band drives using transfer matrices determined from either CHIEF-I, RING-CHIEF, or ATILA-CHIEF models of the CWC. The program can also compute the predicted pressure field within the CWC from a specified set of band drives.

```
Data for the CWC Modeling Program (CWCMDL)
CA0807A          !(CHR) Name of the run (run_name)
3                !(I) Function (1=calc drives, 2=map, 3=both) (oper_mode)
3                !(I) Model type (1=rigid,2=imped.,3=vel. file) (mod_type)
1                !(I) Printout level (prnt_lvl)
55, 92           !(R) Phase speeds of evanescent waves (m/s) (phas_spd)
1 2              !(I) Numbers of phase speeds to map (map_spd_num)
800              !(R) Frequency in (Hz) (freq)
1000             !(R) Density of fluid (kg/m3) (rho)
1485             !(R) Speed of sound in fluid (m/s) (snd_spd)
.0155            !(R) CWC inner radius (m) (r_inner)
.01625           !(R) CWC outer radius (m) (r_outer)
.006             !(R) Width of grounded band (m) (grn_bnd_wid)
.006             !(R) Width of active band (m) (act_bnd_wid)
40               !(I) Number of active bands (num_bnds)
allbands         !(CHR) File containing the driven band numbers (bnd_file)
70               !(I) Number of points for the transfer matrix (num_pts)
-.138            !(R) Minimum z for transfer matrix points (m) (min_zp)
 .138            !(R) Maximum z for transfer matrix points (m) (max_zp)
.1               !(R) Percent average added to matrix diagonals (alpha)
-.085            !(R) Minimum z for window (m) (min_zc)
.085             !(R) Maximum z for window (m) (max_zc)
0                !(R) x coordinate for map (m) (x_map)
0                !(R) y coordinate for map (m) (y_map)
-.135            !(R) Minimum z to map (m) (z_map_min)
 .005            !(R) Delta z for mapping (m) (z_map_delta)
 .135            !(R) Maximum z to map (m) (z_map_max)
CA0800.VEL       !(CHR) File containing the single-drive velocities (vel_file)
```

Fig. B1 — Sample parameter-input file for CWCMDL.

The parameters that CWCMDL uses in each run are contained in a text file. A sample of the input-parameter file is given in Fig. B1. The program reads the parameters from the input file and then performs the necessary computations.

Flow of Processing

The flow of processing in CWCMDL is:

1. Call the subroutine INPUT, which opens the input-parameter file and reads the parameters for the run.
2. Call the subroutine LOADBNDS, which reads the driven band numbers from the specified file. If the file name "allbands" is specified, no driven-band-number file is accessed and all the bands are used.
3. If calculation of drives is requested, call the subroutine CALCDRV, which:
   a. Calls either CHFSUB or CHZSUB to set up CHIEF and generate the CHIEF matrices. CHFSUB sets up CHIEF for the case where all the normal surface velocities are specified and CHZSUB sets up CHIEF for the case where interior-wall impedances are specified.
   b. Calculates the columns of the M matrix by utilizing CHIEF (with or without ATILA) to determine the pressure at each field point while each band is driven alone. If the RING-CHIEF or ATILA-CHIEF models are being used the resultant normal surface velocities for each surface when a single band is excited are read from the specified file. CALCDRV checks for and utilizes any symmetry of field points to reduce the number of unique columns that have to be calculated.
   c. Fills any remaining non-unique columns with the appropriate results from the unique columns.
   d. Calculates the desired pressures P. Multiple P vectors can be specified (e.g., different phase speeds and window widths) since solving for the multiple drives with back substitution requires very little additional computation.
   e. Call the subroutine DCXLSTSQ (Double-precision CompleX, LeaST SQuares) to collapse the m equations to n equations. The solution of the new system is the least-square solution of the original system.
   f. Calculates α as a percentage of the average value of the absolute amplitudes of the elements of the reduced matrix M' and adds it to the diagonal elements.
   g. Perform lower-upper decomposition on M'.
   h. Obtains each set of drives by inserting the appropriate desired pressures and using back-substitution.
   i. Writes the resulting drive levels to files.
4. If maps of the predicted pressure fields are requested, calls the subroutine MAPFLDS to map the resultant pressure fields as follows:
   a. If necessary sets up CHIEF by calling CHFSUB.
   b. For each set of drives to be mapped:
      i. Calls LOADDRV, which loads the drives from a specified file. If the RING-CHIEF or ATILA-CHIEF models are specified, the normal surface velocities are computed by adding the complex contributions to each surface as each band is excited with the specified drive.
      ii. Computes the pressure at each position to be mapped by calling the subroutine CHFNFP.
      iii. Writes the map of the pressure field to a file.

FORTRAN Code

Listings of the more significant routines used by CWCMDL follow:

CWCMDL.FOR (Main program)

```
      program CWCMDL

c  This program models the Cylindrical Wavenumber Calibrator (CWC).
```

```
c  It also calculates the band drives required to produce an
c  evanescent field inside the CWC.

c  L. D. Luker, NRL/USRD, 24-SEP-1990.  Last modified on 9-MAY-1992.

      implicit none

      include 'CWCMDL.INC/list'

      character*3 symtyp
      character*4 fldtyp
      integer*4 i, j, nblks

c  Open the main input file

      open(unit = inp_un, file = inp_file, status = 'OLD')

c  Input the run parameters
      call input(1, 45)
      close (unit = inp_un)

c  If desired, read the driven band numbers and calc. and save drives
      if ((oper_mode .eq. 1) .or. (oper_mode .eq. 3)) then
        call loadbnds
        call calcdrv
      end if

c  If desired, map the pressure fields
      if ((oper_mode .eq. 2) .or. (oper_mode .eq. 3)) then
        call mapflds
      end if

c  All done.
      close (unit = out_un)

      end
```

CWCMDL.INC (Included file)

```
c  This file (CWCMDL.INC) is included in all of the Cylindrical
c  Wavenumber Calibrator (CWC) routines to declare common variables.

c  L. D. Luker, NRL/USRD, 24-SEP-1990.  Last modified on 12-DEC-1992.

      character
     1  date_time*20,   !Date and time
     1  run_name*15     !Name of the run

      character*20
     1  inp_file,       !File containing the main input data
     1  out_file,       !File containing the main output data
     1  bnd_file,       !File containing the numbers of driven bands
     1  drv_file,       !File containing the band drives
     1  vel_file,       !File containing the single drive velocities
     1  map_file        !File containing the pressure map

      parameter (inp_file = 'CWCMDL.INP')

      integer*4
     1  inp_un,         !Unit number for main input file
     1  out_un,         !Unit number for main output file
     1  bnd_un,         !Unit number for driven band file
     1  drv_un,         !Unit number for band drives
```

```
      1  vel_un,          !Unit number for single drive vel. file
      1  map_un,          !Unit number for map output
      1  out_len          !Record length for main output

      parameter (inp_un = 1)
      parameter (bnd_un = 2)
      parameter (drv_un = 3)
      parameter (vel_un = 4)
      parameter (map_un = 8)
      parameter (out_un = 9)
      parameter (out_len = 1024)

      integer*4
      1  max_bnds,        !Maximum number of bands
      1  max_pnts,        !Maximum number of field points or map points
      1  max_spds         !Maximum phase speeds

      parameter (max_bnds=50, max_pnts=151, max_spds=9)

      integer*4
      1  oper_mode,       !Operating mode (1=calc drvs,2=map,3=both)
      1  prnt_lvl,        !Printout level
      1  num_bnds,        !Number of bands
      1  num_drv_bnds,    !Number of driven bands
      1  num_pnts,        !Number of random points for transfer matrix
      1  num_spds,        !Number of evanescent phase speeds
      1  num_map_spds,    !Number of evanescent phase speeds to map
      1  drv_bnd(max_bnds),    !Array containing numbers of driven bands
      1  map_spd_num(max_spds), !Numbers of phase speeds to map
      1  mod_type         !Model type:
c                             1 -> Rigid tube
c                             2 -> Interior impedance
c                             3 -> CHIEF & ATILA
c
      real*4
      1  pi,                    !Good old pi
      1  rp,                    !r coordinate of matrix point
      1  zp,                    !z coordinate of matrix point
      1  z_bnd(max_bnds),       !z coordinate of band edges
      1  max_drv_amp            !Maximum normalized drive amplitude

      real*4
      1  freq,            !Frequency
      1  rho,             !Density of fluid
      1  snd_spd,         !Speed of sound in fluid
      1  phas_spd(max_spds),   !Phase speed of evanescent wave
      1  r_inner,         !Inner radius of array
      1  r_outer,         !Outer radius of array
      1  gnd_bnd_wid,     !Width of grounded band
      1  act_bnd_wid,     !Width of active band
      1  z_arr_min,       !Minimum z coordinate of array
      1  z_arr_max,       !Maximum z coordinate of array
      1  z_bnds_min,      !Minimum z coordinate of driven bands
      1  z_bnds_max,      !Maximum z coordinate of driven bands
      1  min_zp,          !Minimum point region z coordinate
      1  max_zp,          !Maximum point region z coordinate
      1  alpha,           !Value added to matrix diagonals to force sol.
      1  min_zc(max_spds),     !Minimum control region z coordinate
      1  max_zc(max_spds)      !Maximum control region z coordinate

      real*4
      1  x_map,           !x coordinate to map
      1  y_map,           !y coordinate to map
      1  z_map_min,             !Minimum z to map
      1  z_map_delta,           !Delta z for mapping
      1  z_map_max              !Maximum z to map
```

```
      complex*16
     1  wall_imp,              !CWC inner-wall impedance
     1  drive(max_bnds)

      parameter (pi=3.1415927)

      common /cwccom/
     1  date_time, run_name,
     1  bnd_file, drv_file, vel_file, map_file,
     1  oper_mode, prnt_lvl,
     1  num_bnds, num_drv_bnds, num_pnts, num_spds, num_map_spds,
     1  map_spd_num, drv_bnd, mod_type, rp, zp,
     1  z_bnd, max_drv_amp,
     1  freq, rho, snd_spd, phas_spd,
     1  r_inner, r_outer,
     1  gnd_bnd_wid, act_bnd_wid,
     1  z_arr_min, z_arr_max,
     1  z_bnds_min, z_bnds_max,
     1  min_zp, max_zp, min_zc, max_zc,
     1  alpha, x_map, y_map,
     1  z_map_min, z_map_delta, z_map_max, wall_imp, drive

c  CHIEF section

      integer*4
     1  mxars,          !Max surface subdivisions in sym. block
     1  mxnfp           !Max number of nearfield points

      parameter (mxars = 86, mxnfp = max_pnts)

      integer*4
     1  numfpn,         !Number of field points
     1  infnrm,         !Field point to normalize to
     1  mdsize

      parameter (mdsize = mxars * max(mxars, mxnfp))

      real*4
     1  rmnnrm,
     1  nfpxs(3, mxnfp),      !Nearfield point coordinates
     1  pnrmnf(mxnfp)

      complex*8
     1  vel(mxars),           !Surface velocities
     1  sp(mxars),            !Surface pressures
     1  nfp(mxnfp),           !Nearfield pressures
     1  pmatx(mdsize),        ! Pressure matrix for CHIEF
     1  vmatx(mdsize)         ! Velocity matrix for CHIEF

      common /nfinp/ numfpn, nfpxs
      common /velsps/ vel, sp
      common /nfvals/ nfp, pnrmnf, infnrm, rmnnrm
      common /chfc1/ pmatx, vmatx
```

INPUT.FOR (Reads parameters from the input file)

```
      subroutine input(inp_col, out_col)

c  This subroutine reads the input data from unit "inp_un" starting
c  at "inp_col" and writes the data to the unit "out_un" starting
c  at "out_col" preceeded by the data description.

c  L. D. Luker, NRL/USRD, 26-SEP-1990.  Last modified on 12-DEC-1992.
```

```
      implicit none

      include 'CWCMDL.INC/list'

      character dummy*78
      integer*4 data_mode, inp_col, out_col, vals
      logical ask

      data_mode = 1
      ask = .true.
      read(inp_un, '(a)') dummy

      call getchr(data_mode, ask, inp_un, inp_col, -1, out_col,
     1    'Name of the run', run_name)

      open(unit = out_un, file = run_name // '.OUT',
     1    recl = out_len, status = 'NEW')

      date_time = ' '
      call date(date_time(1:9))
      call time(date_time(12:20))
      write(out_un, '(x,''"CWC Modeling Program ('',
     1     a,'') Run Name: '',a/)') date_time(1:19), run_name
d     write(out_un, '(x,''"'',a,/)') dummy

      map_file = run_name
      drv_file = run_name

      call geti(data_mode, ask, inp_un, inp_col, out_un, out_col, 1,
     1    '"Operating mode (1=calc,2=map,3=both)', oper_mode, vals)

      call geti(data_mode, ask, inp_un, inp_col, out_un, out_col, 1,
     1    '"Model type (1=rigid, 2=imped., 2=vel.)', mod_type, vals)

      call geti(data_mode, ask, inp_un, inp_col, out_un, out_col, 1,
     1    '"Printout level', prnt_lvl, vals)

      call getr(data_mode, ask, inp_un, inp_col, out_un,
     1    out_col, max_spds,
     1    '"Phase speeds of evanescent waves (m/s)', phas_spd,
     1    num_spds)

      call geti(data_mode, ask, inp_un, inp_col, out_un,
     1    out_col, max_spds,
     1    '"Numbers of phase speeds to map', map_spd_num,
     1    num_map_spds)

      call getr(data_mode, ask, inp_un, inp_col, out_un, out_col, 1,
     1    '"Frequency (Hz)', freq, vals)

      call getr(data_mode, ask, inp_un, inp_col, out_un, out_col, 1,
     1    '"Density of fluid (kg/m3)', rho, vals)

      call getr(data_mode, ask, inp_un, inp_col, out_un, out_col, 1,
     1    '"Sound speed in fluid (m/s))', snd_spd, vals)

      call getr(data_mode, ask, inp_un, inp_col, out_un, out_col, 1,
     1    '"CWC inner radius (m)', r_inner, vals)

      call getr(data_mode, ask, inp_un, inp_col, out_un, out_col, 1,
     1    '"CWC outer radius (m)', r_outer, vals)

      call getr(data_mode, ask, inp_un, inp_col, out_un, out_col, 1,
     1    '"Width of grounded band (m)', gnd_bnd_wid, vals)

      call getr(data_mode, ask, inp_un, inp_col, out_un, out_col, 1,
```

```
     1    '"Width of active band (m)', act_bnd_wid, vals)

     call geti(data_mode, ask, inp_un, inp_col, out_un, out_col, 1,
     1    '"Number of active bands', num_bnds, vals)

     call getchr(data_mode, ask, inp_un, inp_col, out_un, out_col,
     1    '"File containing driven bands', bnd_file)
     if (bnd_file(1:1) .eq. '.') bnd_file = run_name // bnd_file

     call geti(data_mode, ask, inp_un, inp_col, out_un, out_col, 1,
     1    '"Number of points for transfer matrix', num_pnts, vals)

     call getr(data_mode, ask, inp_un, inp_col, out_un, out_col, 1,
     1    '"Minimum z for matrix points (m)', min_zp, vals)

     call getr(data_mode, ask, inp_un, inp_col, out_un, out_col, 1,
     1    '"Maximum z for matrix points (m)', max_zp, vals)

     call getr(data_mode, ask, inp_un, inp_col, out_un, out_col, 1,
     1    '"% average added to matrix diagonals', alpha, vals)

     call getr(data_mode, ask, inp_un, inp_col, out_un,
     1    out_col, max_spds,
     1    '"Minimum z for controlled region (m)', min_zc, vals)

     call getr(data_mode, ask, inp_un, inp_col, out_un,
     1    out_col, max_spds,
     1    '"Maximum z for controlled region (m)', max_zc, vals)

     call getr(data_mode, ask, inp_un, inp_col, out_un, out_col, 1,
     1    '"x coordinate for map (m)', x_map, vals)

     call getr(data_mode, ask, inp_un, inp_col, out_un, out_col, 1,
     1    '"y coordinate for map (m)', y_map, vals)

     call getr(data_mode, ask, inp_un, inp_col, out_un, out_col, 1,
     1    '"Minimum z to map (m)', z_map_min, vals)

     call getr(data_mode, ask, inp_un, inp_col, out_un, out_col, 1,
     1    '"Delta z for mapping', z_map_delta, vals)

     call getr(data_mode, ask, inp_un, inp_col, out_un, out_col, 1,
     1    '"Maximum z to map (m)', z_map_max, vals)

     call getchr(data_mode, ask, inp_un, inp_col, out_un, out_col,
     1    '"File containing single drive vel.', vel_file)

     z_bnds_max = (num_bnds * act_bnd_wid) / 2.
     z_bnds_min = - z_bnds_max
     z_arr_max = z_bnds_max + gnd_bnd_wid
     z_arr_min = - z_arr_max
     wall_imp = cmplx(0.0, -4.0e9 * 0.497 / freq)

     return

     end
```

CALCDRV.FOR (Calculates band drives)

```
     subroutine calcdrv

c  This subroutine calculates the band drive required for the CWC.
c  This is accomplished by constructing the set of simultaneous eqns:
```

```
c                              M X = Y                                  (1)
c                              = -   -
c  where (for each equation) the values for the elements in M and Y are
c  calculated for a point in the region where the desired sound field is
c  to be created.  This gives m equations with n unknowns (m greater
c  than or equal to n) where n is the number of driven bands in the CWC.

c  This set of equations is then collapsed to form the new set of eqns:

c                              M' X = Y'                                (2)
c                              =  -   -
c  consisting of n equations with n unknowns.  Equation 2 is arrived at
c  by multiplying both sides of Eq. 1 by the conjugate transpose of M.
c  Equation 2 is then solved to yield the required drive values X.
c  The solution to Eq. 2 is the least-squares solution to Eq. 1.

c  L. D. Luker, NRL/USRD, 25-OCT-1990.  Last modified on 17-JUL-1992.

      implicit none

      include 'CWCMDL.INC/list'

      character name*30

      integer*4 i, j, bnd,
     1  uniq_col,                    !Number of unique columns in M
     1  rows_used,                   !Total rows used (some zeros)
     1  perm_vec(max_bnds)           !Permutation vector for dcxludc

      real*4 angle, beta, del_zp, col_max, mat_max

      real*8 work_vec(max_bnds)      !Working vector for dcxludc

      complex*16
     1  M_mat(max_pnts,max_bnds),    !Transfer matrix.
     1  M_star(max_bnds,max_pnts),   !Conjugate transpose of M_mat
     1  M_prime(max_bnds,max_bnds),        !Collapsed matrix.
     1  Y_mat(max_pnts,max_spds),    !Right-hand-side of the equation.
     1  Y_prime(max_bnds,max_spds),        !Collapsed right-hand-side.
     1  det

d     write(out_un, '(/,'' <CALCDRV> Entered.'',/)')

c  Set up CHIEF and generate the matrices
      if (mod_type .eq. 2) then
        call chzsub
      else
        call chfsub
      endif

      numfpn = num_pnts
      del_zp = (max_zp - min_zp) / (num_pnts - 1)

c  Load the point coordinates
      do 50 i = 1, num_pnts
        nfpxs(1, i) = 0.
        nfpxs(2, i) = 0.
        nfpxs(3, i) = min_zp + (i - 1) * del_zp
d       write(out_un, '('' nfpxs(3,'', i3, '') ='', f8.4)')
d     1   i, nfpxs(3,i)
50    continue

d     if (prnt_lvl .eq. 4) then
d       open(unit = 1, file = 'CWCMDL.TMP',
d     1   recl = out_len, status = 'OLD')
d       call dcxin(M_mat, name, max_pnts, num_pnts,
```

```
d     1   num_drv_bnds, 1, out_len, 34 + num_pnts)
d       close(unit = 1)
d       goto 200
d     endif

c  Fill the M matrix
c    Determine the number of unique columns
       if (min_zp .eq. -max_zp) then !Can use symmetry
         uniq_col = (num_drv_bnds + 1) / 2
       else                        !Can't use symmetry
         uniq_col = num_drv_bnds
       endif

c    For each unique column
       mat_max = 0.
       do 100 i = 1, uniq_col
         call fillcol(i, M_mat, col_max)
         mat_max = max(mat_max, col_max)
100    continue

c    Fill any remaining columns
       do 150 i = uniq_col + 1, num_drv_bnds
         do 150 j = 1, num_pnts
           M_mat(j,i) = M_mat(num_pnts + 1 - j, num_drv_bnds + 1 - i)
150    continue

c  Write the transposed M matrix as real and imaginary
d      open(unit = 1, file = run_name // '.RE',
d      1 recl = out_len, status = 'NEW')
d      do 160 i = 1, num_drv_bnds
d        write(1,'(85(x,1pe11.4))')
d      1       (dreal(M_mat(j,i)), j=1,num_pnts)
160    continue
d      close(unit=1)
d      open(unit = 1, file = run_name // '.IM',
d      1 recl = out_len, status = 'NEW')
d      do 170 i = 1, num_drv_bnds
d        write(1,'(85(x,1pe11.4))')
d      1       (dimag(M_mat(j,i)), j=1,num_pnts)
170    continue
d      close(unit=1)

c  Calculate the right-hand sides
       do 200 j = 1, num_spds
         if ((max_zc(j) - min_zc(j)) .eq. 0.) then
           min_zc(j) = min_zc(j - 1)
           max_zc(j) = max_zc(j - 1)
         endif
         do 200 i = 1, num_pnts
           if ((nfpxs(3,i) .ge. (min_zc(j) - .0001))
       1     .and. (nfpxs(3,i) .le. (max_zc(j) + .0001))) then
             angle = ((2. * pi * freq) / phas_spd(j)) * nfpxs(3, i)
d            type *, i, j, phas_spd(j), nfpxs(3,i), angle
             Y_mat(i,j) = cmplx(cos(angle),sin(angle))
           else
             Y_mat(i,j) = cmplx(0.0,0.0)
           endif
200    continue

       rows_used = num_pnts

c  Collapse the equations for the least-square solution.
       call dcxlstsq(M_mat, max_pnts,
       1             Y_mat, max_pnts,
       1             M_prime, max_bnds,
       1             Y_prime, max_bnds,
```

```
     1              M_star, max_bnds,
     1              rows_used, num_drv_bnds, num_spds)
*    1              num_pnts, num_drv_bnds, num_spds)

d    call dcxout(M_mat, '<CALCDRV> M  '//name,
d    1  max_pnts, rows_used, num_drv_bnds, out_un, out_len)
*    1  max_pnts, num_pnts, num_drv_bnds, out_un, out_len)

d    call dcxout(Y_mat, '<CALCDRV> Y',
d    1  max_pnts, rows_used, num_spds, out_un, out_len)
*    1  max_pnts, num_pnts, num_spds, out_un, out_len)

d    call dcxout(M_prime, '<CALCDRV> M'',
d    1  max_bnds, num_drv_bnds, num_drv_bnds, out_un, out_len)

c  Calculate beta as alpha percent of the average |M'| value.
     if (alpha .ne. 0.0) then
       beta = 0.0
       do 300 i = 1, num_drv_bnds
         do 300 j = 1, num_drv_bnds
           beta = beta + abs(M_prime(j,i))
300    continue
       beta = alpha * beta / (100. * num_drv_bnds ** 2)

c  Add beta to the diagonal elements of M'.
       do 400 i = 1, num_drv_bnds
         M_prime(i,i) = M_prime(i,i) + beta
400    continue
     write(out_un, '(/,'' "beta = '',1pg11.4/)') beta
     endif

d    call dcxout(M_prime, '<CALCDRV> M'' + beta',
d    1  max_bnds, num_drv_bnds, num_drv_bnds, out_un, out_len)

d    call dcxout(Y_prime, '<CALCDRV> Y'',
d    1  max_bnds, num_drv_bnds, num_spds, out_un, out_len)

c  Calculate the drives using LU decomposition
     call dcxludc(M_prime, max_bnds,
     1            num_drv_bnds, work_vec, perm_vec, det)

c  For each phase speed
     do 600 j = 1, num_spds

c    Load the RHS vector
       do 500 i = 1, num_drv_bnds
         drive(i) = Y_prime(i,j)
500    continue

c    Solve for the drives with back-substitution
       call dcxlubk(M_prime, max_bnds,
     1            num_drv_bnds, perm_vec, drive)

d      call dcxout(drive, '<CALCDRV> DRIVE',
d    1  max_bnds, num_drv_bnds, 1, out_un, out_len)

c    Save the drives
       call savedrv(j)

600  continue

     return

     end
```

LOADBNDS.FOR (Loads band drives from a file)

```
      subroutine loadbnds

c  This routine loads the active band numbers from the file specified
c  by bnd_file.

c  L. D. Luker, NRL/USRD, 09-JAN-1991.  Last modified on 10-APR-1991.

      implicit none

      include 'CWCMDL.INC/list'

      integer*4 i

d     type *, '<LOADBNDS> bnd_file =', bnd_file

      if ((bnd_file(1:8) .eq. 'allbands') . or.
     1   (bnd_file(1:8) .eq. 'ALLBANDS')) then

        do 100 i = 1, num_bnds
          drv_bnd(i) = i
d         type *, '    drv_bnd(', i, ') = ', drv_bnd(i)
100     continue

      else
        open(unit = bnd_un, file = bnd_file, status = 'OLD')
        do 200 i = 1, max_bnds
          read(bnd_un, *, end = 999) drv_bnd(i)
d         type *, '    drv_bnd(', i, ') = ', drv_bnd(i)
200     continue
      end if

999   num_drv_bnds = i - 1

d     type *, '<LOADBNDS> num_drv_bnds =', num_drv_bnds

      close (unit = bnd_un)

      return

      end
```

MAPFLDS.FOR (Computes predicted pressure fields)

```
      subroutine mapflds

c  This routine maps the pressure fields inside the CWC.

c  L. D. Luker, NRL/USRD, 27-SEP-1990.  Last modified on 29-MAY-1992.

      implicit none

      include 'CWCMDL.INC/list'

      character*20 filename
      integer*4 i, j
      real*4 angle, mag, phase, phas180, map_spd

c  Set up CHIEF if necessary
      if ((oper_mode .eq. 2) .and. (mod_type .eq. 2)) then
        call chzsub
      else if ((oper_mode .eq. 2) .or. (mod_type .eq. 2)) then
```

```
        call chfsub
      endif

c  Determine the number of points to map
      numfpn = nint(1 + (z_map_max - z_map_min) / z_map_delta)

c  Load the map coordinates
      do 100 i = 1, numfpn
        nfpxs(1, i) = x_map
        nfpxs(2, i) = y_map
        nfpxs(3, i) = z_map_min + (i - 1) * z_map_delta
100   continue

c  For each phase speed to map
      do 300 j = 1, num_map_spds

c     Load the drives
        call loaddrv(map_spd_num(j), map_spd)

c     Calculate the nearfield pressures with CHIEF
       if ((oper_mode .eq. 2) .and. (mod_type .eq. 2)) then
         call chznfp(drv_bnd(1))
       else
         call chfnfp(pmatx, vmatx, mdsize)
       endif

c     Write the map data
        filename = map_file(1:index(map_file,' ')-1) //
     1           '.MA' // char(j + 48) // char(0)

        open(unit = map_un, file = filename, status = 'NEW')

        write(map_un,'('' "Pressure-Field Map for'',
     1                 f7.2,'' m/s Phase Speed.  Run name: '',a,i,//,
     1                 '' " z (cm)       amp       pha (deg)'',
     1                 ''   amp err (dB)   pha err (deg)'')')
     1                 map_spd, run_name, j
        do 200 i = 1, numfpn
          angle = ((360. * freq) / map_spd) * nfpxs(3, i)
          write(map_un,'(f8.2,t13,1pg13.6,t27,0pf7.2,
     1          t39,0pf7.2,t54,0pf7.2)')
     1      nfpxs(3, i) * 100., mag(nfp(i)), phas180(phase(nfp(i))),
     1      20. * alog10(mag(nfp(i))), phas180(phase(nfp(i)) - angle)

200     continue

        close (unit = map_un)

300   continue

      return

      end
```

APPENDIX C

MODIFICATIONS TO CHIEF FOR THE CWC

Description of the Problem

The CHIEF program, as currently distributed, can give erroneous results when modeling thin radiating bodies. Although the problem with thin bodies is not mentioned in the CHIEF user's manual it has been observed previously where it was shown that the results do improve if a finer division of the surface is utilized [79]. Unfortunately, dividing the surface into very small subdivisions would increase the size of the CHIEF model of the CWC to the point that it could not be run on the available computational facilities. The problem with thin radiating bodies seems to arise from errors introduced when evaluating the surface integrals for points that are very near the integration surface. In particular, errors are introduced for thin bodies when evaluating the surface integral for a point that is on the "back" side of the integration surface. The limiting case of this integration problem (i.e., infinitely-thin body) is the same problem encountered, and solved, by CHIEF when integrating the Helmholtz self integrals.

Solution Implemented for the CWC

One solution to the problem of thin bodies is to evaluate the troublesome integrals using the same technique that CHIEF uses to evaluate the Helmholtz self integrals [80]. This consists of dividing the surface to be integrated into four triangular subregions (by cutting the original rectangular region with diagonals) and performing a change of variables. This allows integration of a function that grows rapidly as the center of the original region is approached (such as a singularity at the center). For this technique to work, the front and back of the thin body must both be divided into the same arrangement of subregions. To put it more precisely, the front and back surfaces must be divided in such a way that (in u,v coordinates) the center of the back subregions approach the center of the front subregions as the thickness of the thin body approaches zero. Fortunately, this condition is satisfied for the CWC models.

This technique has been implemented in CHIEF by modifying two subroutines. The subroutine SURMAT has been modified to call a new integration routine (CLSINT) for each surface area on the first symmetry block. The subroutine CLSINT is a combination of the original subroutines MATGEN and SLFINT. This routine performs all the surface integrals for the first symmetry block using the algorithm that was formerly only used for the self integrals.

The new technique was tested by using CHIEF's point-source check for a model of the CWC. The CWC was modeled as a cylindrical tube 25.2-cm long with an inner radius of 1.55 cm and a wall thickness of 0.75 mm. The tube was modelled using 18-fold rotational symmetry. The inner and outer surfaces of the tube were divided into bands that were 6.0-mm wide. A single point source was centered on the axis of the tube (i.e., at $z = 0$). The point-source check was run at 800 Hz using CHIEF with and without the modifications. Figure C1 shows the percent errors of the surface pressures computed by CHIEF relative to the pressures from the point-source model for the outer band surfaces. The results show that the errors are reduced dramatically by using the modified version of CHIEF.

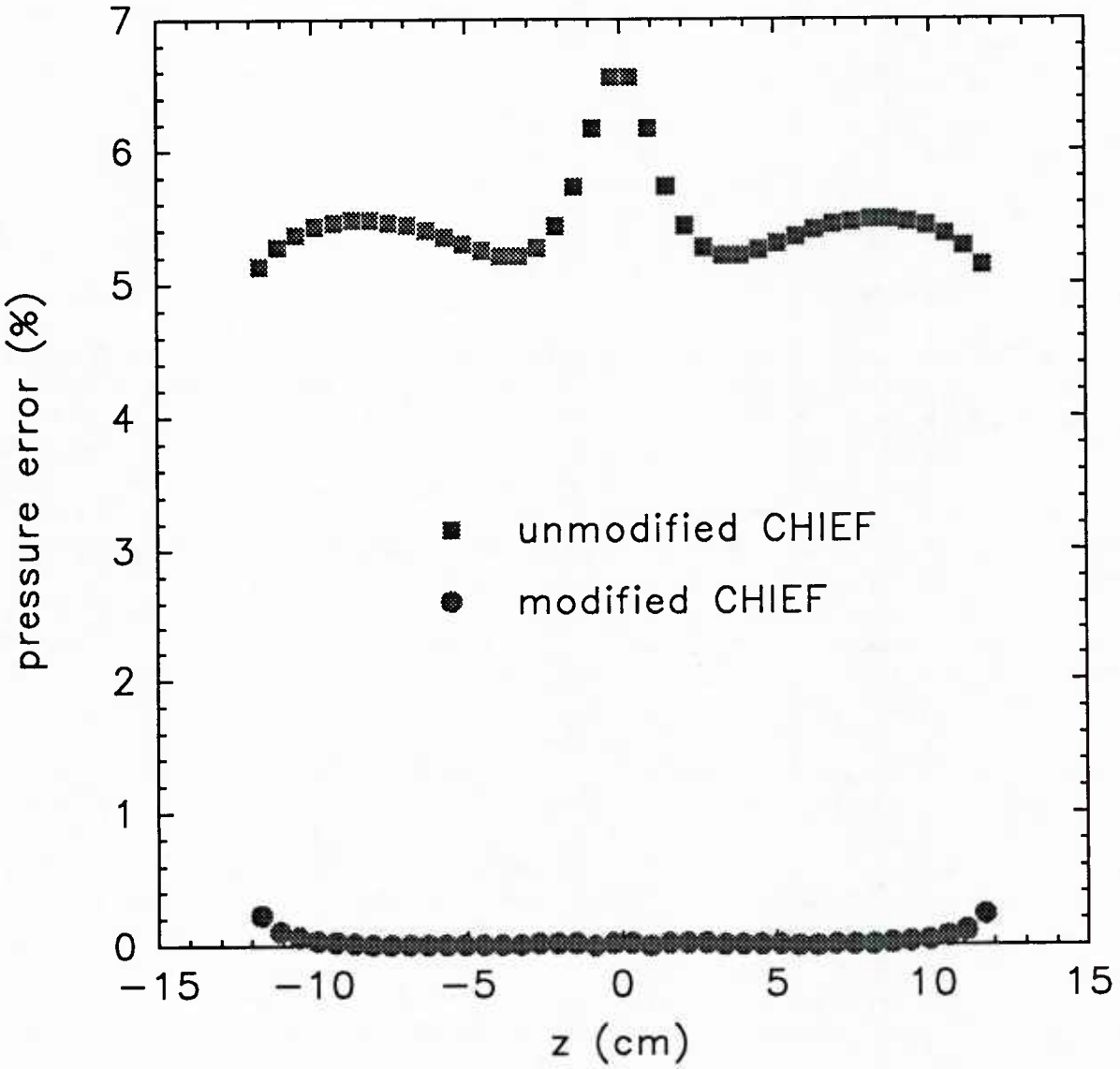

Fig. C1 — Pressure errors for the outer band surfaces using the point-source check from CHIEF with and without the modifications.

The disadvantages of this technique include the requirement placed on the layout of the surface subregions mentioned above and the fact that the more complex integration routine takes longer to run. The additional time required could be reduced by only using the more complex integration routine for the self integrals and the point that is opposite the area being integrated, but this would require considerable knowledge about how the user had subdivided and ordered the surface areas.

FORTRAN Code

SURMAT.FOR

```
      SUBROUTINE SURMAT(FREQ,SYMTYP,NBLKS,PMATX,VMATX,MTXDIM)

C     GENERATION OF P AND V SURFACE MATRICES

      PARAMETER (MXSREG=500)
      PARAMETER (MXIPS=20)
      PARAMETER (MXARS=500)
      PARAMETER (MXGAUS=64)
      PARAMETER (MXQPTS=512)
      PARAMETER (MXBLKS=100)
      PARAMETER (MXFFP=361)
      PARAMETER (MXNFP=361)

C     ****
      PARAMETER (MXFPS=520)
C     PARAMETER (MXFPS=MAX0(MXARS+MXIPS,MXFFP,MXNFP))
C     ***

      COMPLEX PMATX(MTXDIM), VMATX(MTXDIM)

      CHARACTER*3 SYMTYP

      COMMON/CONST/RHO,C
      COMMON/PRTCOM/NUNPRT,NUNERR
      COMMON/NDASG/NDQPTS,NDPMXS,NDVMXS,NDDECM,NDVELS,NDSPS,
     *             NDPMXF,NDVMXF,NDPMXN,NDVMXN,NDPSSP,NDEXPR,NDCOMV,
     *             NDTEMP,NDZRDB,NDPATB
      COMMON/SVALS/NSREG,NSEQNS(MXSREG),SUL(MXSREG),SUU(MXSREG),
     *             SVL(MXSREG),SVU(MXSREG),NSU(MXSREG),NSV(MXSREG),
     *             CCS(10,MXSREG),TRNSS(3,MXSREG),IZAX(MXSREG),
     *             IORDU(MXSREG),IORDV(MXSREG),NCCEQS
      COMMON/IPTS/NUMIPS,IPXS(3,MXIPS)
      REAL IPXS

      COMMON/QPTS/QPS(7,MXQPTS)
      COMMON/GAUSNS/WKGAUS(MXGAUS),ROOTU(MXGAUS),ROOTV(MXGAUS),
     *              WTUV(MXGAUS+1,2)
      COMMON/FLDPTS/FPBK1(4,MXFPS),FPC(4,MXFPS)

      COMMON/WORK/VEC1(MXARS),VEC2(MXBLKS),VEC3(MXBLKS),VEC4(MXBLKS),
     *            VEC5(MXFPS),VEC6(MXFPS)
      COMPLEX VEC2,VEC3,VEC4,VEC5,VEC6
      DIMENSION FACTRS(MXARS)
      EQUIVALENCE (FACTRS(1),VEC1(1))

      COMMON/PRGVLS/NDIMPV,NUMARS,NUMSFP,NUMFFP,NUMNFP,NWDVEC
      COMMON/SURARS/AREAS(MXARS)
      COMMON/TAPREC/RECRD(10),IRECRD(30)
      COMMON/TAPRC1/ARECRD(10)

C*************** impedance coating modification *************
      COMMON/COATING/ZCOAT,NUMZ
      COMPLEX ZCOAT(MXARS)
C***********************************************************

      CHARACTER*4 ARECRD

      COMPLEX JRHOWP
C
C     SURMAT ERROR CHECKS
C
```

```
      IERR=0

      IF (NSREG.GT.MXSREG.OR.NSREG.LE.0) THEN
        IERR=2
        WRITE(NUNERR,1001)NSREG
1001    FORMAT(/,' ERROR IN SURMAT - NSREG=',I6)
      END IF
      IF (NBLKS.GT.MXBLKS.OR.NBLKS.LE.0) THEN
        IERR=1
        WRITE(NUNERR,1002)NBLKS
1002    FORMAT(/,' ERROR IN SURMAT - NBLKS=',I6)
      END IF
      IF (SYMTYP.NE.'REF'.AND.SYMTYP.NE.'ROT') THEN
        IERR=1
        WRITE(NUNERR,1003)SYMTYP
1003    FORMAT(/,' ERROR IN SURMAT - SYMTYP= ',A3)
      END IF
      IF (NUMIPS.GT.MXIPS.OR.NUMIPS.LT.0) THEN
        IERR=1
        WRITE(NUNERR,1004)NUMIPS
1004    FORMAT(/,' ERROR IN SURMAT - NUMIPS=',I6)
      END IF

      IF (IERR.EQ.2) STOP

      NAR=0
      DO 1110 I=1,NSREG
      NAR=NAR+NSU(I)*NSV(I)
      IF (NSEQNS(I).GT.NCCEQS.OR.NSEQNS(I).LE.0) THEN
        IERR=1
        WRITE(NUNERR,1006)I,NSEQNS(I)
1006    FORMAT(/,' ERROR IN SURMAT - REG#,NSEQNS=',2I6)
      END IF
      IZABS=IABS(IZAX(I))
      IF (IZABS.GT.3.OR.IZABS.EQ.0) THEN
        IERR=1
        WRITE(NUNERR,1007)I,IZAX(I)
1007    FORMAT(/,' ERROR IN SURMAT - REG#,IZAX=',2I6)
      END IF
      IF (NSU(I)*NSV(I).LE.0) THEN
        IERR=1
        WRITE(NUNERR,1008)I,NSU(I),NSV(I)
1008    FORMAT(/,' ERROR IN SURMAT - REG#,NSU,NSV=',3I6)
      END IF
      IORDRU=IORDU(I)
      IORDRV=IORDV(I)
      IF (IORDRU.GT.MXGAUS.OR.IORDRV.GT.MXGAUS.OR.IORDRU*IORDRV
     *           .GT.MXQPTS.OR.IORDRU*IORDRV.LE.0) THEN
        IERR=1
        WRITE(NUNERR,1009)I,IORDRU,IORDRV
1009    FORMAT(/,' ERROR IN SURMAT - REG#,IORDRU,IORDRV=',3I6)
      END IF
1110  CONTINUE

      IF (NAR.GT.MXARS.OR.NAR.LE.0) THEN
        IERR=1
        WRITE(NUNERR,1111)NAR
1111    FORMAT(/,' ERROR IN SURMAT - #OF AREAS=',I10)
      END IF
      NFP=NAR+NUMIPS
      IF (NFP.GT.MXFPS.OR.NFP.LE.0) THEN
        IERR=1
        WRITE(NUNERR,1112)NFP
1112    FORMAT(/,' ERROR IN SURMAT - #OF FIELD POINTS=',I10)
      END IF
      MTXT=NAR*NFP
```

```
      IF (MTXT.GT.MTXDIM.OR.MTXT.LE.0) THEN
        IERR=1
        WRITE(NUNERR,1113)MTXT
1113    FORMAT(/,' ERROR IN SURMAT - ',I10,' WORDS NEEDED FOR P,V')
      END IF

      IF (IERR.NE.0) STOP

      PI=ACOS(-1.0)
      TWOPI=2.0*PI
      FOURPI=4.0*PI
      ROMEGA=TWOPI*FREQ
      JRHOWP=CMPLX(0.0,ROMEGA*RHO)/FOURPI
      SMALLK=ROMEGA/C
      NDIMPV=MTXDIM

C         COMPUTE QUADRATURE POINTS FOR EACH SURFACE SUBDIVISION(AREA)
C            STORE ON FILE/UNIT NDQPTS
C         COMPUTE FIELD POINT FOR EACH SURFACE AREA AND INTERIOR POINT
C            STORE IN ARRAY FPBK1


      CALL IOSUB(NDQPTS,10,QPS,0)
      ISUB=0

      DO 10 I=1,NSREG

      CALL GAUSS(IORDU(I),ROOTU,WTUV(1,1),WKGAUS)
      WTUV(MXGAUS+1,1)=IORDU(I)
      CALL GAUSS(IORDV(I),ROOTV,WTUV(1,2),WKGAUS)
      WTUV(MXGAUS+1,2)=IORDV(I)

      DELSU=(SUU(I)-SUL(I))/NSU(I)
      DELSV=(SVU(I)-SVL(I))/NSV(I)
      HDELSU=0.5*DELSU
      HDELSV=0.5*DELSV
      FACTI=HDELSU*HDELSV
      UAVE=HDELSU+SUL(I)
      DO 8 J=1,NSU(I)
      VAVE=HDELSV+SVL(I)
      DO 6 K=1,NSV(I)

      ISUB=ISUB+1
      FACTRS(ISUB)=FACTI

      CALL QPTGEN(UAVE,VAVE,HDELSU,HDELSV,NSEQNS(I),CCS(1,I),
     *            TRNSS(1,I),IZAX(I),IORDU(I),IORDV(I),ROOTU,ROOTV,QPS)

      CALL IOSUB(NDQPTS,1,WTUV,2*(MXGAUS+1))
      CALL IOSUB(NDQPTS,1,QPS,7*IORDU(I)*IORDV(I))

      CALL CCUNMD(UAVE,VAVE,NSEQNS(I),CCS(1,I),TRNSS(1,I),IZAX(I),
     *         FPBK1(1,ISUB),FPBK1(2,ISUB),FPBK1(3,ISUB),D1,D2,D3,DDJ,0)

6     VAVE=VAVE+DELSV
8     UAVE=UAVE+DELSU
10    CONTINUE

      NUMARS=ISUB
      NUMFPS=ISUB
      NWDVEC=2*NUMARS

      IF(NUMIPS.NE.0) THEN
        DO 20 J=1,NUMIPS
        ISUB=ISUB+1
        DO 15 I=1,3
```

```
15      FPBK1(I,ISUB)=IPXS(I,J)
20      CONTINUE
      END IF

      NUMFPS=NUMFPS+NUMIPS
      NUMSFP=NUMFPS
      MTXTOT=NUMARS*NUMFPS

C               GENERATION OF SURFACE MATRICES
C                  P MATRICES TO FILE/UNIT NDPMXS
C                  V MATRICES TO FILE/UNIT NDVMXS

      INTTYP=1

      CALL IOSUB(NDPMXS,10,PMATX,0)
      CALL IOSUB(NDVMXS,10,VMATX,0)

      DO 50 IBLK=1,NBLKS

C     ************** SYMMETRY CONSIDERATIONS ******************

      IF(SYMTYP.EQ.'REF') THEN
        CALL FPREFC(IBLK,NUMFPS,INTTYP,FPBK1,FPC)
      END IF

      IF (SYMTYP.EQ.'ROT') THEN
        GAMMA=TWOPI/NBLKS
        CALL FPROTC(IBLK,GAMMA,NUMFPS,INTTYP,FPBK1,FPC)
      END IF

C     ************************************************************

C==================  Modified for CWC (thin wall)  =============
      IF(IBLK.EQ.1) THEN
        CALL CLSINT(PMATX,VMATX,NUMARS,NUMFPS,SMALLK,INTTYP,
     *              ROOTU,ROOTV,WTUV,WKGAUS,MXGAUS,
     *              NSREG,NSEQNS,CCS,TRNSS,IZAX,SUL,SUU,SVL,SVU,
     *              NSU,NSV,NDQPTS,QPS,FPC,AREAS)
      ELSE
        CALL MATGEN(NUMARS,NUMFPS,FACTRS,INTTYP,WTUV,MXGAUS,
     *              NDQPTS,QPS,FPC,SMALLK,PMATX,VMATX)
      END IF
C=============================================================

      DO 30 I=1,MTXTOT
D     IF (IBLK.EQ.1) PRINT *, 'I,P,V', I, PMATX(I), VMATX(I)
      VMATX(I)=VMATX(I)*JRHOWP
30    PMATX(I)=-PMATX(I)/FOURPI

      IF(IBLK.EQ.1) THEN
        DO 40 I=1,NUMARS
        K=(I-1)*NUMFPS+I
40      PMATX(K)=PMATX(K)+0.5
      END IF

C*************** impedance coating modification *************
      CALL MTXSWZS(PMATX,VMATX,NUMARS,NUMZ,NUMIPS,ZCOAT)
C************************************************************

      CALL IOSUB(NDPMXS,1,PMATX,2*MTXTOT)
      CALL IOSUB(NDVMXS,1,VMATX,2*MTXTOT)

50    CONTINUE

      RECRD(1)=FREQ
      RECRD(2)=RHO
```

```
      RECRD(3)=C
      IRECRD(1)=NBLKS
      IRECRD(2)=MTXDIM
      IRECRD(3)=NUMARS
      IRECRD(4)=NUMSFP
      ARECRD(1)=SYMTYP

      RETURN
      END
```

CLSINT.FOR

```
      SUBROUTINE CLSINT(PMATX,VMATX,NUMARS,NUMFPS,SMALLK,INTTYP,
     *                  ROOTU,ROOTV,WTUV,WKGAUS,MXGAUS,
     *                  NSREG,NSEQNS,CCS,TRNSS,IZAX,SUL,SUU,SVL,SVU,
     *                  NSU,NSV,NDQPTS,QPS,FPC,AREAS)

C COMPUTES P AND V MATRIX ELEMENTS FOR CLOSE SURFACES AND SELF INTEGRALS

      COMPLEX PMATX(NUMFPS,NUMARS), VMATX(NUMFPS,NUMARS)

      DIMENSION ROOTU(MXGAUS),ROOTV(MXGAUS),WTUV(MXGAUS+1,2)
      DIMENSION WKGAUS(MXGAUS)
      DIMENSION AREAS(NUMARS),QPS(7,*),FPC(4,NUMFPS)

      DIMENSION NSEQNS(*),SUL(*),SUU(*),SVL(*),SVU(*),NSU(*),NSV(*),
     *          CCS(10,*),TRNSS(3,*),IZAX(*)

      COMPLEX PII, VII

      CALL IOSUB(NDQPTS,10,QPS,0)
      DO 100 N=1,NUMARS
        CALL IOSUB(NDQPTS,2,WTUV,2*(MXGAUS+1))
        IORDRU=WTUV(MXGAUS+1,1)
        IORDRV=WTUV(MXGAUS+1,2)
        CALL IOSUB(NDQPTS,2,QPS,7*IORDRU*IORDRV)
        II=0
        DO 100 I=1,NSREG
          CALL GAUSS(IORDRU,ROOTU,WTUV(1,1),WKGAUS)
          CALL GAUSS(IORDRV,ROOTV,WTUV(1,2),WKGAUS)
          DELSU=(SUU(I)-SUL(I))/NSU(I)
          DELSV=(SVU(I)-SVL(I))/NSV(I)
          HDELSU=0.5*DELSU
          HDELSV=0.5*DELSV
          FACTI=HDELSU*HDELSV
          UAVE=HDELSU+SUL(I)
          DO 80 J=1,NSU(I)
            VAVE=HDELSV+SVL(I)
            DO 60 K=1,NSV(I)
              II=II+1
              CALL HELMSI(UAVE,VAVE,HDELSU,HDELSV,NSEQNS(I),CCS(1,I),
     *                    TRNSS(1,I),IZAX(I),
     *                    INTTYP,SMALLK,FACTI,IORDRU,IORDRV,FPC(1,N),
     *                    ROOTU,ROOTV,WTUV(1,1),WTUV(1,2),PII,VII,AREAVL)
              PMATX(N,II)=PII
              VMATX(N,II)=VII
              AREAS(II)=AREAVL
60            VAVE=VAVE+DELSV
80          UAVE=UAVE+DELSU
100       CONTINUE
      RETURN
      END
```